

WL - TR - 97 -3046

**COMPUTATIONAL FLUID DYNAMIC
ANALYSIS OF A SINGLE-ENGINE
BUSINESS JET**



**Kenneth Wurtzler
Amid Ansari
Don Kinsey**

**December 1996
Final Report for Period Sep 95 - Nov 96**

Approved for public release; distribution unlimited

DTIC QUALITY INSPECTED 2

**Flight Dynamics Directorate
Wright Laboratory
Air Force Materiel Command
Wright-Patterson AFB OH 45433-7562**

19971223 148

NOTICE

USING GOVERNMENT DRAWINGS, SPECIFICATIONS, OR OTHER DATA INCLUDED IN THIS DOCUMENT FOR ANY PURPOSE OTHER THAN GOVERNMENT PROCUREMENT DOES NOT IN ANY WAY OBLIGATE THE US GOVERNMENT. THE FACT THAT THE GOVERNMENT FORMULATED OR SUPPLIED THE DRAWINGS, SPECIFICATIONS, OR OTHER DATA DOES NOT LICENSE THE HOLDER OR ANY OTHER PERSON OR CORPORATION; OR CONVEY ANY RIGHTS OR PERMISSION TO MANUFACTURE, USE, OR SELL ANY PATENTED INVENTION THAT MAY RELATE TO THEM.

THIS REPORT IS RELEASABLE TO THE NATIONAL TECHNICAL INFORMATION SERVICE (NTIS). AT NTIS, IT WILL BE AVAILABLE TO THE GENERAL PUBLIC, INCLUDING FOREIGN NATIONS.

THIS TECHNICAL REPORT HAS BEEN REVIEWED AND IS APPROVED FOR PUBLICATION.



DON W. KINSEY
Technical Area Leader
CFD Research Branch



GEORGE L. SEIBERT
Chief
CFD Research Branch



DENNIS SEDLOCK
Chief
Aeromechanics Division

IF YOUR ADDRESS HAS CHANGED, IF YOU WISH TO BE REMOVED FROM OUR MAILING LIST, OR IF THE ADDRESSEE IS NO LONGER EMPLOYED BY YOUR ORGANIZATION PLEASE NOTIFY WL/ FIMC WRIGHT-PATTERSON AFB OH 45433-7913 TO HELP MAINTAIN A CURRENT MAILING LIST.

Do not return copies of this report unless contractual obligations or notice on a specific document requires its return.

REPORT DOCUMENTATION PAGE			Form Approved OMB No. 0704-0188
<p>Public reporting burden for this collection of information is estimated to average 1 hour per response, including the time for reviewing instructions, searching existing data sources, gathering and maintaining the data needed, and completing and reviewing the collection of information. Send comments regarding this burden estimate or any other aspect of this collection of information, including suggestions for reducing this burden, to Washington Headquarters Services, Directorate for Information Operations and Reports, 1215 Jefferson Davis Highway, Suite 1204, Arlington, VA 22202-4302, and to the Office of Management and Budget, Paperwork Reduction Project (0704-0188), Washington, DC 20503.</p>			
1. AGENCY USE ONLY (Leave blank)	2. REPORT DATE	3. REPORT TYPE AND DATES COVERED	
	December 1996	FINAL REPORT, Sep 95 - Nov 96	
4. TITLE AND SUBTITLE		5. FUNDING NUMBERS	
Computational Fluid Dynamic Analysis of a Single-Engine Business Jet		PE 62201F PR 2404 TA LABR WBS CRD3	
6. AUTHOR(S)		8. PERFORMING ORGANIZATION REPORT NUMBER	
Kenneth Wurtzler, Amid Ansari, Don Kinsey			
7. PERFORMING ORGANIZATION NAME(S) AND ADDRESS(ES)		9. SPONSORING/MONITORING AGENCY NAME(S) AND ADDRESS(ES)	
Interdisciplinary & Appl CFD Section Flight Dynamics Directorate Wright Laboratory Air Force Materiel Command Wright-Patterson AFB OH 45433-7913		Flight Dynamics Directorate Wright Laboratory Air Force Materiel Command Wright-Patterson AFB OH 45433-7562 POC: D. KINSEY, WL/FIMC, 937-255-3876	
10. SPONSORING/MONITORING AGENCY REPORT NUMBER		WL-TR-97-3046	
11. SUPPLEMENTARY NOTES			
12a. DISTRIBUTION AVAILABILITY STATEMENT		12b. DISTRIBUTION CODE	
Approved for public release; distribution unlimited			
13. ABSTRACT (Maximum 200 words)			
<p>This report documents the longitudinal and lateral-directional aerodynamic analysis of a single-engine business jet aircraft. A Euler level analysis was chosen for the evaluation because of the size of the problem (complete aircraft with inlet and nozzle flow simulated) and the relatively large number of runs desired. While Euler analyses ignore viscous effects, it was determined that these effects would be small (except on drag estimates) for the cruise and low-speed flight conditions under consideration. Also, the primary emphasis was on providing incremental effects from a baseline condition, which is more accurate than absolute values.</p> <p>Variation of longitudinal and lateral-direction characteristics with Mach number, angle of attack and control deflections were determined. The maximum Mach number is up to the estimated wing drag divergence Mach number. Integrated force coefficient data and selected pressure coefficient data are presented. Comparisons with low-speed wind tunnel data are made where appropriate experimental data is available.</p>			
14. SUBJECT TERMS		15. NUMBER OF PAGES	
Computational Fluid Dynamics, Aerodynamics, Euler Analysis		90	
16. PRICE CODE			
17. SECURITY CLASSIFICATION OF REPORT	18. SECURITY CLASSIFICATION OF THIS PAGE	19. SECURITY CLASSIFICATION OF ABSTRACT	20. LIMITATION OF ABSTRACT
UNCLASSIFIED	UNCLASSIFIED	UNCLASSIFIED	UL

Table of Contents

	<u>Page</u>
1. Introduction	1
2. Total Aircraft Aerodynamic Analysis	4
2.1 Computational Method - Mercury	4
2.2 Computational Grid	4
2.3 Boundary Conditions	5
2.4 Computational Approach	5
2.5 Results and Discussion	5
2.5.1 Longitudinal Aerodynamics	6
2.5.2 Lateral Aerodynamics	8
3. Aileron Effectiveness	47
3.1 Computational Method - Team	47
3.2 Computational Grid	47
3.3 Boundary Conditions	47
3.4 Computational Approach	48
3.5 Results and Discussion	48
4. Drag Divergence Analysis	58
5. Elevator Effectiveness	60
6. Horizontal Tail Fairing	71
7. Comparison of CFD Data with 2-D Airfoil Data	85
8. Summary	87
9. References	89
List of Symbols	90

Preceding Page Blank

List of Figures

	<u>Page</u>
Figure 1 Century Jet 3-View	2
Figure 2 View of Grid Topology around Century Aircraft	10
Figure 3 Grid on Top Midsection. Main Engine Inlet and Auxiliary Inlet Shown in Red. (Right Half of Aircraft Shown.)	10
Figure 4 Aft End of Half of Aircraft. Engine Exhaust Face Shown in Red	11
Figure 5 Top View of Right Half, Ailerons and Elevator Shown in Red	11
Figure 6 Convergence History for Mach = 0.7, Angle of Attack =0.0	12
Figure 7 Convergence History for Mach = 0.7, Angle of Attack = 4.0	12
Figure 8 Lift Coefficient versus Angle of Attack	13
Figure 9 Pitch Coefficient versus Angle of Attack	13
Figure 10 Side View, Mach = 0.2, Angle of Attack = 0.0	14
Figure 11 Front View, Mach = 0.2, Angle of Attack = 0.0	14
Figure 12 Top View, Mach = 0.2, Angle of Attack = 0.0	15
Figure 13 Bottom View, Mach = 0.2, Angle of Attack = 0.0	15
Figure 14 Side View, Mach = 0.2, Angle of Attack = 4.0	16
Figure 15 Front View, Mach = 0.2, Angle of Attack = 4.0	16
Figure 16 Top View, Mach = 0.2, Angle of Attack = 4.0	17
Figure 17 Bottom View, Mach = 0.2, Angle of Attack = 4.0	17
Figure 18 Side View, Mach = 0.7, Angle of Attack = 0.0	18
Figure 19 Front View, Mach = 0.7, Angle of Attack = 0.0	18
Figure 20 Top View, Mach = 0.7, Angle of Attack = 0.0	19
Figure 21 Bottom View, Mach = 0.7, Angle of Attack = 0.0	19
Figure 22 Side View, Mach = 0.7, Angle of Attack = 4.0	20
Figure 23 Front View, Mach = 0.7, Angle of Attack = 4.0	20
Figure 24 Top View, Mach = 0.7, Angle of Attack = 4.0	21
Figure 25 Bottom View, Mach = 0.7, Angle of Attack = 4.0	21
Figure 26 Underside View of Aircraft with Mach Contours. Mach = 0.2, Angle of Attack = 0.0	22
Figure 27 Underside View of Aircraft with Mach Contours. Mach = 0.2, Angle of Attack = 4.0	22
Figure 28 Underside View of Aircraft with Mach Contours. Mach = 0.7, Angle of Attack = 4.0	23
Figure 29 Underside View of Aircraft with Mach Contours. Mach = 0.7, Angle of Attack = 4.0	23
Figure 30 Plot of Incoming Flow Angle versus Span Location on Horizontal Tail. Mach = 0.7, Angle of Attack = 0.0	24
Figure 31 Plot of Incoming Flow Angle versus Span Location on Horizontal Tail. Mach = 0.7, Angle of Attack = 2.0	24
Figure 32 Plot of Incoming Flow Angle versus Span Location on Horizontal Tail. Mach = 0.7, Angle of Attack = 4.0	25
Figure 33 Wing Span Location of Cp Plots	25

List of Figures (Continued)

	<u>Page</u>
Figure 34 Wing Cp. Mach = 0.2, Angle of Attack = 0.0	26
Figure 35 Wing Cp. Mach = 0.2, Angle of Attack = 1.0	26
Figure 36 Wing Cp. Mach = 0.2, Angle of Attack = 4.0	27
Figure 37 Wing Cp. Mach = 0.7, Angle of Attack = 0.0	27
Figure 38 Wing Cp. Mach = 0.7, Angle of Attack = 1.0	28
Figure 39 Wing Cp. Mach = 0.7, Angle of Attack = 2.0	28
Figure 40 Wing Cp. Mach = 0.7, Angle of Attack = 4.0	29
Figure 41 Wing Cp. Mach = 0.75, Angle of Attack = 1.0	29
Figure 42 Wing Cp. Mach = 0.75, Angle of Attack = 2.0	30
Figure 43 Lift Coefficient versus Beta Angle	30
Figure 44 Pitch Coefficient versus Beta Angle	31
Figure 45 Roll Coefficient versus Beta Angle	31
Figure 46 Yaw Coefficient versus Beta Angle	32
Figure 47 Windward Side, Mach = 0.20, Angle of Attack = 0.0, Beta = 5.0	32
Figure 48 Leeward Side, Mach = 0.20, Angle of Attack = 0.0, Beta = 5.0	33
Figure 49 Front View, Mach = 0.20, Angle of Attack = 0.0, Beta = 5.0	33
Figure 50 Top View, Mach = 0.20, Angle of Attack = 0.0, Beta = 5.0	34
Figure 51 Bottom View, Mach = 0.20, Angle of Attack = 0.0, Beta = 5.0	34
Figure 52 Windward Side, Mach = 0.20, Angle of Attack = 0.0, Beta = 10.0	35
Figure 53 Leeward Side, Mach = 0.20, Angle of Attack = 0.0, Beta = 10.0	35
Figure 54 Front View, Mach = 0.20, Angle of Attack = 0.0, Beta = 10.0	36
Figure 55 Top View, Mach = 0.20, Angle of Attack = 0.0, Beta = 10.0	36
Figure 56 Bottom View, Mach = 0.20, Angle of Attack = 0.0, Beta = 10.0	37
Figure 57 Windward Side, Mach = 0.70, Angle of Attack = 0.0, Beta = 5.0	37
Figure 58 Leeward Side, Mach = 0.70, Angle of Attack = 0.0, Beta = 5.0	38
Figure 59 Front View, Mach = 0.70, Angle of Attack = 0.0, Beta = 5.0	38
Figure 60 Top View, Mach = 0.70, Angle of Attack = 0.0, Beta = 5.0	39
Figure 61 Bottom View, Mach = 0.70, Angle of Attack = 0.0, Beta = 5.0	39
Figure 62 Windward Side, Mach = 0.70, Angle of Attack = 0.0, Beta = 10.0	40
Figure 63 Leeward Side, Mach = 0.70, Angle of Attack = 0.0, Beta = 10.0	40
Figure 64 Front View, Mach = 0.70, Angle of Attack = 0.0, Beta = 10.0	41
Figure 65 Top View, Mach = 0.70, Angle of Attack = 0.0, Beta = 10.0	41
Figure 66 Bottom View, Mach = 0.70, Angle of Attack = 0.0, Beta = 10.0	42
Figure 67 Windward Wing Cp. Mach = 0.20, Angle of Attack = 0.0, Beta = 5.0	43
Figure 68 Leeward Wing Cp. Mach = 0.20, Angle of Attack = 0.0, Beta = 5.0	43
Figure 69 Windward Wing Cp. Mach = 0.20, Angle of Attack = 0.0, Beta = 10.0	44
Figure 70 Leeward Wing Cp. Mach = 0.20, Angle of Attack = 0.0, Beta = 10.0	44

List of Figures (Continued)

	Page
Figure 71 Windward Wing Cp. Mach = 0.70, Angle of Attack = 0.0, Beta = 5.0	45
Figure 72 Leeward Wing Cp. Mach = 0.70, Angle of Attack = 0.0, Beta = 5.0	45
Figure 73 Windward Wing Cp. Mach = 0.70, Angle of Attack = 0.0, Beta = 10.0	46
Figure 74 Leeward Wing Cp. Mach = 0.70, Angle of Attack = 0.0, Beta = 10.0	46.
Figure 75 Surface Mach Number Contours, Mach = 0.70, Angle of Attack = 0.0	50
Figure 76 Lift Coefficient Variation with Aileron Deflections, Mach = 0.70, Angle of Attack = 0.0	51
Figure 77 Drag Coefficient Variation with Aileron Deflections, Mach = 0.70, Angle of Attack = 0.0	52
Figure 78 Pitching Moment Coefficient Variation with Aileron Deflections, Mach = 0.70, Angle of Attack = 0.0	53
Figure 79 Change in Force Coefficients with Aileron Deflection, Experimental Mach = 0.2, Numerical Mach = 0.70	54
Figure 80 Pressure Coefficients with Aileron Deflections at Given Span Station, Mach = 0.70	55
Figure 81 Pressure Coefficients at Different Span Stations for Given Aileron Deflections, Mach = 0.70	56
Figure 82 Pressure Coefficients on Tail due to Wing Aileron Deflections	57
Figure 83 Drag Divergence	59
Figure 84 Effect of Elevator Deflection on Lift Coefficient	62
Figure 85 Effect of Elevator Deflection on Drag Coefficient	63
Figure 86 Effect of Elevator Deflection on Pitching Moment Coefficient	64
Figure 87 Variation of Lift Coefficient with Iterations	65
Figure 88 Variation of Drag Coefficient with Iterations	66
Figure 89 Variation of Pitching Moment Coefficient with Iterations	67
Figure 90 Tail Pressure Coefficients with Elevator Deflections - B.L. 1.6	68
Figure 91 Tail Pressure Coefficients with Elevator Deflections - B.L. 4.1	69
Figure 92 Tail Pressure Coefficients with Elevator Deflections - B.L. 6.9	70
Figure 93 Horizontal Tail with KEW Fairing	73
Figure 94 Horizontal Tail Geometry Normalized to Unit Length	74
Figure 95 Pressure Coefficient on Tail with/without Tail Fairing - B.L. 0.56	75
Figure 96 Pressure Coefficient on Tail with/without Tail Fairing - B.L. 1.42	76
Figure 97 Pressure Coefficient on Tail with/without Tail Fairing - B.L. 3.34	77
Figure 98 Pressure Coefficient on Tail with/without Tail Fairing - B.L. 6.85	78
Figure 99 Pressure Coefficient on Tail with/without Tail Fairing - B.L. 7.75	78
Figure 100 Velocity Vectors below Tail Fairing	79

List of Figures (Concluded)

	<u>Page</u>
Figure 101 Velocity Vectors below Tail without Fairing	80
Figure 102 Mach Number Contours on Top of Tail with Fairing	81
Figure 103 Mach Number Contours on Top of Tail without Fairing	82
Figure 104 Mach Number Contours below Tail with Fairing	83
Figure 105 Mach Number Contours below Tail without Fairing	84
Figure 106 Pressure Coefficient Comparison of 2-D Airfoil with 3-D Wing	86

List of Tables

	<u>Page</u>
Table 1 Matrix of Solutions	2
Table 2 Century Jet Wave Drag Estimates	58
Table 3 Elevator Effectiveness	60
Table 4 Tail Fairing Effectiveness	72

Foreword

This report was prepared by the Applied Computational Fluid Dynamics Section, CFD Research Branch, Aeromechanics Division, Flight Dynamics Directorate of the Wright Laboratory. The work was accomplished under Cooperative Research and Development Agreement (CRDA) number 95-201-WL-01, signed by Wright Laboratory on 28 Sep 95. While the CRDA covers a wide range of technologies available in Wright Laboratory, this effort concentrates on computational fluid dynamic analysis of the longitudinal and lateral directional aerodynamic characteristics of the Century Jet configuration.

The technical effort was completed by a team of engineers which includes the three authors of this report plus Captain Matt Grismer and Mr. Howard Emsley. Century Aerospace Corporation engineers and consultants providing direction and guidance included Mr. Leon Mark, Mr. Dan Cichy, Mr. Dan Apel and Mr. Don Coburn.

Computational Fluid Dynamic Analysis of a Single-Engine Business Jet

1. Introduction

This Computational Fluid Dynamic (CFD) analysis was conducted by the Applied Computational Fluid Dynamics Section of the CFD Research Branch, Aeromechanics Division, Flight Dynamics Directorate, Wright Laboratory. The work was conducted under a Cooperative Research and Development Agreement (CRDA) between Wright Laboratory and the Century Aerospace Corporation. Under this agreement the Air Force was to provide CFD analysis of the Century Jet single-engine business jet aircraft. Specifically, the analyses were to predict the longitudinal and lateral-directional aerodynamic characteristics with Mach number, angle of attack, and control surface deflections for the modeled aircraft. The maximum Mach number was to be at least up to the estimated wing drag divergence Mach number. A qualitative evaluation of the airflow conditions at the inlet face and the interaction of the inlet nacelle airflow on the vertical tail was conducted by reviewing the flow solutions on workstations. Wing airfoil and chordwise and spanwise pressures were compared to analytical predictions computed by OSU with their airfoil computer codes. After consultation with Century engineers, the conditions listed in Table 1 were determined to be the desired analyses in order to meet the above objectives.

The Century Jet is a single-engine, six-place business jet of approximately 5000 pounds gross take-off weight. The aircraft was designed by North American Aeronautical Consultants of Columbus, Ohio and is of conventional design with a high-aspect ratio wing and a conventional horizontal-vertical tail arrangement (See Figure 1). The inlet for the Williams/Rolls FJ44 turbofan engine is top mounted, much like the centerline engine on Boeing's 727 jet airliner. Preliminary performance figures include a maximum speed of Mach 0.75 and a 1,331 nautical mile range at 288 knots cruise speed at 40,000 feet altitude. It is at these higher subsonic Mach numbers that CFD analysis is needed to supplement the Ohio State University low-speed (Mach = 0.20) wind tunnel test data¹.

A Euler level analysis was chosen for the aerodynamic evaluation over the more exact Navier-Stokes methods because of the size of the problem (a complete aircraft, with inlet and nozzle), and the relatively large number of runs desired. While Euler analyses ignore viscous effects (e.g., boundary layers) it was determined that these effects would be small (except for drag) for the cruise and low-speed flight conditions under consideration. Also, the primary emphasis was on providing incremental effects from a low speed baseline condition for design and performance analyses.

The geometry information for the Century Jet was provided by Century in the form of Computer Aided Design (CAD) files. These files were read into an Intergraph CAD program where the geometry was checked and prepared for the next step--grid generation. Grid generation was accomplished using the Gridgen structured grid generation program on a

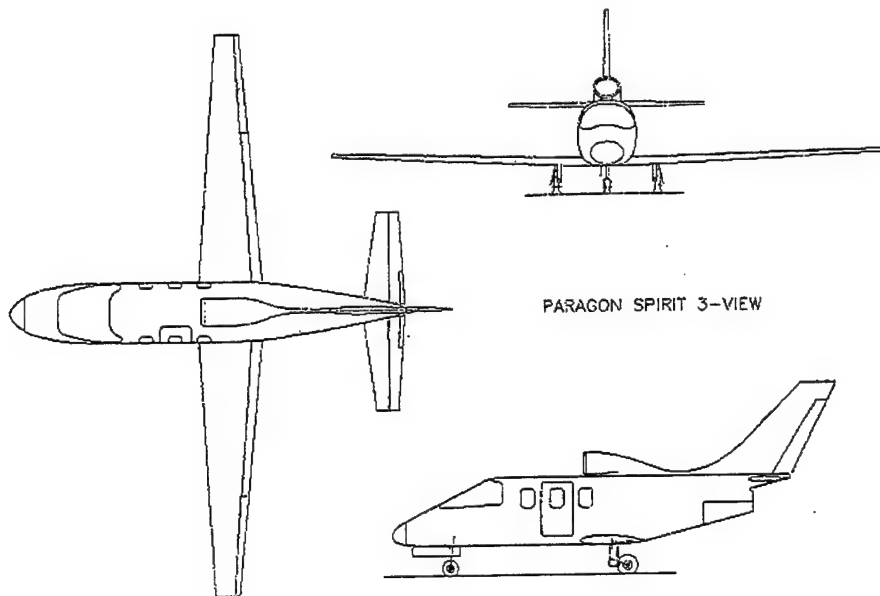


Figure 1 Century Jet 3-View

Table 1
Matrix of Solutions

<u>Purpose</u>	<u>Mach No.</u>	<u>AOA</u>	<u>Beta</u>	<u>Aileron</u>	<u>Elevator</u>
Longitudinal Aero	0.70	0, 2, 4	0	0	0
	0.20	0, 4	0	0	0
Drag Rise	0.20, 0.70, 0.75, 0.80	1	0	0	0
	0.75	2	0	0	0
	0.70	0	5, 10	0	0
Lateral-Directional	0.20	0	5, 10	0	0
	0.70	0	0	10, 5, 0, -5, -10	0
Control Effectiveness	0.70	0	0	0	10, 5, 0, -5, -10
	0.70	0	0	10, 5, 0, -5, -10	0

Silicon Graphics work station. The computations were run on a variety of computers, including IBM workstations, an IBM SP2 parallel computer and Cray C-90s. Two separate codes were used. A strictly Euler code, Mercury, was used for most of the longitudinal and lateral-directional analyses, and an Euler/Navier-Stokes code, TEAM, for the aileron and elevator effectiveness studies. Additional information on the grid generation and flow solvers is provided in Sections 2 and 3. The Sections are essentially independent analyses of particular aspects of the aerodynamics and contain a discussion of the results followed by figures as appropriate.

2 Total Aircraft Aerodynamic Analysis

2.1 Computational Method - Mercury

The numerical analysis of the Century aircraft that deals with longitudinal aerodynamic characteristics, drag rise, and lateral directional stability was accomplished using the Mercury code. The Mercury code is a derivative of Jameson's finite volume, cell-centered, Runge-Kutta method that was developed in-house. The code incorporates implicit residual smoothing and enthalpy damping and is strictly an Euler code. Local time-stepping is used to accelerate convergence. Inputs to the code include a body-conforming, structured grid, a flow condition file, and a grid connectivity file. Various boundary conditions, such as solid, far-field, sink, source, and symmetry can be applied only at block faces, but block faces can have multiple boundary conditions. Previous cases on which this code has been applied span a range of conditions and flows including escape capsule geometries, generic forebodies at high angles of attack, fighter configurations, and large transports.

2.2 Computational Grid

The grid constructed for the CFD analysis of the Century aircraft is a multi-block grid with point-to-point match-up at block interfaces. The complete grid generation process was accomplished with the Gridgen code on a Silicon Graphics workstation. Due to the complexity of the geometry, the grid consisted of 21 blocks in a C-C topology. Block outlines of these blocks and the surface grid of the right-half of the aircraft are shown in Figure 2. Since the aircraft was symmetric about the yaw plane, one half of the aircraft was used for non-yawed runs. A total of 1,348,777 points were used to build the computational domain around half of the aircraft.

The geometry used for the aircraft surface was brought into Gridgen as a collection of IGES entities. The aircraft has several features that had to be distinctly modeled in the grid generation process. The grid stops just beyond the edge of the engine inlet lip inside the duct and that face serves as the boundary face for the inlet airflow. The external shape of the auxiliary inlet serves as the computational face for that inlet. These two faces are prominently displayed in Figure 3. The engine exhaust face is defined in the grid as the external definition of the nozzle as seen in Figure 4. The wing has a flat trailing edge that was defined with three points. The horizontal tail had a flat trailing edge but due to the scale of the thickness and the fact that this is an Euler analysis, the edge was sharpened to the top edge line. The tips of the wing, horizontal tail, and rudder were kept flat and have the shape of the airfoil at the tip. The outlines for the ailerons and elevators on the wing and horizontal tail were kept in the surface grid so as to account for them in the control surface deflection cases. In Figure 5, a top view of the surface grid is shown with these features marked.

Grid spacing was kept as even and smooth as possible throughout the surface and domain. The auxiliary inlet, located underneath the main engine inlet, dictated the minimum grid spacing in the domain. The far field boundaries were 7 fuselage lengths away to accommodate the $Mach = 0.2$ flow cases.

2.3 Boundary Conditions

The main engine inlet and the auxiliary inlet both were assigned sink boundary conditions. The main inlet was specified with a mass flow rate and the auxiliary inlet was specified with a pressure. At Mach = 0.2, the auxiliary inlet was specified with a no-flow condition (essentially a solid surface) and the main inlet was assigned a mass flow rate of 55.8 lbs/sec. (take-off conditions). At cruise conditions of Mach = 0.7 and an altitude of 36,000 ft., the auxiliary inlet was specified with a pressure value of $P = 4.1954$ psia and the main inlet was assigned a mass flow rate of 24 lbs/sec. All of the cases run with Mercury were with engine thrust simulated. This was specified at the exhaust face with Mach number (M), pressure (P), and temperature (T). For Mach = 0.2, the exhaust face had values of $T = 712.48$ °R, $P = 12.304$ psia, and $M = 0.82$. For the higher Mach = 0.7 case, the values were $T = 624$ °R, $P = 3.99$, and $M = 1.01$. The solid surface was specified with a flow tangency boundary condition for all cases.

2.4 Computational Approach

A total of 14 runs were accomplished with the Mercury code. These runs were performed on an IBM RS6000 workstation. Convergence was determined by a leveling off of the body forces and a drop of at least 4 orders of magnitude in the residuals. The two plots in Figures 6 and 7 show variance in the body forces versus the number of iterations for two Mach = 0.7 cases. For the angle-of-attack case equal to 4.0, the oscillating behavior in the side force indicates areas of unsteadiness in the flow. This exhibits itself most in the pitching moment. The angle-of-attack case equal to 0.0 reveals no noticeable oscillations in the body forces. For this case, the flow is more steady and the aerodynamic coefficients converged to a definite number. Convergence occurred at approximately 3000 iterations for this case with a CFL of 5. For the higher angles of attack, runs were taken to 5000 iterations with no settling of the body forces or coefficients.

2.5 Results and Discussion

Aerodynamic coefficients such as pitch, roll, and yaw are all taken with reference to the wind-axis system for the aircraft. The x,y,z coordinates for the moment reference point are $x = 180.352$, $y = 0.0$, and $z = 14.1$ inches. The reference lengths for moments about the axis system are 426 (x), 50.985 (y), and 426 (z) inches. The reference area used in calculating the aerodynamic coefficients is the wing surface area, $20,160$ in². A positive pitching moment is nose-up, a positive yawing moment is nose to the left, and a positive rolling moment is left wing down. A positive angle of attack is with a nose-up attitude and a positive beta angle is with nose left (wind coming from right side).

2.5.1 Longitudinal Aerodynamics

Longitudinal aerodynamic characteristics of the Century aircraft were determined by varying angle of attack at two Mach numbers, 0.2 and 0.7. The angles of attack investigated were 0, 2, 4 degrees for Mach = 0.2 and 0 and 4 degrees for Mach = 0.7. A Mach = 0.75 case with angles of attack of 1 and 2 is also included in this portion of the analysis. This case was initially calculated to determine drag rise. Comparison of the lift coefficient versus angle of attack gives a good indication that the CFD code is performing correctly. As seen in Figure 8, the lift curves for the four cases all give positive, linear slopes. The Mach = 0.75 curve almost lies directly on the Mach = 0.7 curve for angles of attack 1 and 2. The lift calculated by the CFD code does not include viscous effects. Since the wing on the aircraft is straight and no vortex lift is expected, the lift should be linear with angle of attack up to drag divergence. (See Section 4 for drag rise information). Figure 9 contains a plot of pitch coefficient versus angle of attack. The pitching moment is non-linear with angle of attack. The aircraft responds with less positive nose-up force in all of the cases and obtains a negative pitching moment for the Mach = 0.7 case at angle of attack equal to 4.0. (The data referring to 'New Fairing' in both of these plots is discussed in Section 6.)

A qualitative view of the results is presented in the form of the surface colored by local Mach number. This provides a view of the physical flow features of each case. For each case analyzed, four views will be presented - side, front, top, and bottom. Together with the quantitative data from above, a complete picture of the aerodynamic attributes of the aircraft are revealed.

At Mach = 0.2 and AOA = 0.0, the flow is quite benign over the complete aircraft (Figures 10-13). From the side view, areas of higher speed flow are displayed over the cockpit, at the wing-fuselage juncture, and below the horizontal tail root. The flow appears to be well behaved on the side of and behind the main engine inlet fairing. From the front, the flow into the main engine inlet is undisturbed. The top view clearly shows the area of lift on the upper wing as well as the flow expansion over the front of the fuselage area. The bottom view shows clean flow on the underside with a small area of low-speed flow at the rear of the horizontal tail-fuselage juncture.

At Mach = 0.2, AOA = 4.0, the same four views (Figures 14-17) show changes due to an increase in angle of attack. The flow expansion over the cockpit is greater, as is the expansion at the wing-fuselage juncture. Compared to the previous case, the flow does not accelerate around the horizontal tail root as much. The flow over the wing indicates high velocity flow much closer to the leading edge, as seen in the top view. The bottom view shows that the region of low-speed flow is reduced at this higher angle of attack.

At the higher speed case of Mach = 0.7, AOA = 0.0 (Figures 18-21), the flow exhibits transonic characteristics over the wing and around the main engine inlet fairing. From the front view, it is apparent that the flow into the main engine inlet is undisturbed. The distinct high speed region on top of the wing terminates with a rapid compression or possibly a weak

shock wave. On top of the horizontal tail, the high speed region remains near mid-chord. The region underneath the horizontal tail becomes much more unsteady and larger. The low speed region seems to encompass a smaller region of high speed flow. This type of flow irregularity implies flow separation with a region of random and reversed flow. The origin and extent of such a separation should be considered only qualitative, since the Euler equations do not model viscous effects. From the side, this separation bubble seems to stem from the flow not being able to turn under the horizontal tail.

At the higher angle of attack of 4.0, $\text{Mach} = 0.7$ (Figures 22-25), as seen from the side, the airflow along the fuselage seems to be able to turn around the horizontal tail better compared to the previous flow case. The flow into the main engine inlet remains constant at about a Mach number of 0.5. The high speed region on top of the wing and the front fuselage become greater and more distinct. The low pressure region on the wing moves closer to the leading edge. The flow underneath the aircraft lowers in speed. This causes the low speed/separation region at the horizontal tail root to become smaller.

A more detailed look at the underside region at the horizontal tail/fuselage juncture is provided in Figures 26-29. The low speed region first appears at $\text{Mach} = 0.2$, $\text{AOA} = 0.0$. The region remains near the fuselage and does not extend down the rear of the fuselage. At the leading edge of the horizontal tail, the flow accelerates downward. At an angle of attack of 4.0, the region disappears. The high acceleration region is lessened and does not reach as far down. At $\text{Mach} = 0.7$, $\text{AOA} = 0.0$, the region spreads out on the underside of the horizontal tail and forward and down on the fuselage. At an angle of attack of 4.0, the horizontal extent of the region is lowered but the vertical extent remains about the same. The initial cause of this region appears to be the inability of the flow to turn around the leading edge of the horizontal tail. Figures 30-32 contain plots of incoming flow angle versus span location on the horizontal tail for $\text{Mach} = 0.70$, $\text{AOA} = 0, 2$ and 4. The six different locations refer to how far in front of the leading edge the data is collected. In each plot, the flow has a high negative angle at the root. In general the flow angle is large, but is especially large right at the leading edge. It is the lowest at $\text{AOA} = 2.0$ and approximately equal at the other angles of attack.

Pressure distributions on both the upper and lower surfaces of the wing are presented in Figures 33-42. In Figure 33, the span locations at which the data is collected are shown on the aircraft planform. These locations are actual grid lines on the wing and were chosen so as to give complete coverage of the wing. The three cases with $\text{Mach} = 0.2$ are presented in Figures 34-36. Several trends are evident. First, as the angle of attack increases, the maximum negative pressure coefficient increases and moves forward on the wing. Second, the flow on the underside of the wing remains fairly stable through the increase in angle of attack. The oscillations in the data found in the first quarter chord are a result of a wide surface grid spacing at the leading edge of the wing. The curvature of the wing leading edge is not adequately defined for this low speed case.

For the $\text{Mach} = 0.7$ cases, the low pressure on the upper wing reaches a greater value and the peak is more centered than in the low speed case. The peak remains in the same chord

location as the angle of attack increases while the pressure on the first quarter of the chord becomes more negative. The Mach = 0.75 cases in Figures II.23 and 24 show the peak pressure point moving aft on the wing.

2.5.2 Lateral Aerodynamics

The lateral stability characteristics of the aircraft were obtained by running a high and low speed case at two beta angles, 5 and 10 degrees. The complete aircraft configuration was run due to the asymmetry of the flow. A positive beta angle involves a nose left flight attitude. These two cases were run at an angle of attack of 0.0. A plot of lift versus beta angle is shown in Figure 42. At beta = 5.0, the lift coefficient decreases slightly but returns to the C_l value at beta = 10.0 for both Mach cases. The pitch coefficient behaves in a reverse manner, as shown in Figure 44. It increases at beta = 5.0 and then decreases at beta = 10.0. Figure 45 contains a plot of rolling coefficient versus beta angle. The high speed case exhibits a very small negative rolling moment (right wing down). The low speed case responds linearly with a much greater negative rolling moment (right wing down). Finally, in Figure 46, the yawing coefficient in both cases responds linearly with a negative yawing moment (nose right).

The qualitative results, consisting of color contours of local Mach number on the surface, reveal areas where the flow accelerates due to the beta angles and where the flow speed decreases. Each case contains five views - windward, leeward, front, top, and bottom. The Mach = 0.2, beta = 5.0 case is shown in Figures 47-51 and the Mach = 0.2, beta = 10.0 case is shown in Figures 52-56. The higher Mach case of 0.7 is shown in Figures 57-61 for beta = 0.5 and Figures 62-66 for beta = 10.0.

The two top views for the lower Mach case (Figure 50 and 55) show that the leeward wing experiences higher speed flow over the top surface. The top surface of the windward wing experiences more stagnating flow at the leading edge root. As beta increases from 5.0 to 10.0, these differences become greater. The flow under the wing on the windward side accelerates as beta increases as seen in Figures 51 and 56. The combination of these two events produces the comparatively large negative rolling moment (right wing down) for the Mach = 0.2 case (Figure 45).

For the higher Mach case, there is not a large negative rolling moment. The qualitative analysis reveals that the differences seen in the Mach = 0.2 case do not exist in the same magnitude for the Mach = 0.7 case. The windward leading edge root does experience reduced velocity flow and the leeward wing does experience accelerated flow at the root. However, the magnitude of these differences does not cause a large negative rolling moment. Figures 67-74 contain plots of pressure coefficients for the windward and leeward wings for all four beta cases. The lower pressure values under the leading edge root on the windward side are shown in Figures 67, 69, 71 and 73. The corresponding plots for the leeward side are shown in Figures 68, 70, 72 and 74. The Mach = 0.2 case has a region of lower pressure at the root on the windward side when compared to the leeward side wing. The corresponding

plots for the Mach = 0.7 case do not show as great a discrepancy. This could account for the difference in rolling moments.

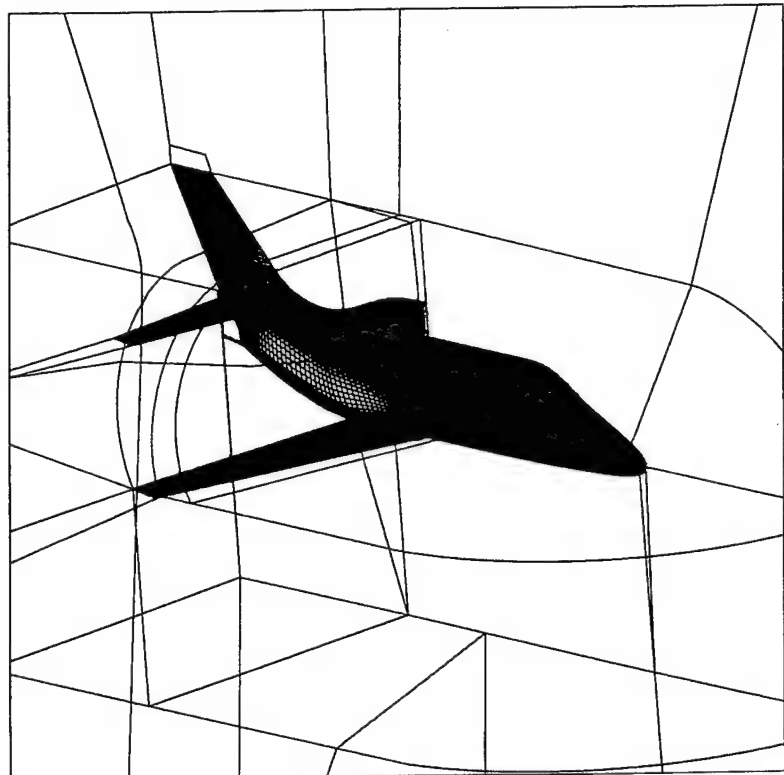


Figure 2 View of Grid Topology around Century Aircraft

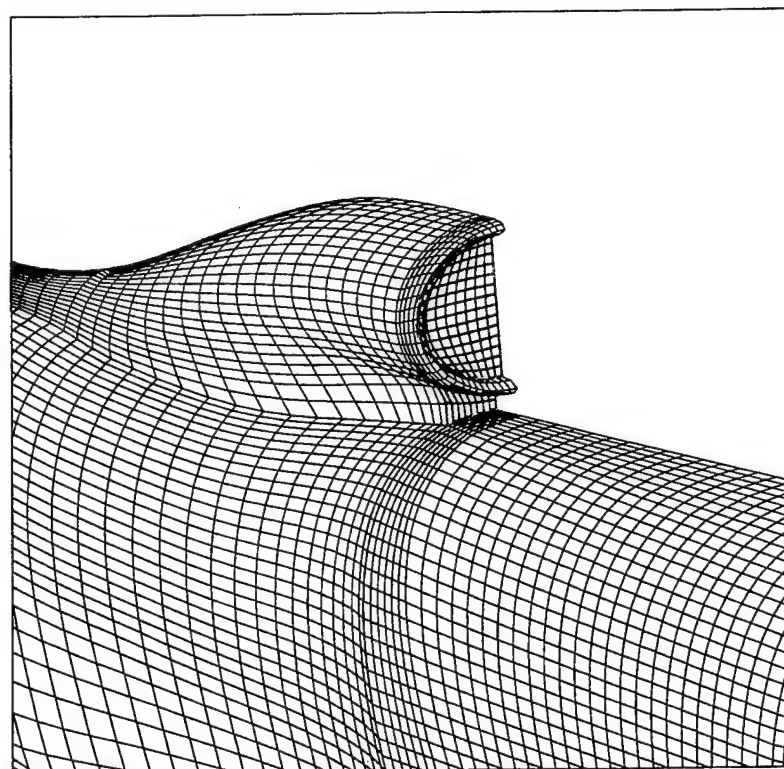


Figure 3 Grid on Top Midsection. Main Engine Inlet and Auxiliary Inlet
Shown in Red. (Right Half of Aircraft Shown.)

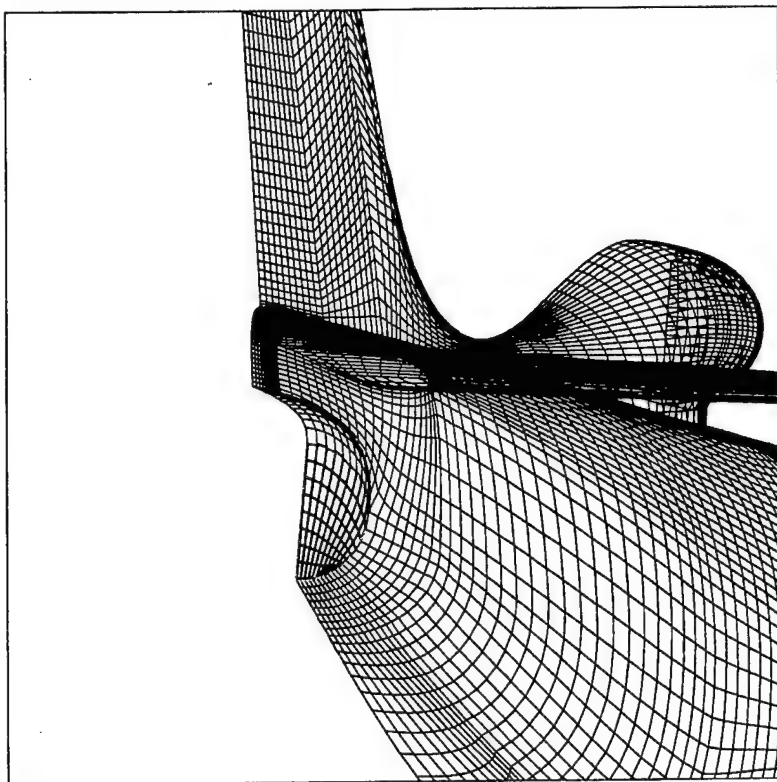


Figure 4 Aft End of Half of Aircraft. Engine Exhaust Face Shown in Red

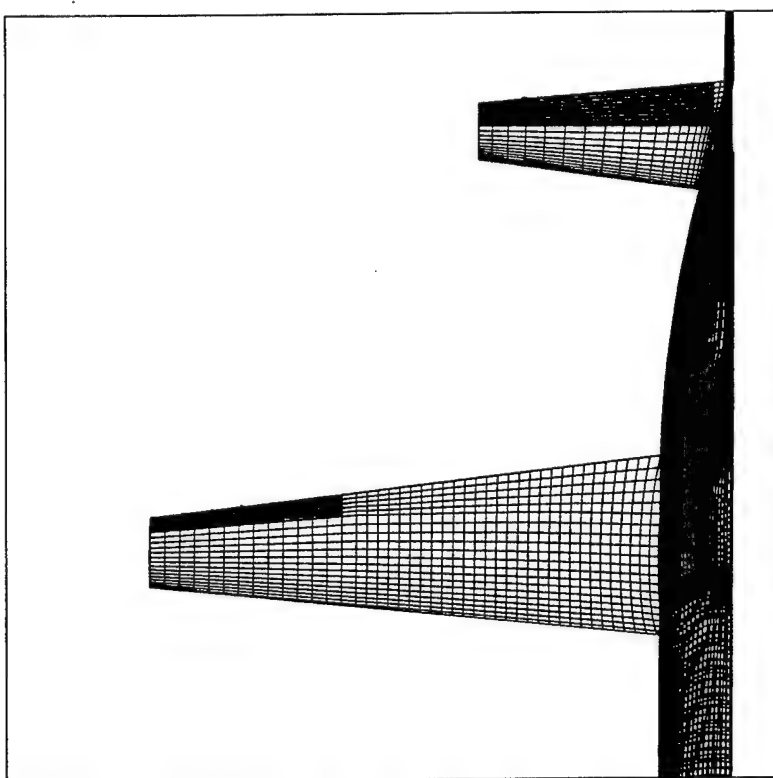


Figure 5 Top View of Right Half, Ailerons and Elevator Shown in Red

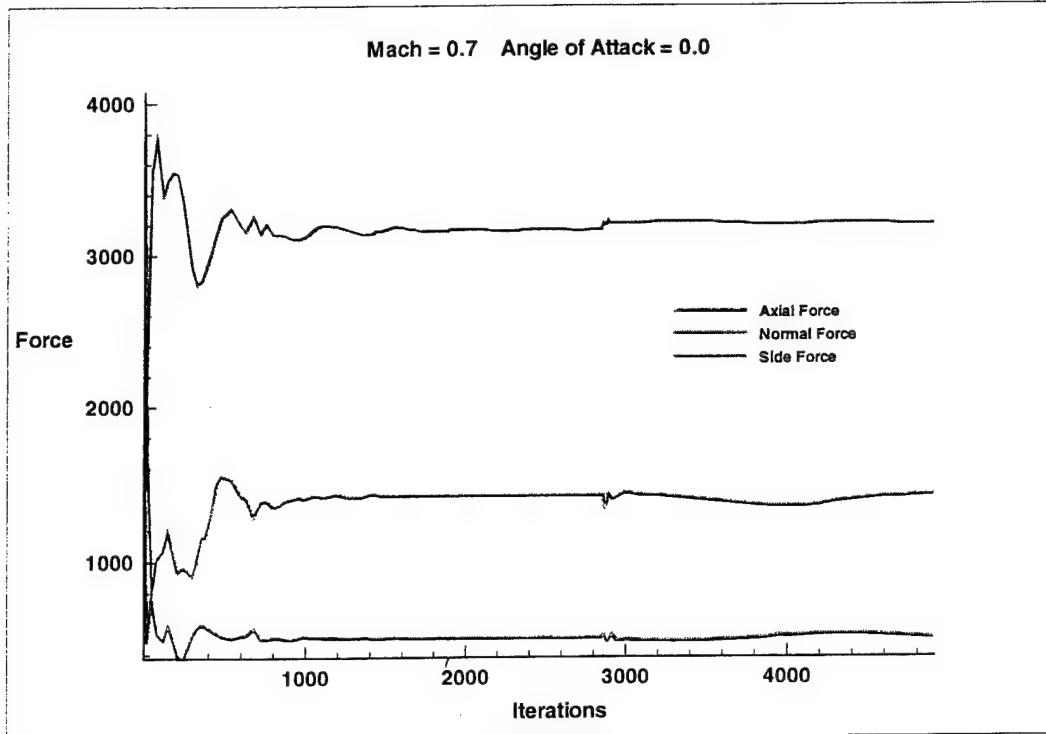


Figure 6 Convergence History for Mach = 0.7, Angle of Attack = 0.0

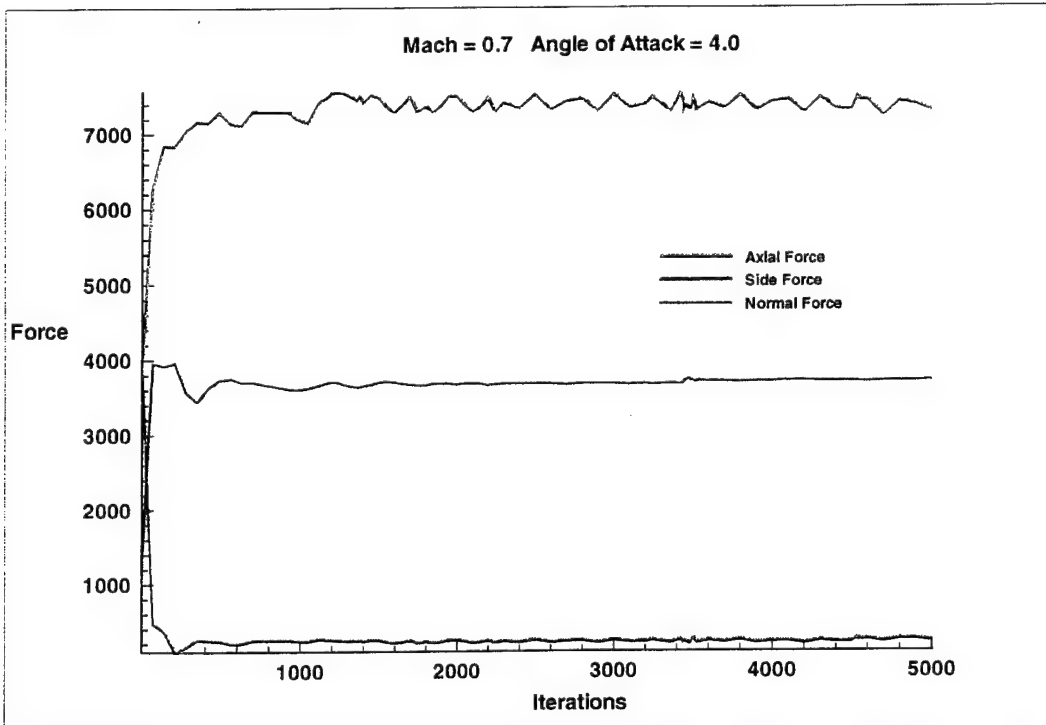


Figure 7 Convergence History for Mach = 0.7, Angle of Attack = 4.0

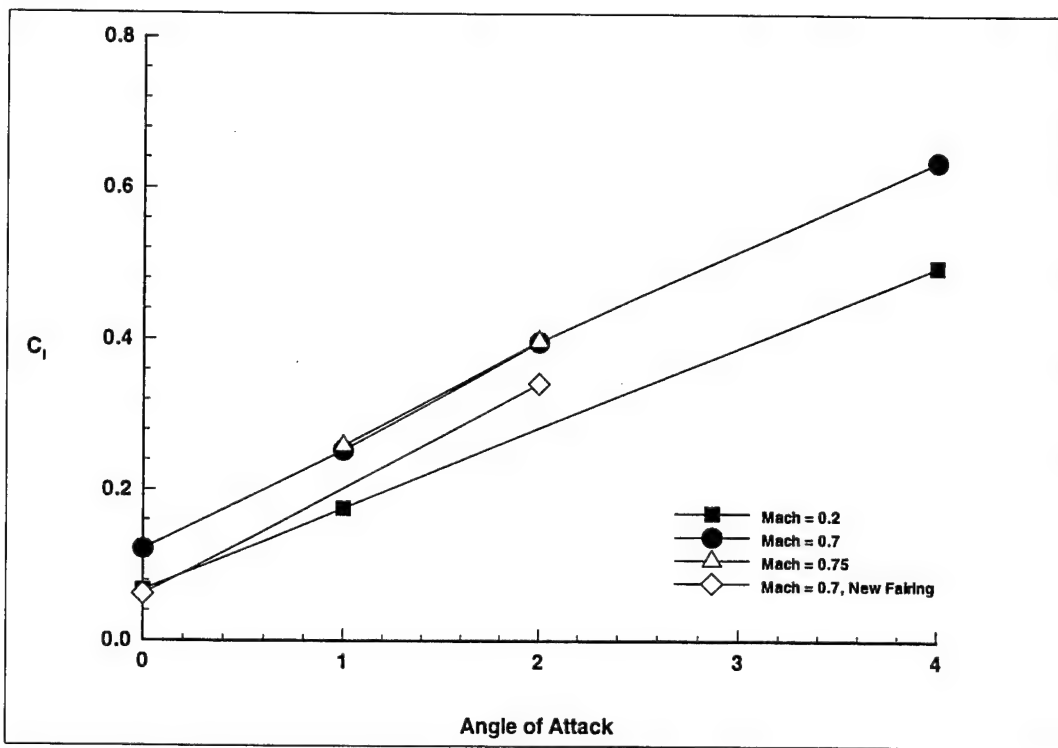


Figure 8 Lift Coefficient versus Angle of Attack

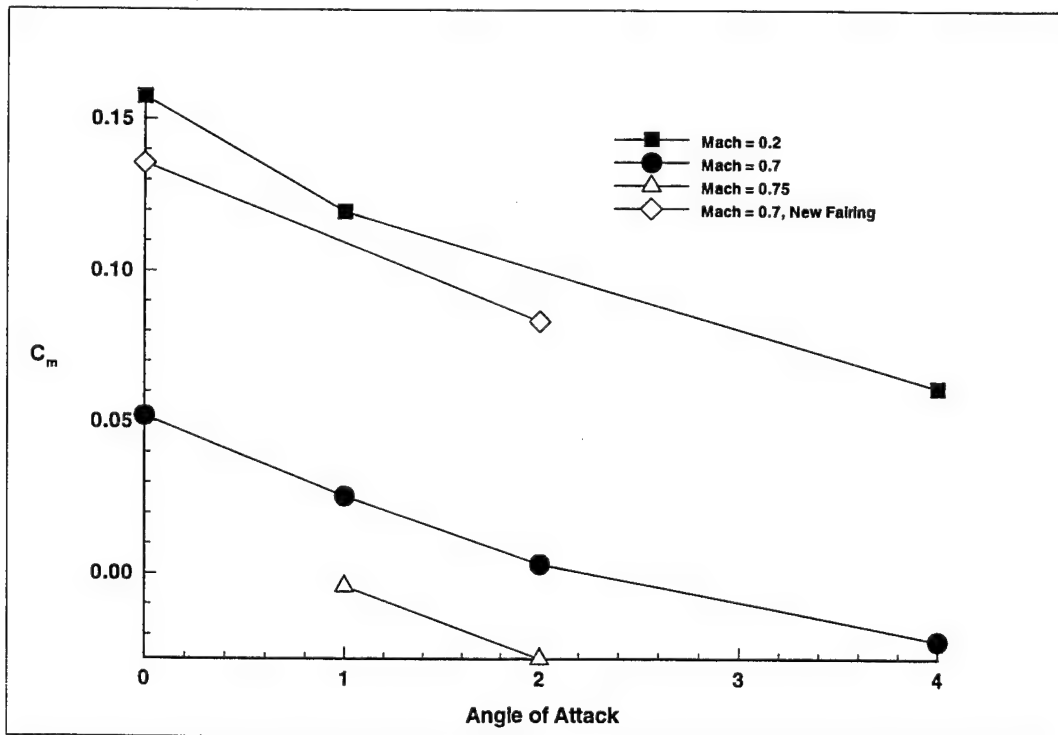


Figure 9 Pitch Coefficient versus Angle of Attack

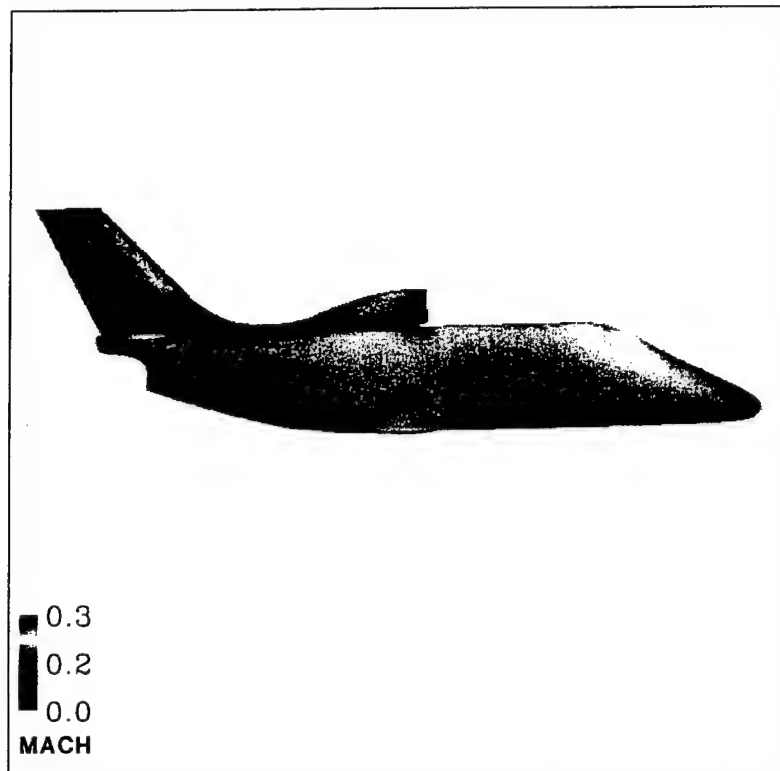


Figure 11 Front View, Mach = 0.2, Angle of Attack = 0.0

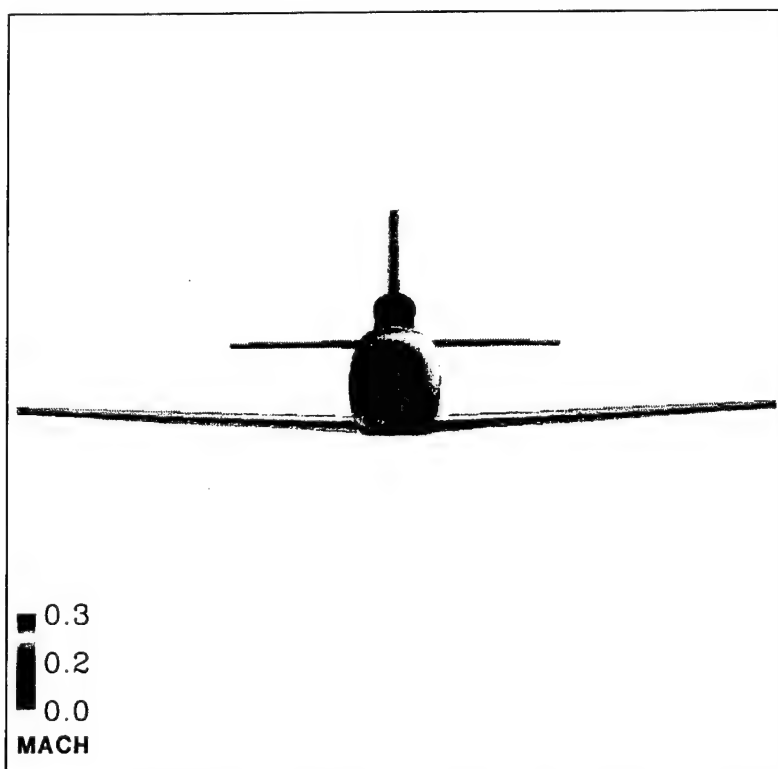


Figure 10 Side View, Mach = 0.2, Angle of Attack = 0.0

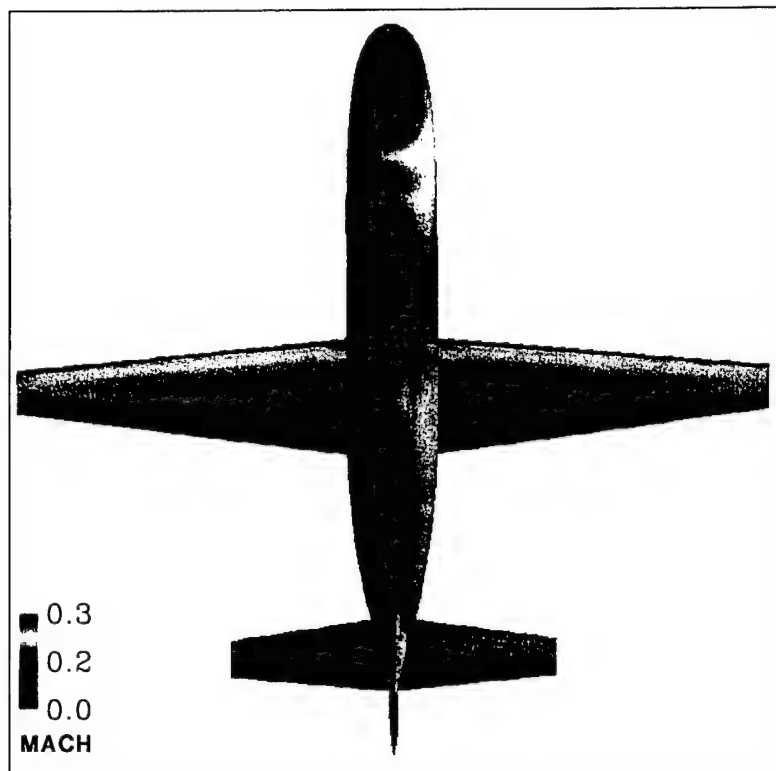


Figure 12 Top View, Mach = 0.2, Angle of Attack = 0.0

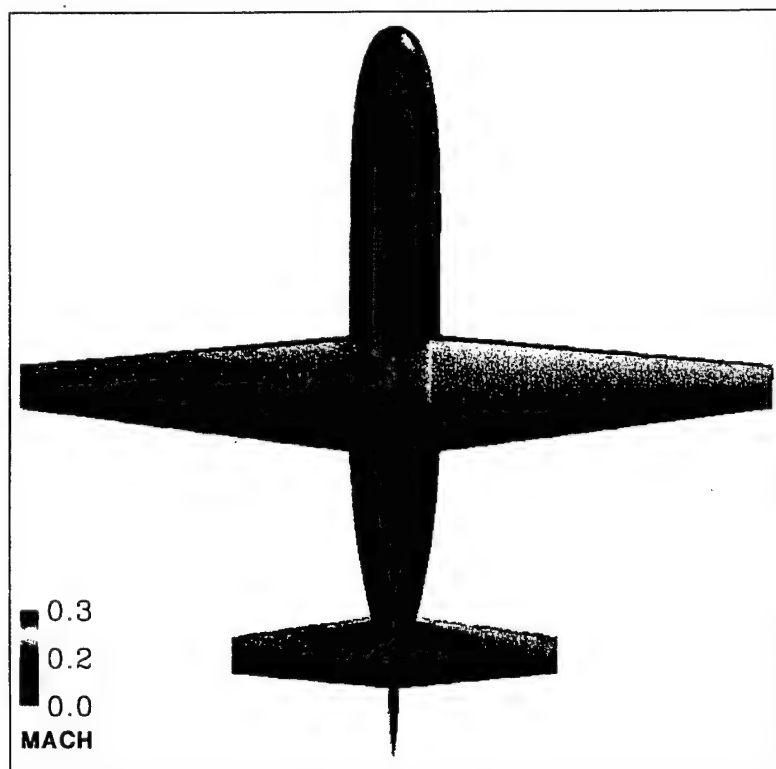


Figure 13 Bottom View, Mach = 0.2, Angle of Attack = 0.0

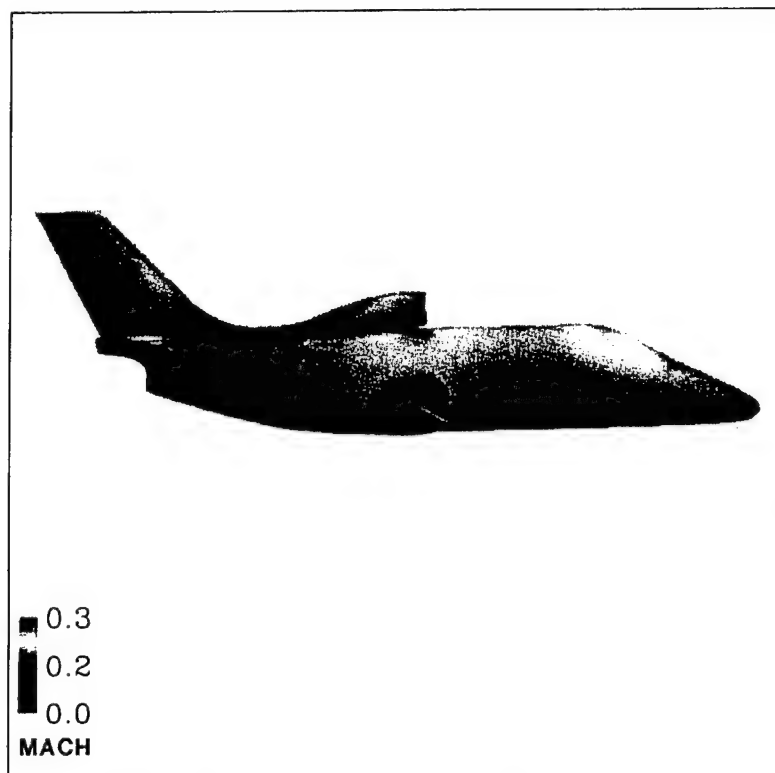


Figure 14 Side View, Mach = 0.2, Angle of Attack = 4.0

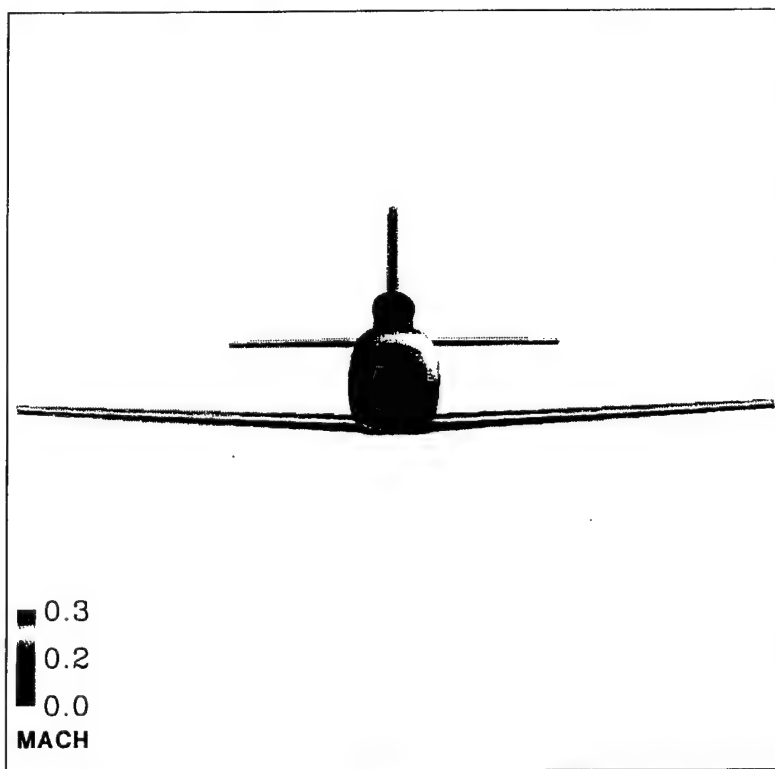


Figure 15 Front View, Mach = 0.2, Angle of Attack = 4.0

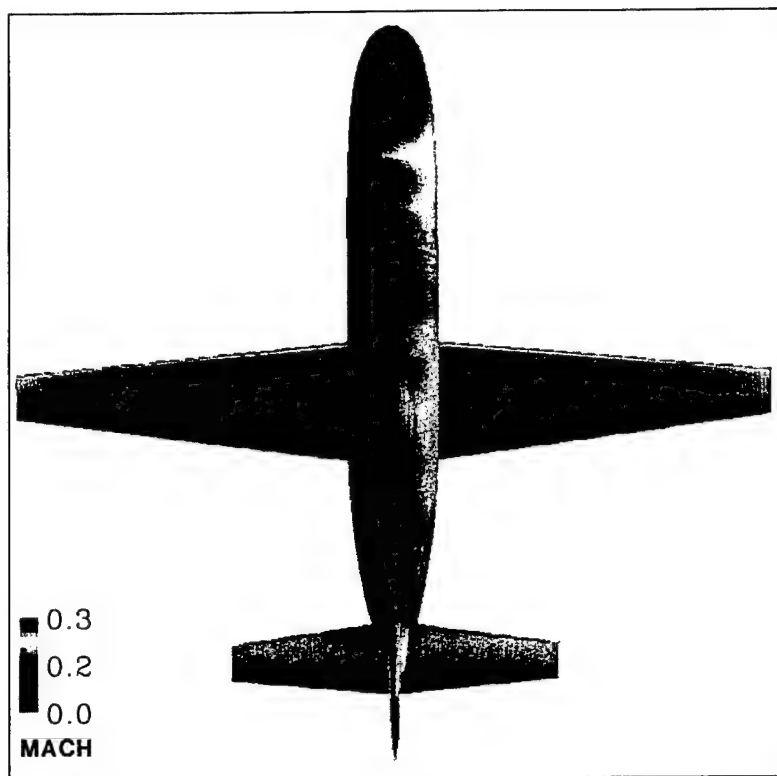


Figure 16 Top View, Mach = 0.2, Angle of Attack = 4.0

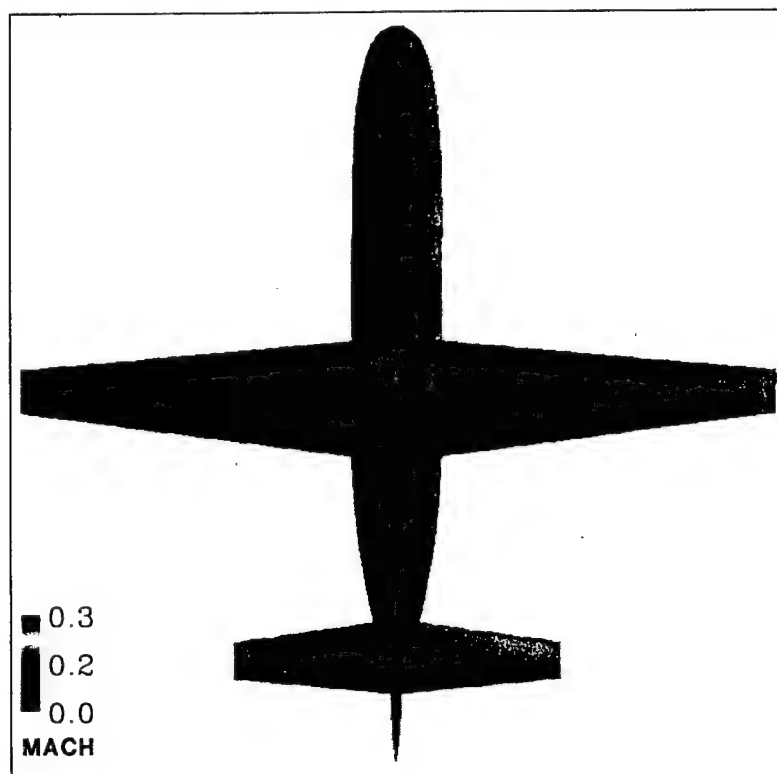


Figure 17 Bottom View, Mach = 0.2, Angle of Attack = 4.0

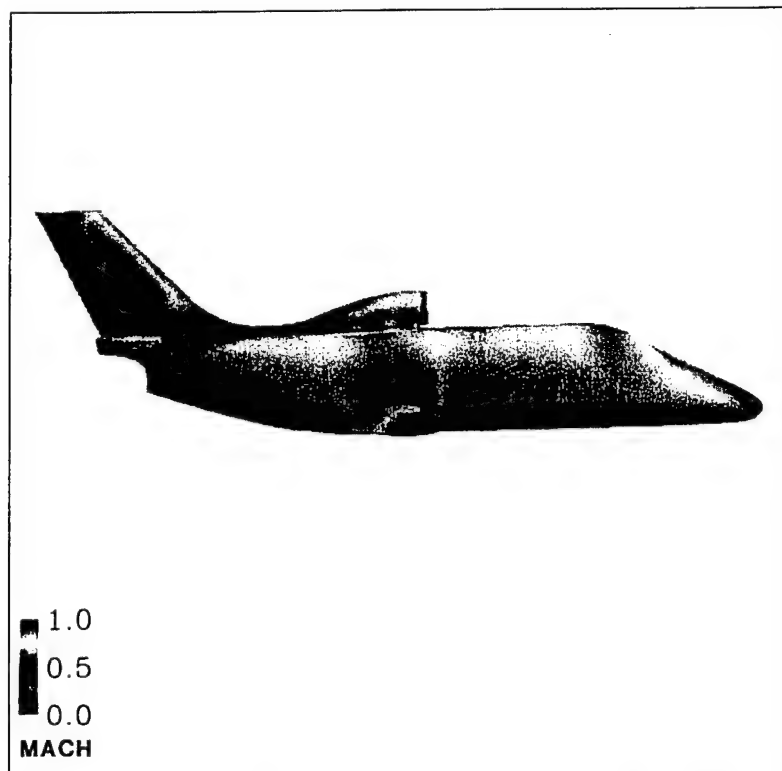


Figure 18 Side View, Mach = 0.7, Angle of Attack = 0.0

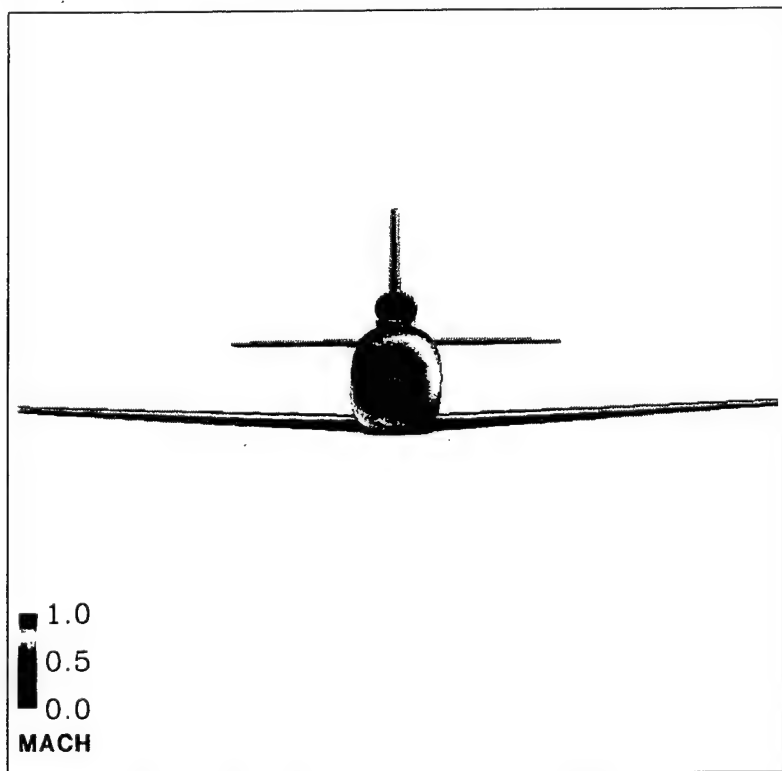


Figure 19 Front View, Mach = 0.7, Angle of Attack = 0.0

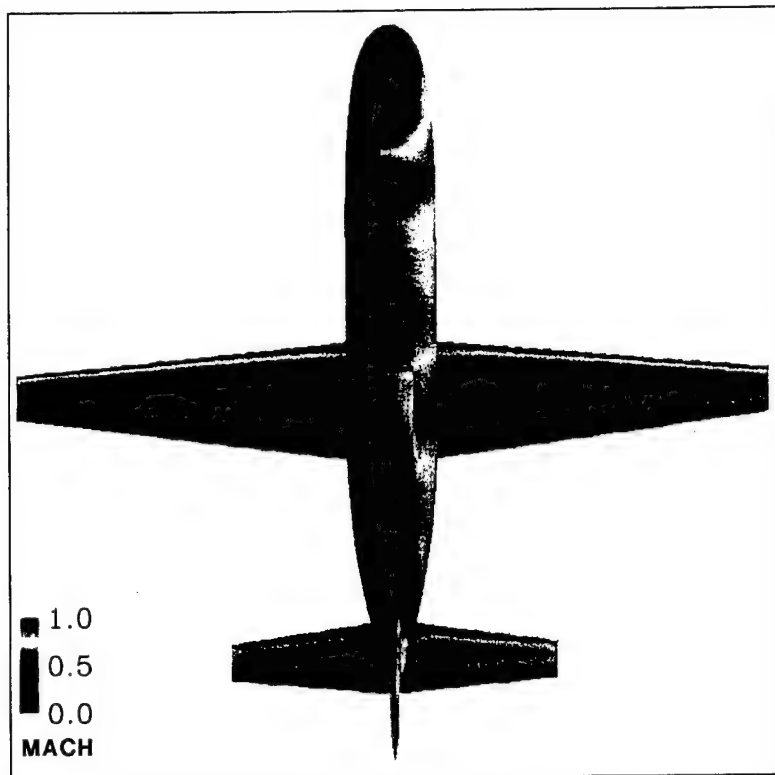


Figure 20 Top View, Mach = 0.7, Angle of Attack = 0.0

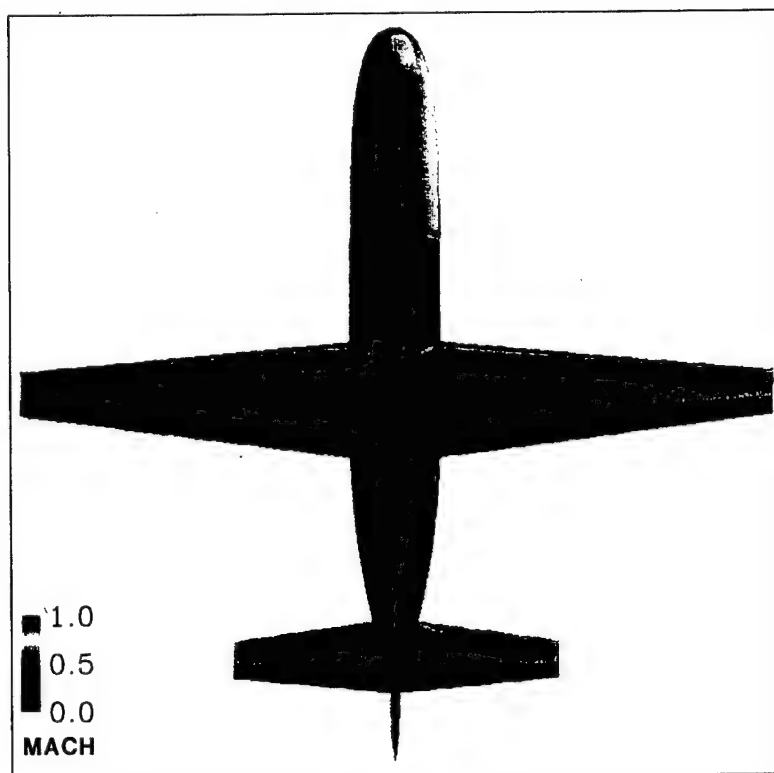


Figure 21 Bottom View, Mach = 0.7, Angle of Attack = 0.0

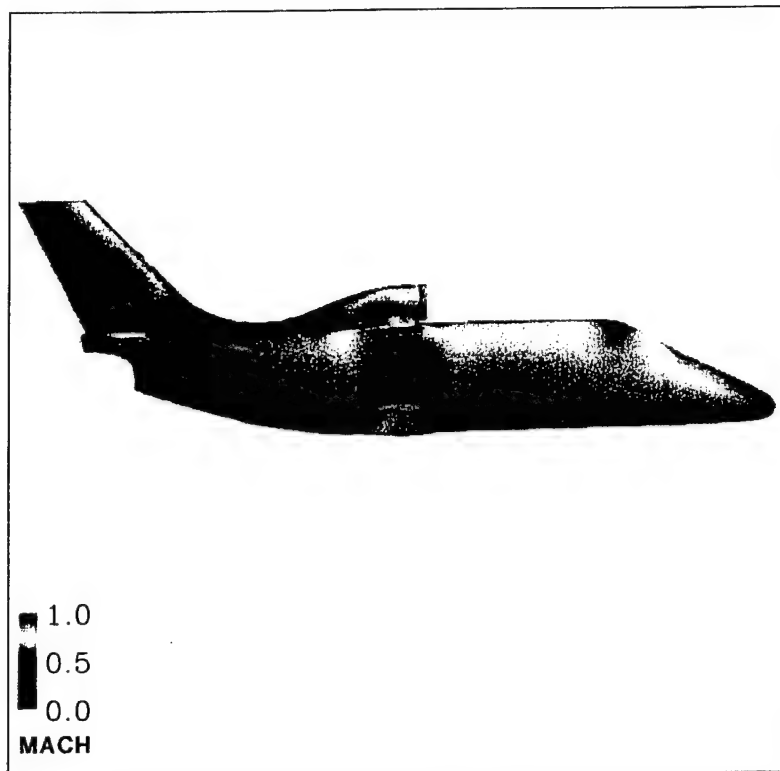


Figure 22 Side View, Mach = 0.7, Angle of Attack = 4.0

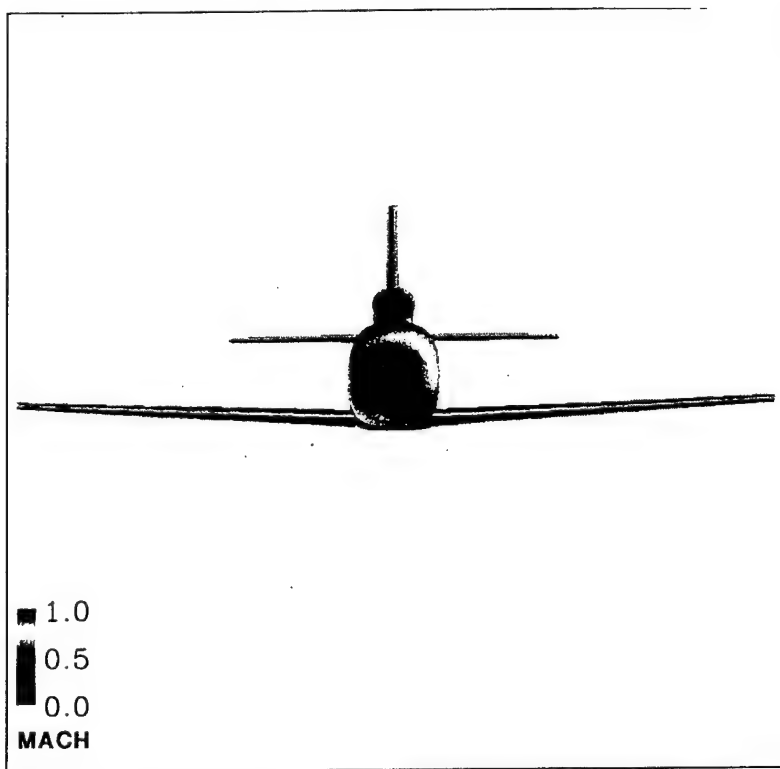


Figure 23 Front View, Mach = 0.7, Angle of Attack = 4.0

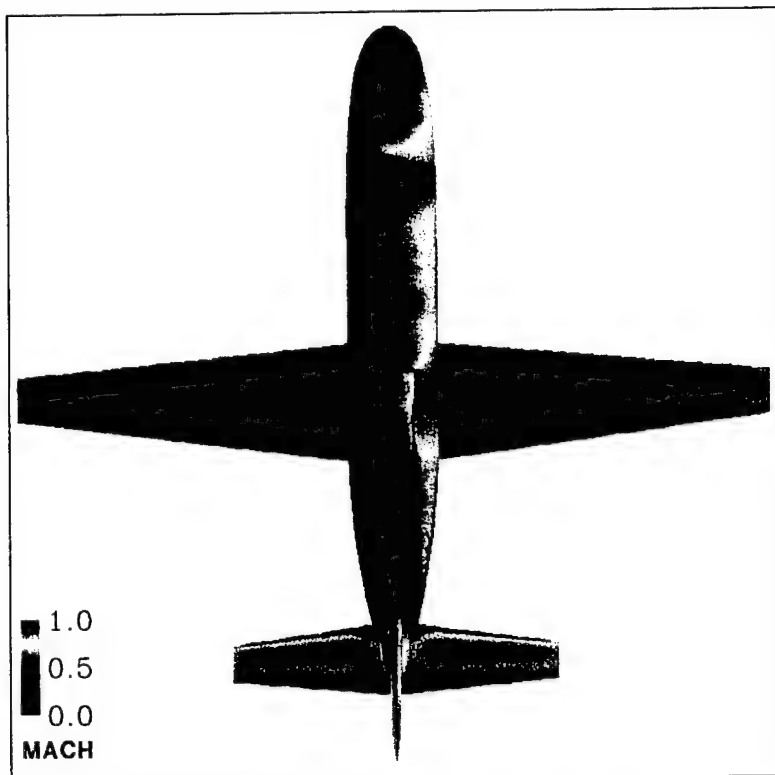


Figure 24 Top View, Mach = 0.7, Angle of Attack = 4.0

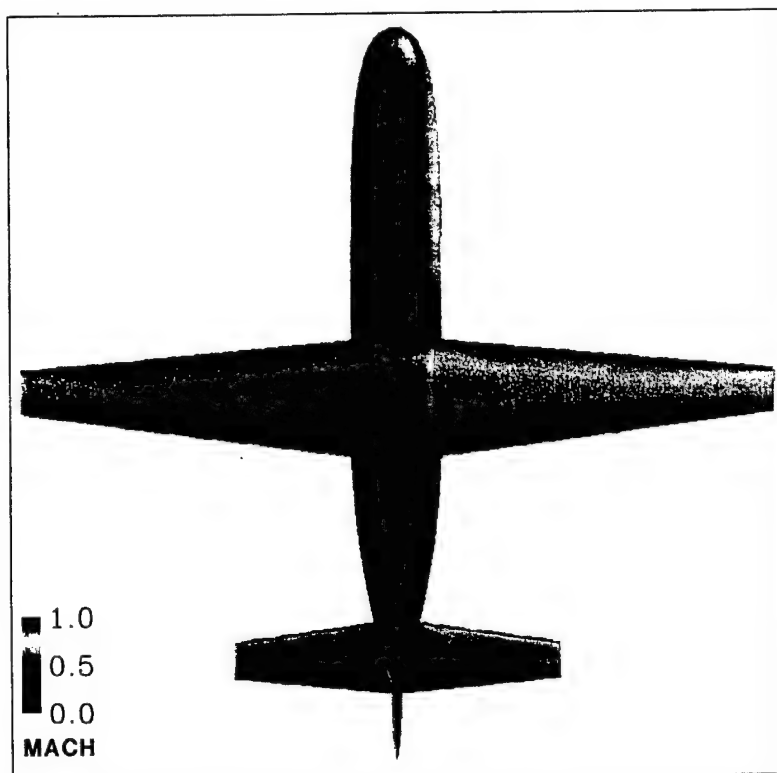


Figure 25 Bottom View, Mach = 0.7, Angle of Attack = 4.0

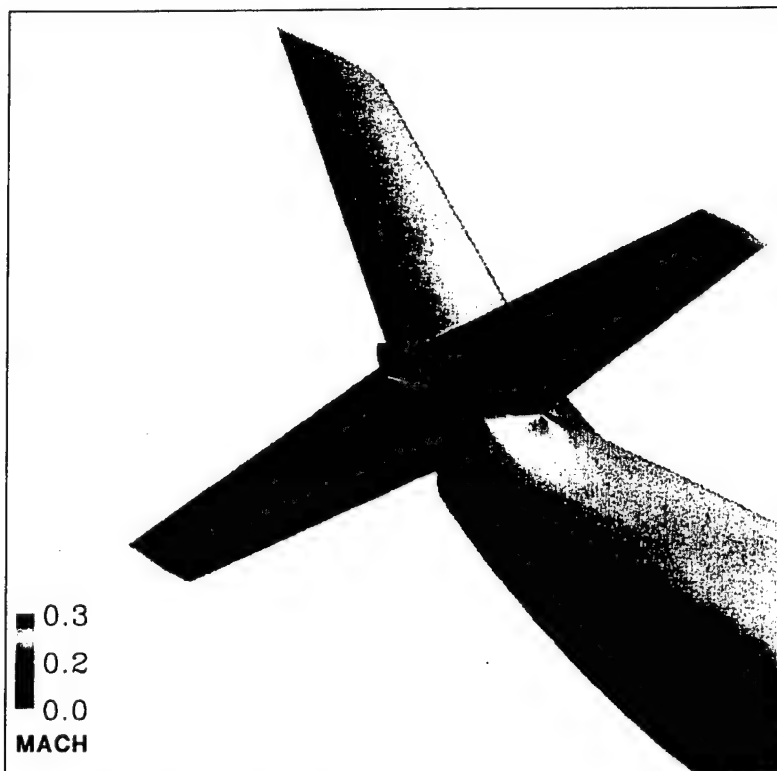


Figure 26 Underside View of Aircraft with Mach Contours.

Mach = 0.2, Angle of Attack = 0.0

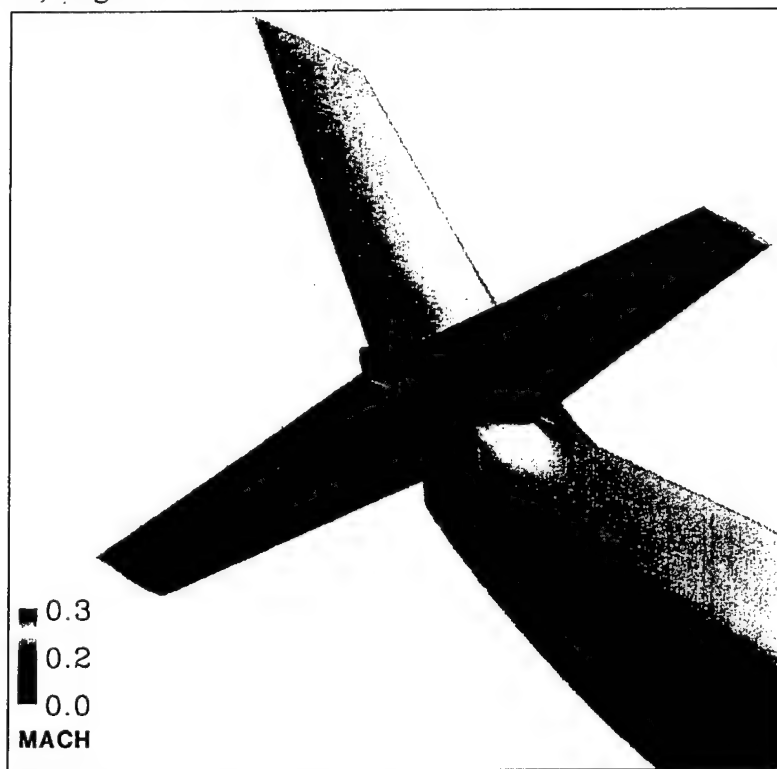
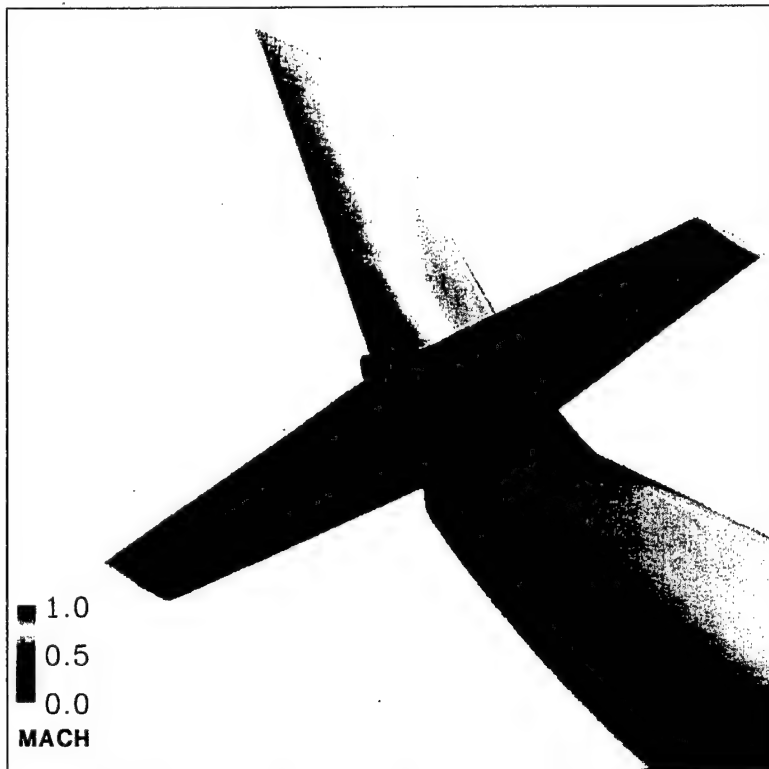
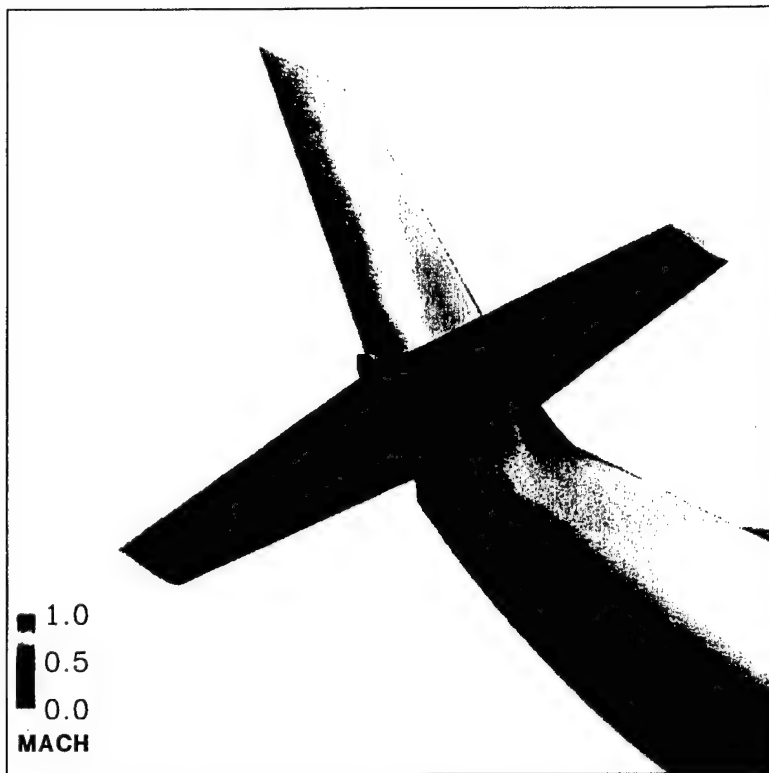


Figure 27 Underside View of Aircraft with Mach Contours.

Mach = 0.2, Angle of Attack = 4.0



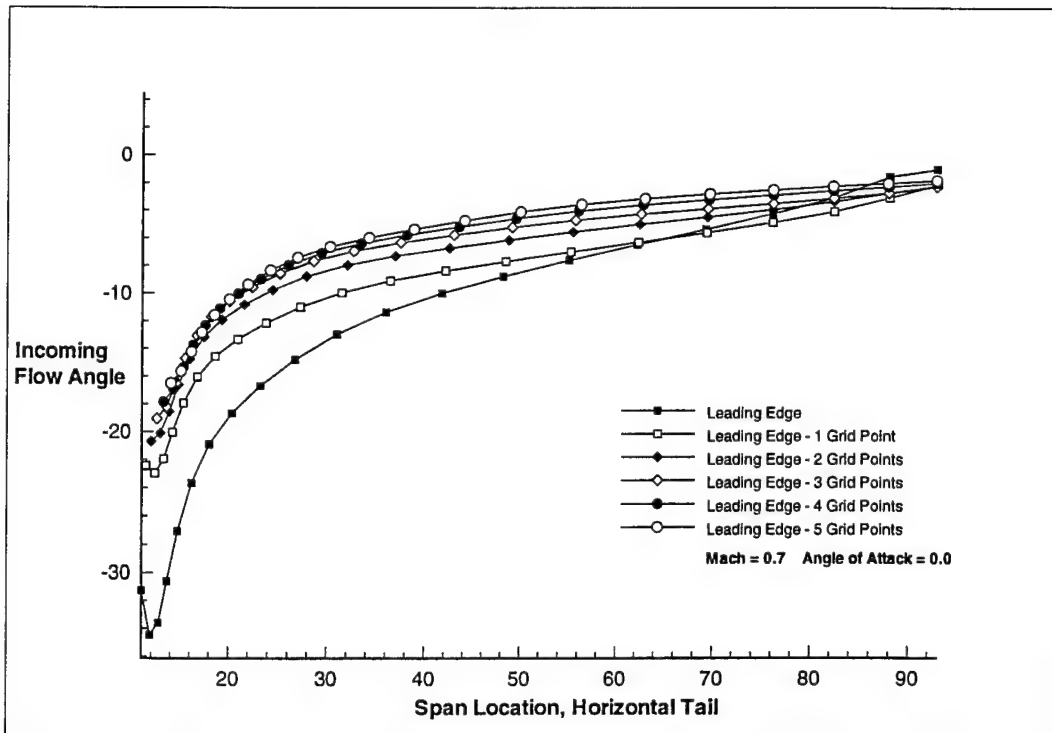


Figure 30 Plot of Incoming Flow Angle versus Span Location on Horizontal Tail. Mach = 0.7, Angle of Attack = 0.0

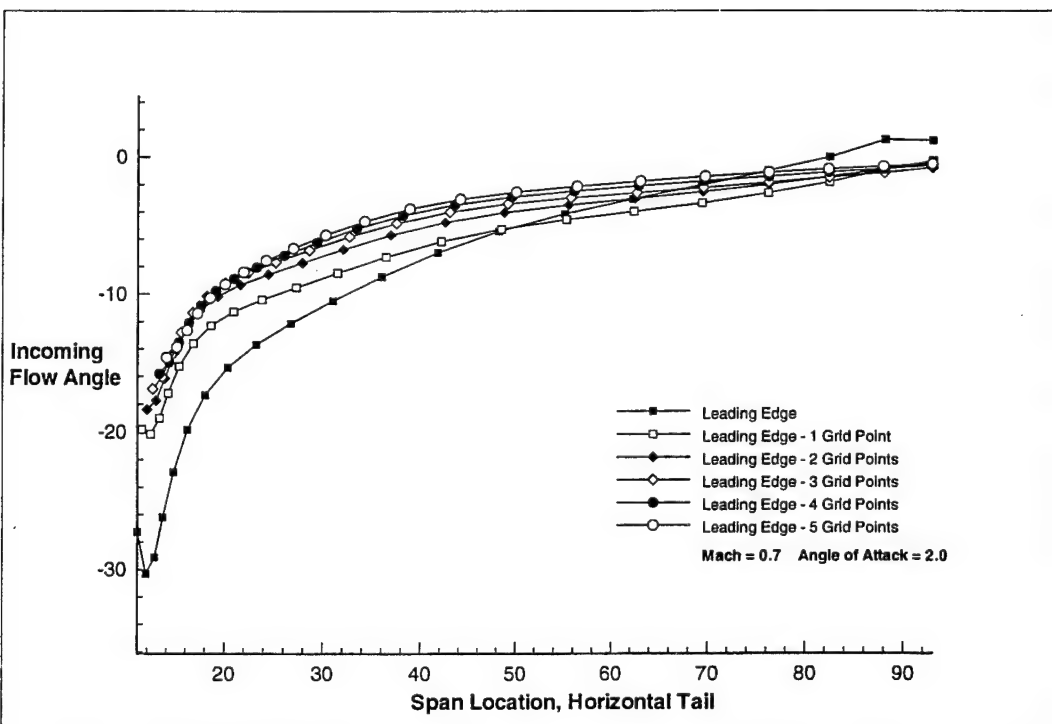


Figure 31 Plot of Incoming Flow Angle versus Span Location on Horizontal Tail. Mach = 0.7, Angle of Attack = 2.0

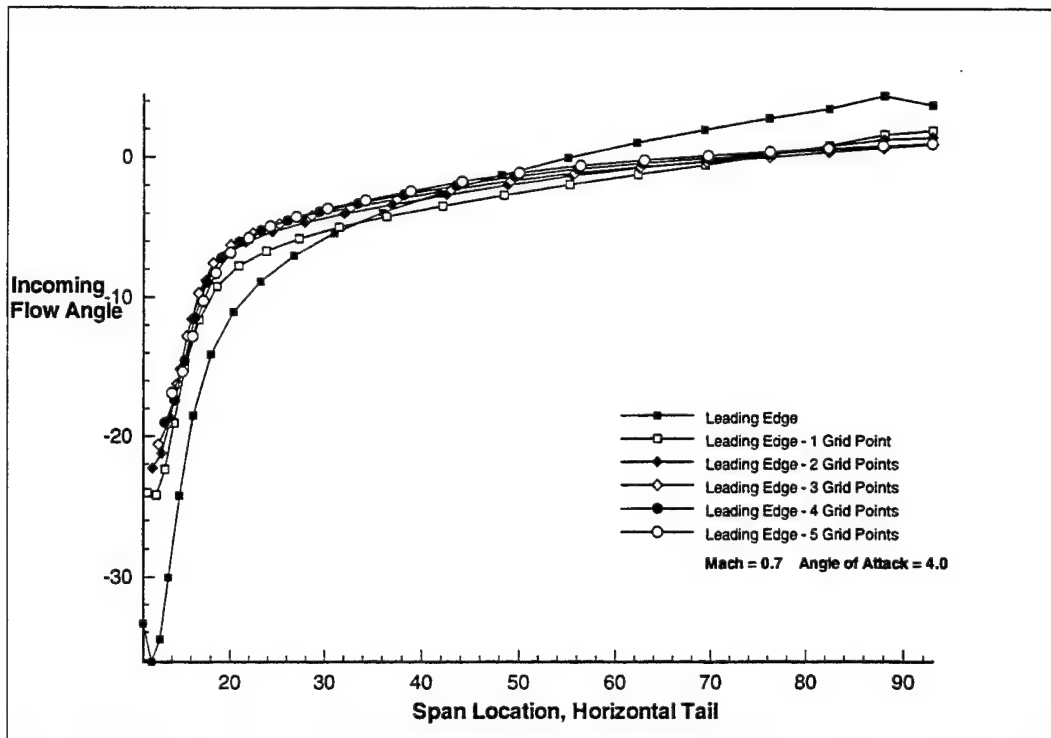


Figure 32 Plot of Incoming Flow Angle versus Span Location on Horizontal Tail. Mach = 0.7, Angle of Attack = 4.0

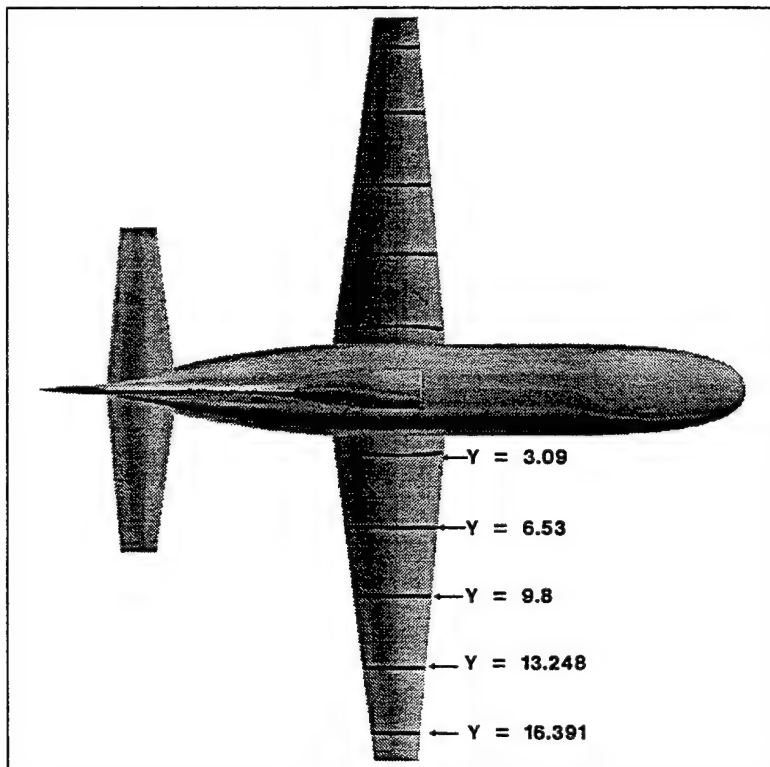


Figure 33 Wing Span Location of Cp Plots

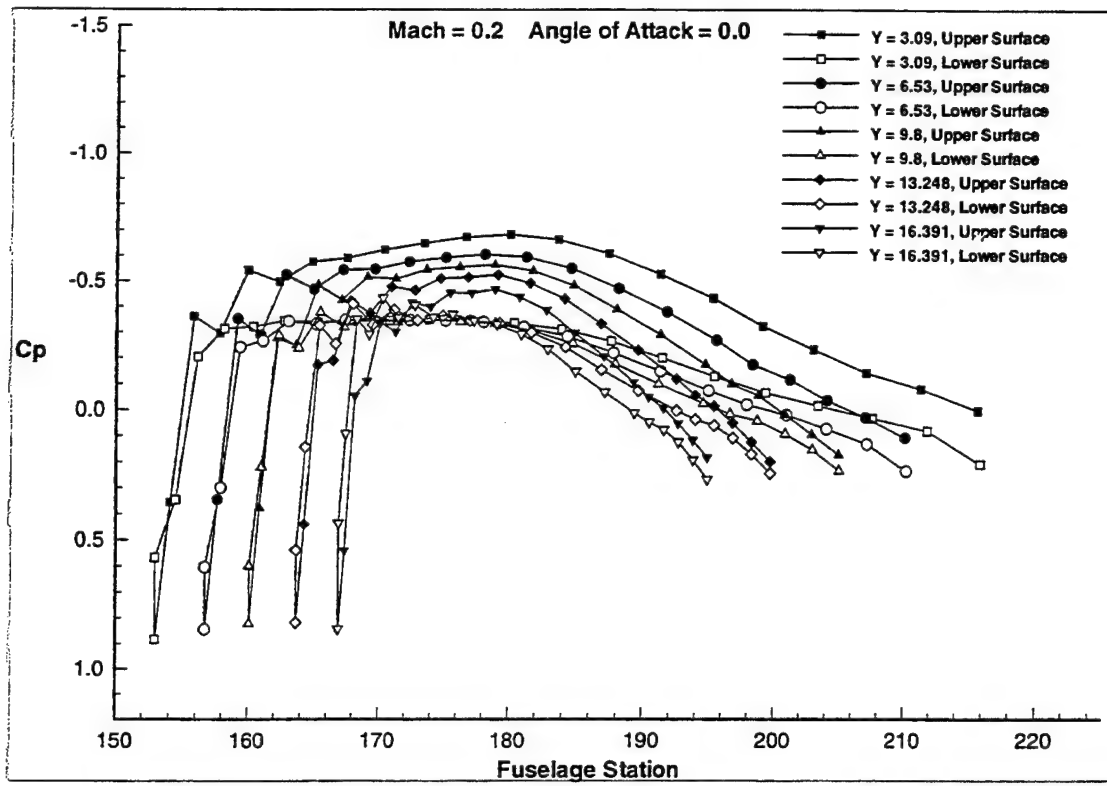


Figure 34 Wing Cp. Mach = 0.2, Angle of Attack = 0.0

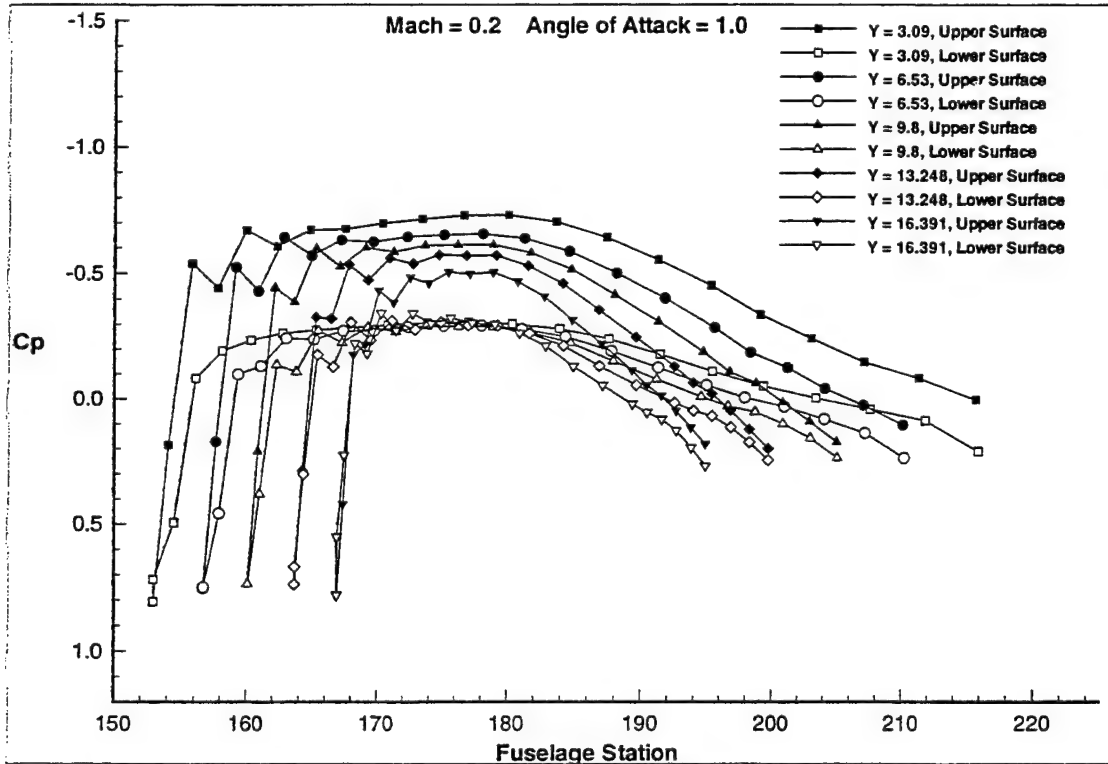


Figure 35 Wing Cp. Mach = 0.2, Angle of Attack = 1.0

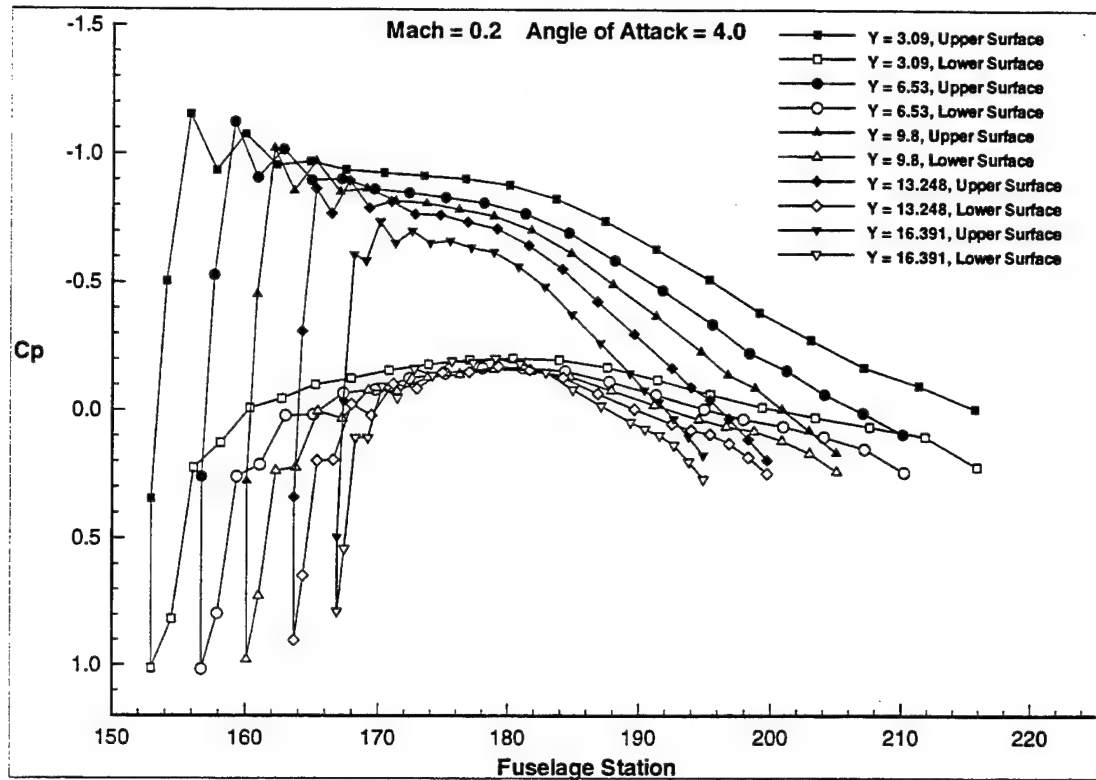


Figure 36 Wing Cp. Mach = 0.2, Angle of Attack = 4.0

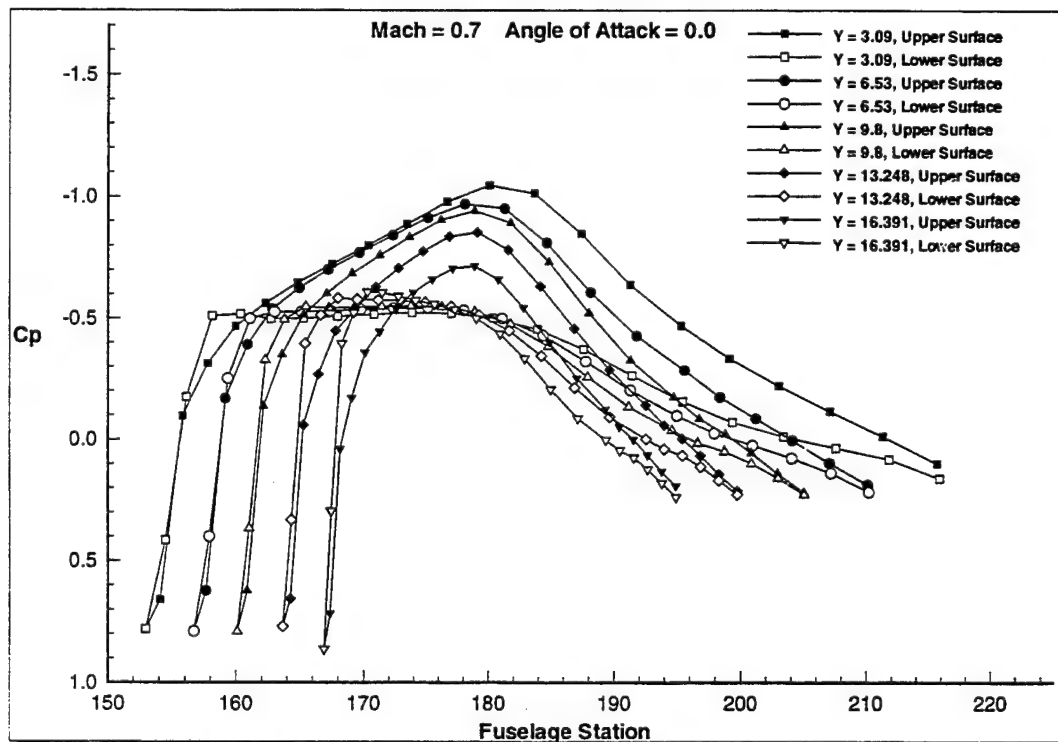


Figure 37 Wing Cp. Mach = 0.7, Angle of Attack = 0.0

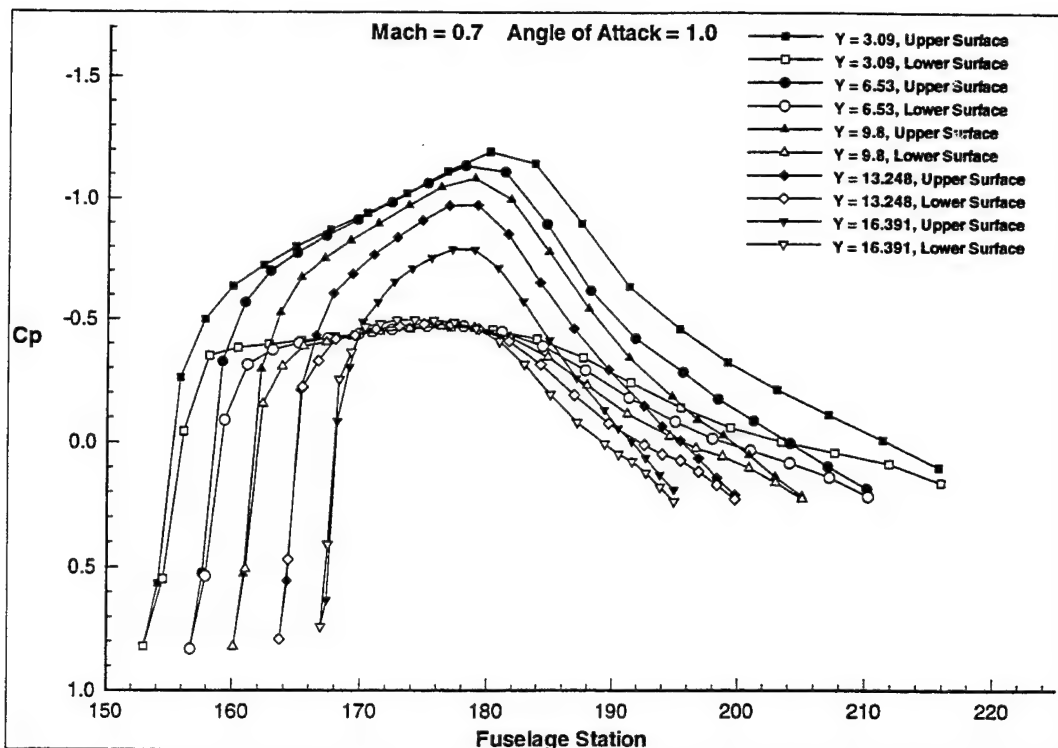


Figure 38 Wing Cp. Mach = 0.7, Angle of Attack = 1.0

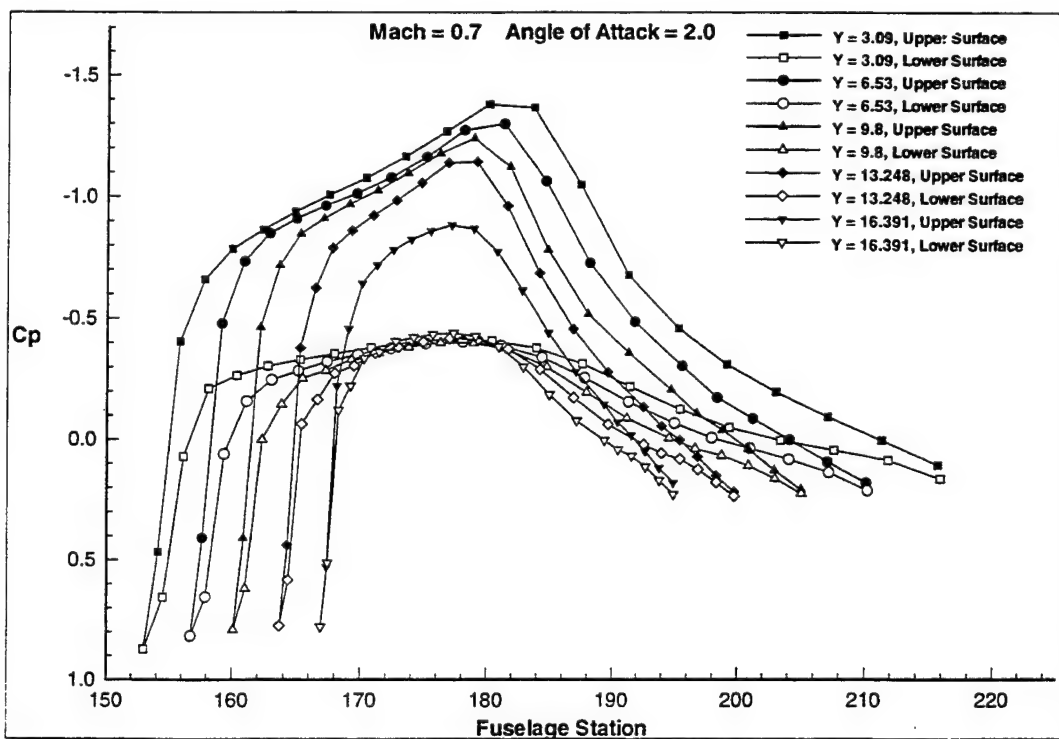


Figure 39 Wing Cp. Mach = 0.7, Angle of Attack = 2.0

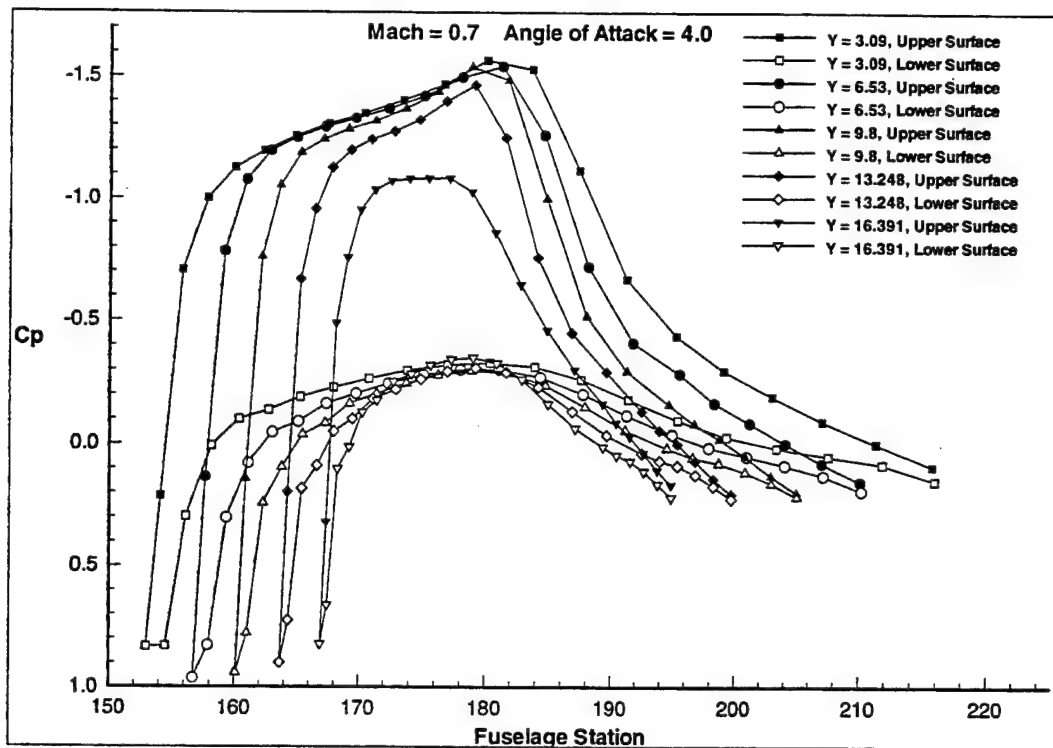


Figure 40 Wing Cp. Mach = 0.7, Angle of Attack = 4.0

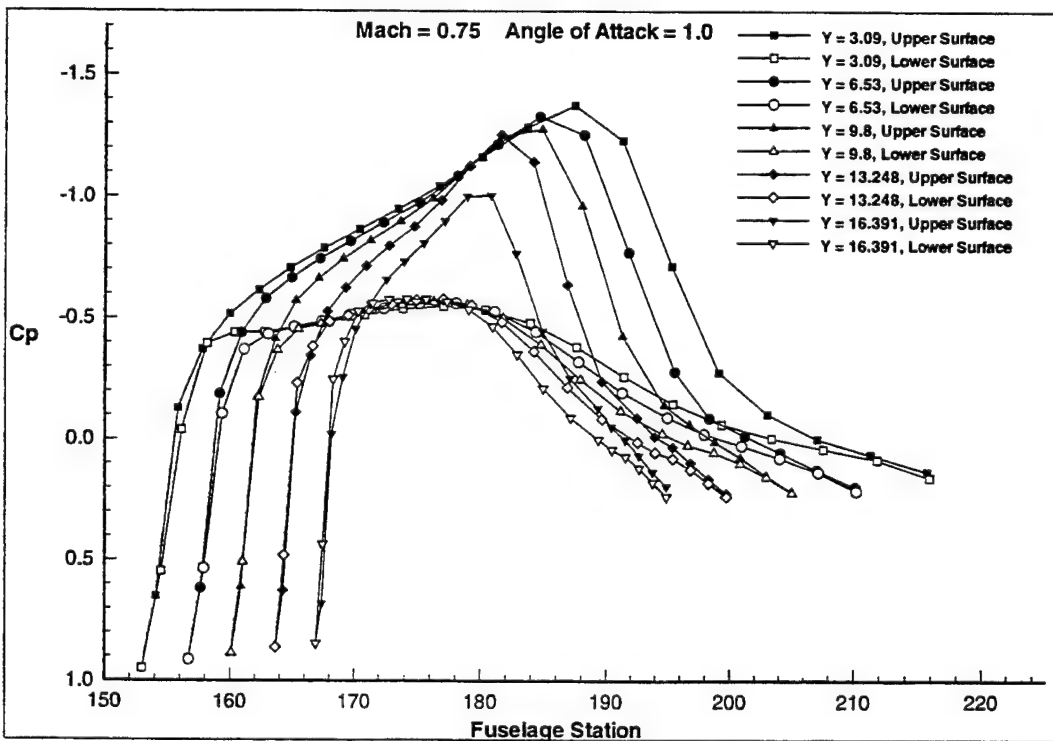


Figure 41 Wing Cp. Mach = 0.75, Angle of Attack = 1.0

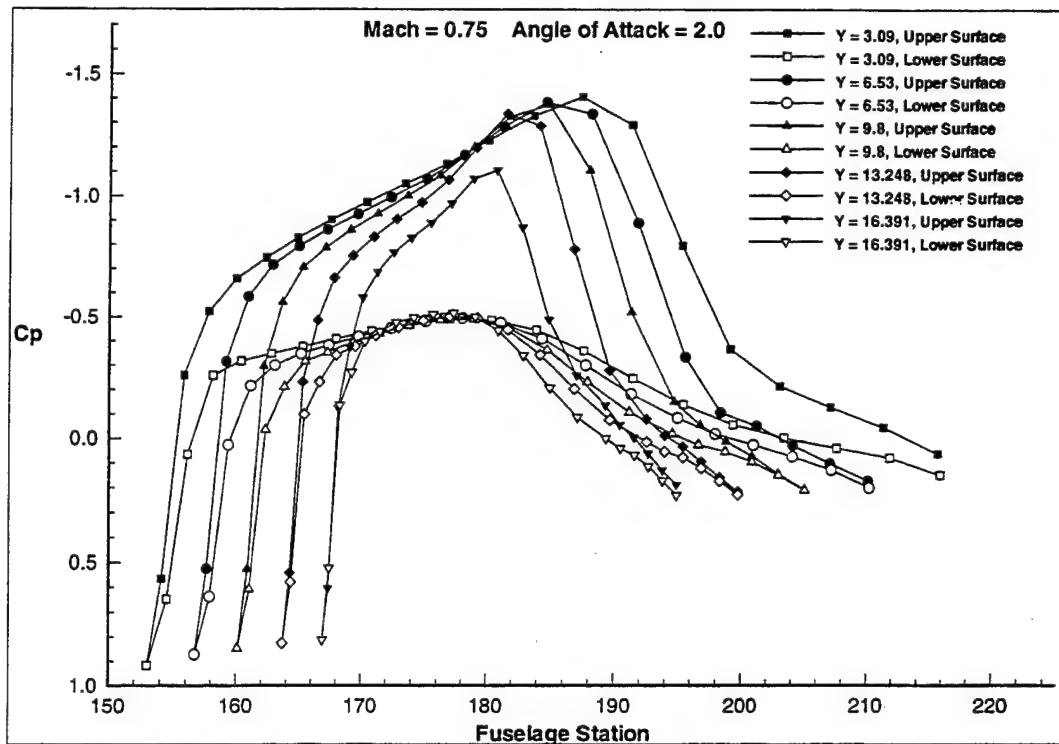


Figure 42 Wing Cp. Mach = 0.75, Angle of Attack = 2.0

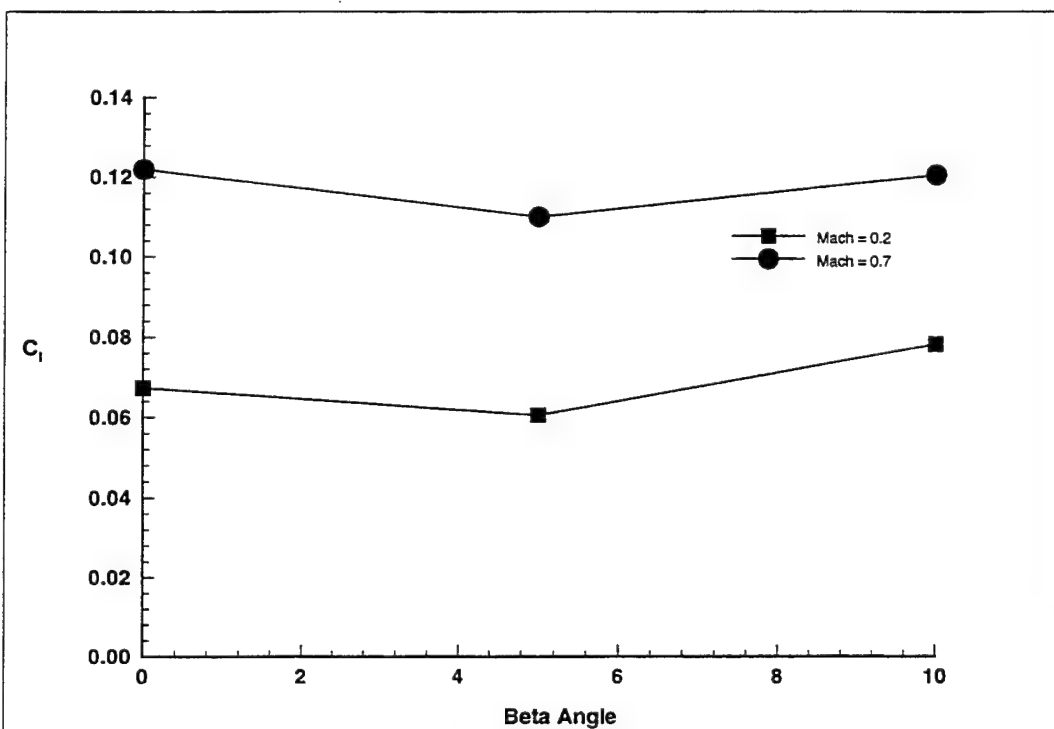


Figure 43 Lift Coefficient versus Beta Angle

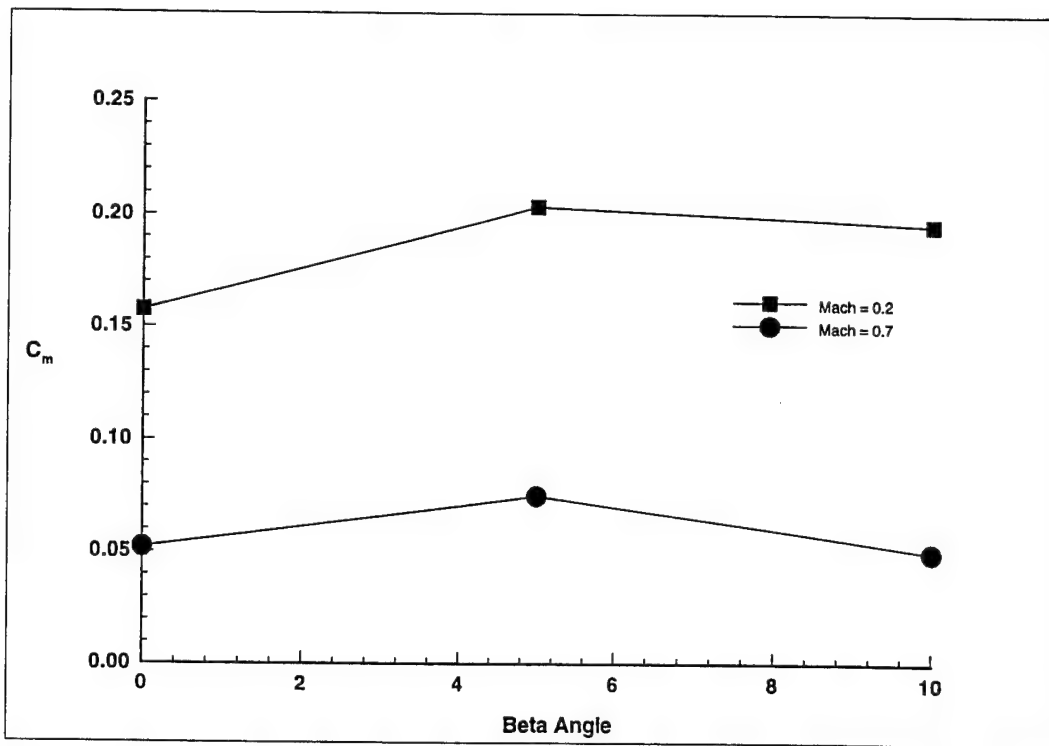


Figure 44 Pitch Coefficient versus Beta Angle

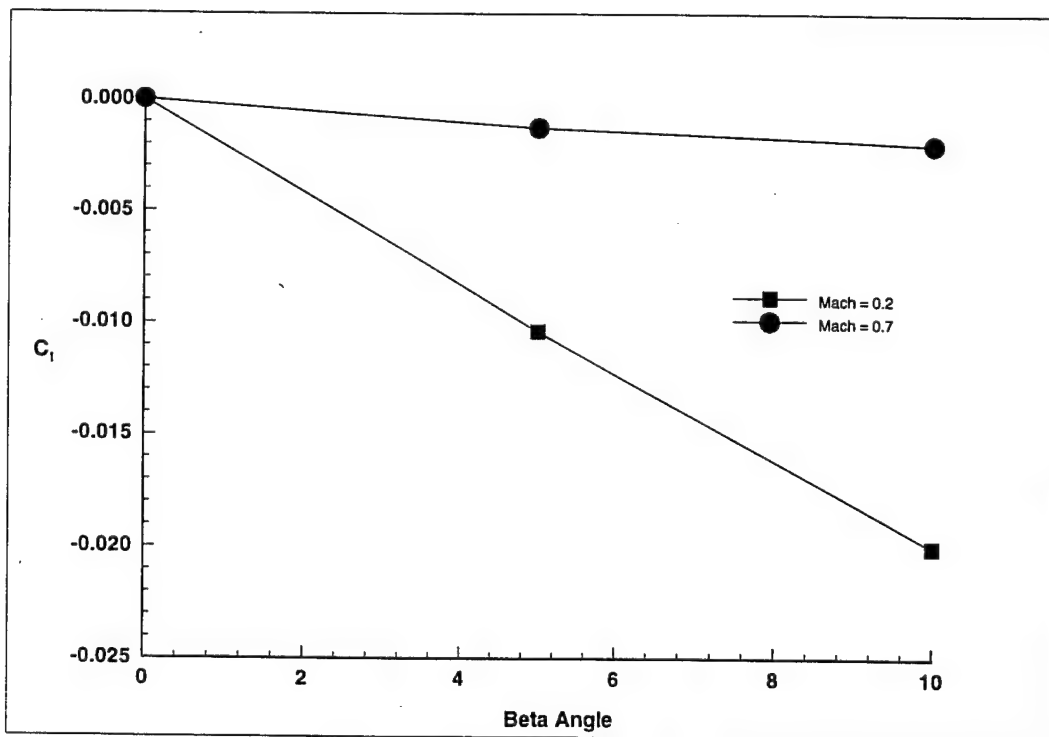


Figure 45 Roll Coefficient versus Beta Angle

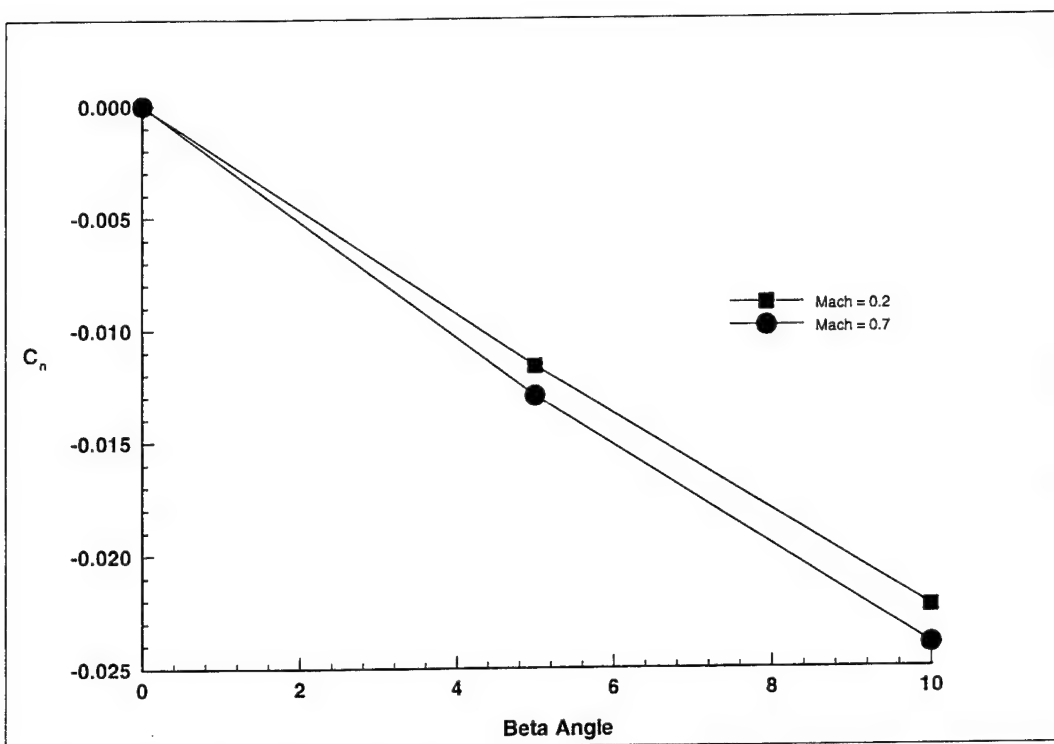


Figure 46 Yaw Coefficient versus Beta Angle

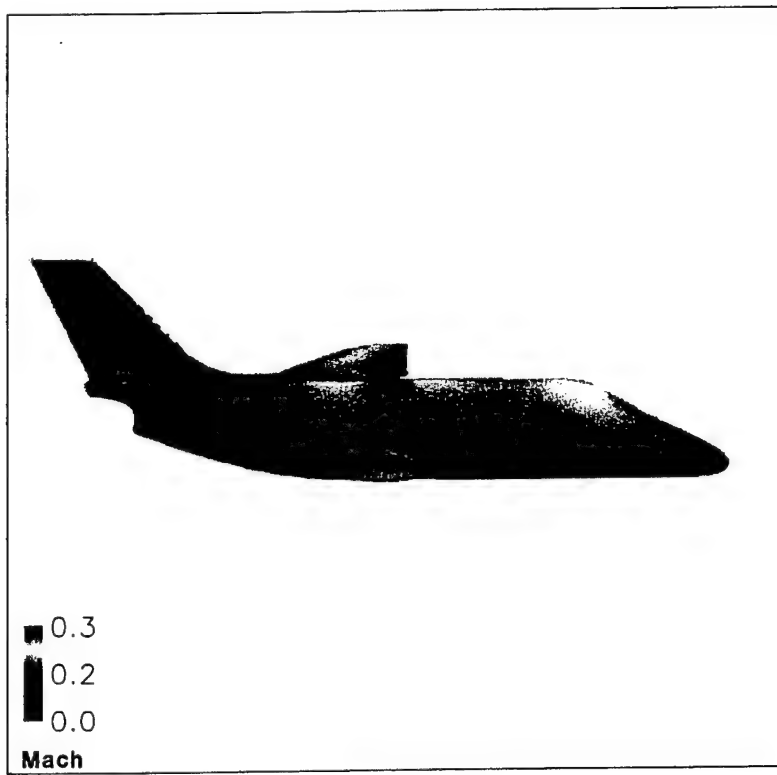


Figure 47 Windward Side, Mach = 0.20, Angle of Attack = 0.0, Beta = 5.0

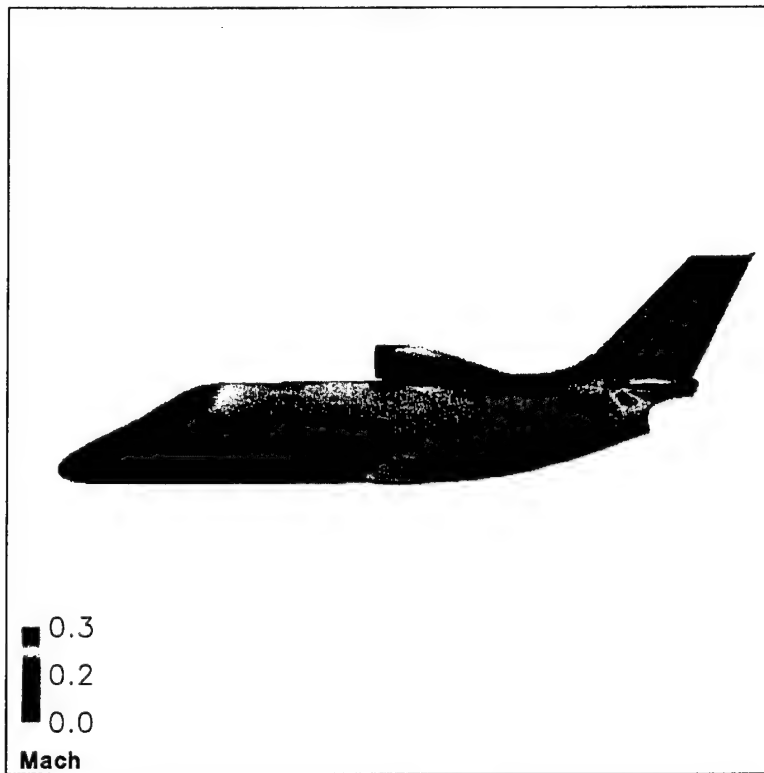


Figure 48 Leeward Side, Mach = 0.20, Angle of Attack = 0.0, Beta = 5.0

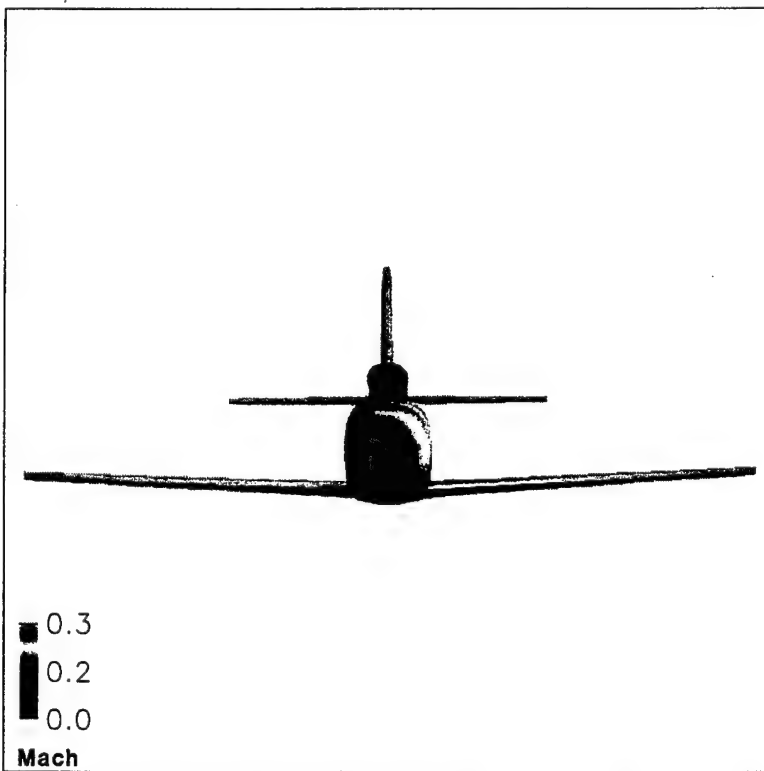


Figure 49 Front View, Mach = 0.20, Angle of Attack = 0.0, Beta = 5.0

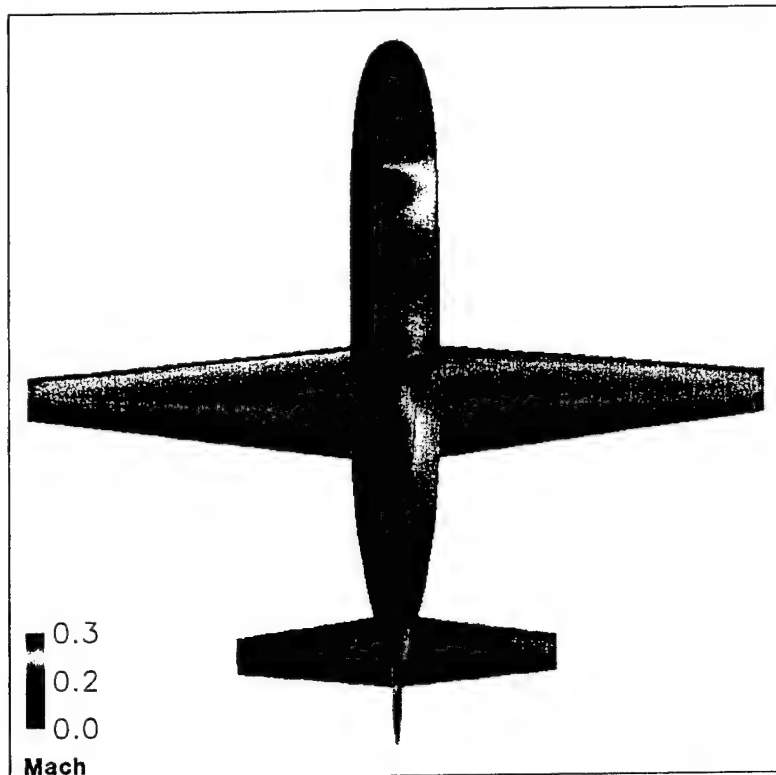


Figure 50 Top View, Mach = 0.20, Angle of Attack = 0.0, Beta = 5.0

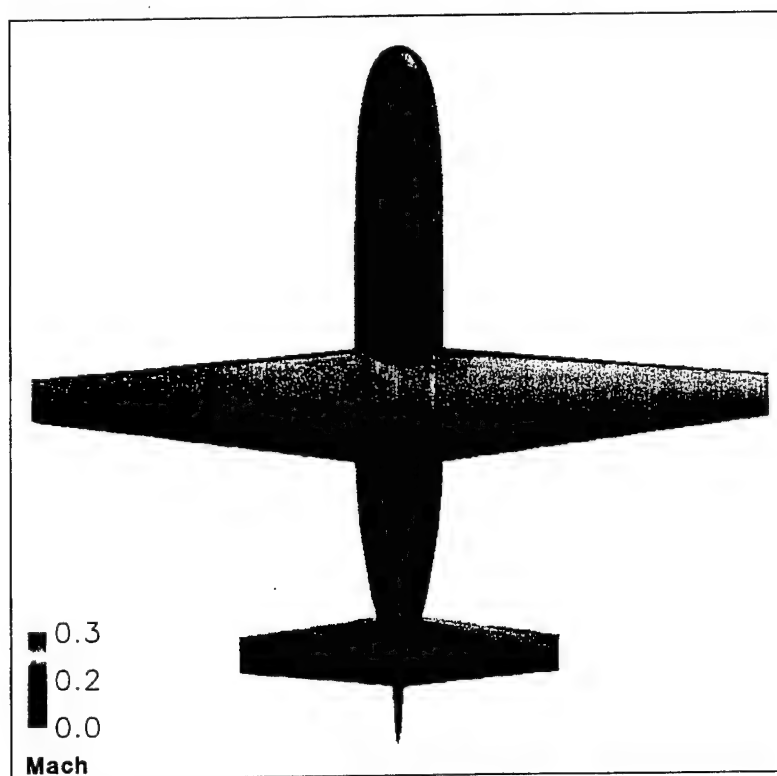


Figure 51 Bottom View, Mach = 0.20, Angle of Attack = 0.0, Beta = 5.0

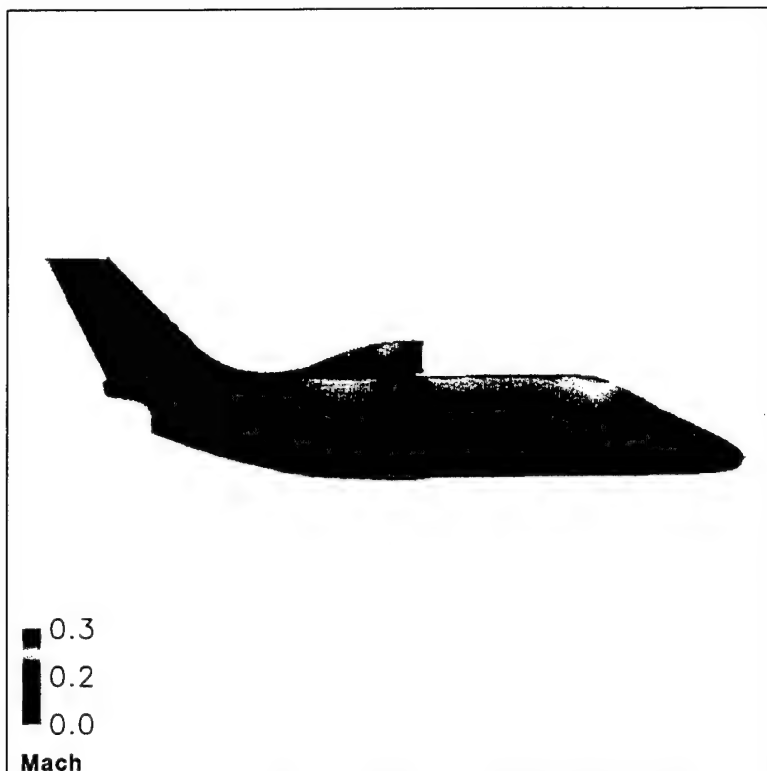


Figure 52 Windward Side, Mach = 0.20, Angle of Attack = 0.0, Beta = 10.0

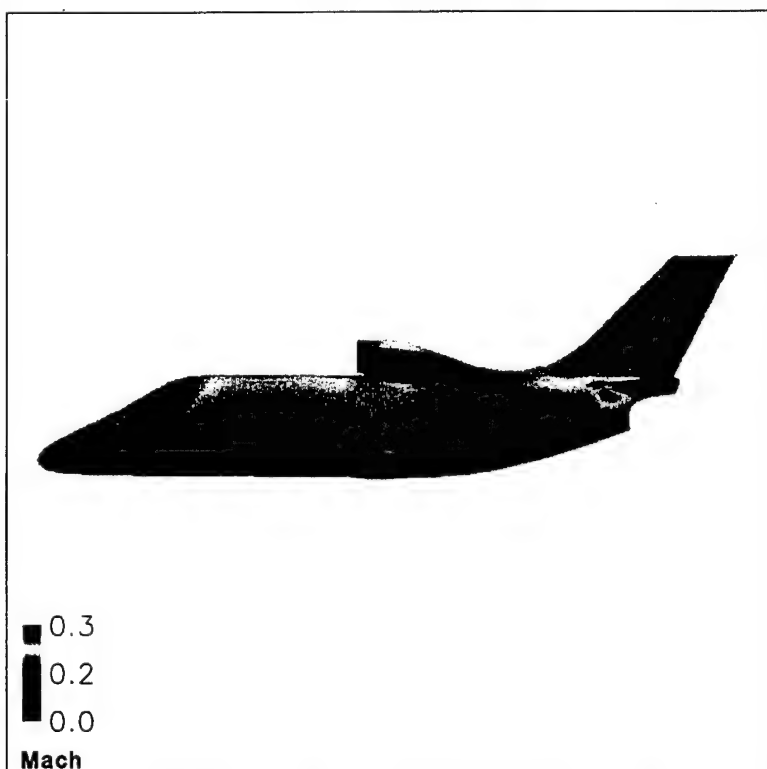


Figure 53 Leeward Side, Mach = 0.20, Angle of Attack = 0.0, Beta = 10.0

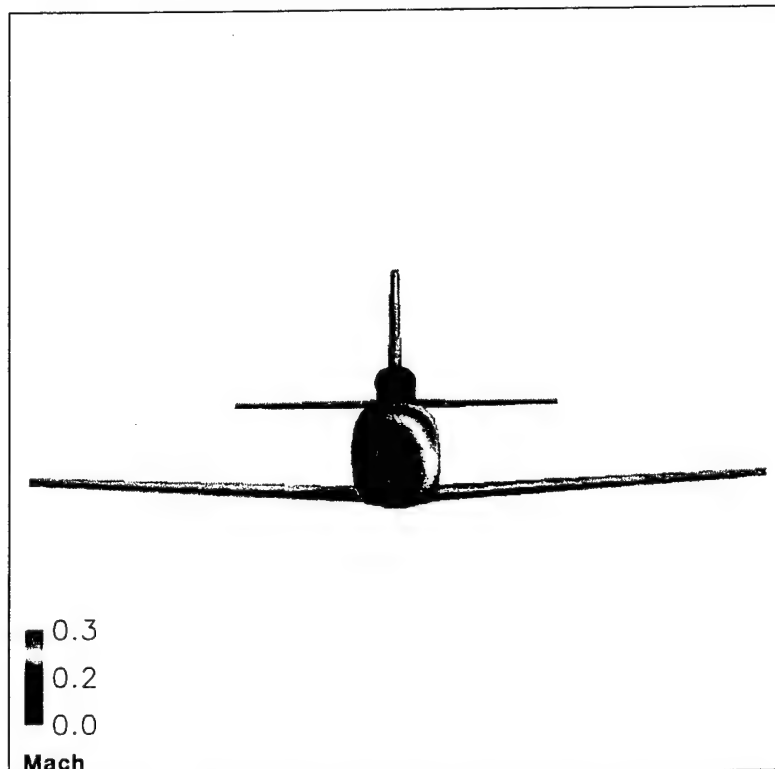


Figure 54 Front View, Mach = 0.20, Angle of Attack = 0.0, Beta = 10.0

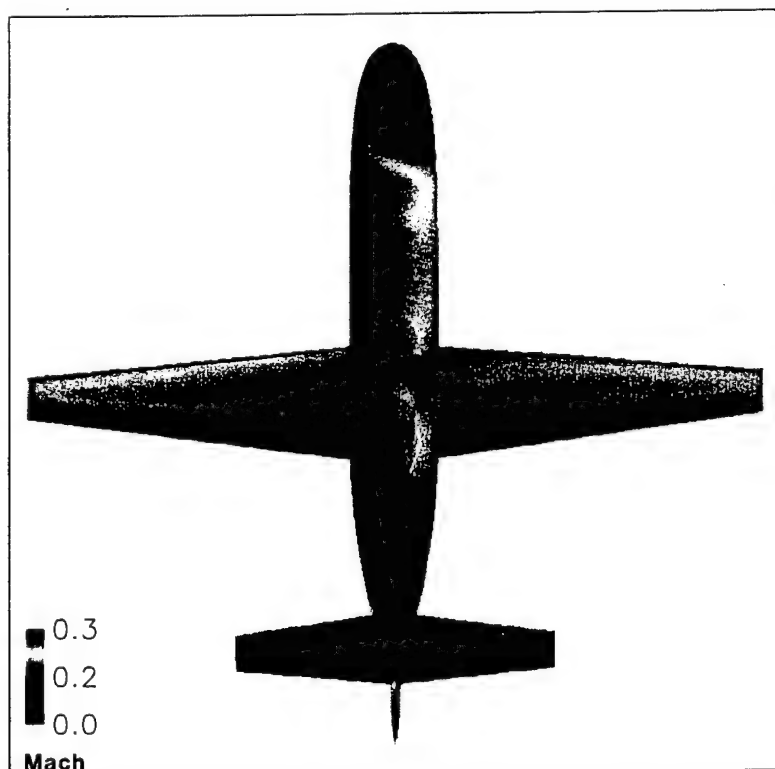


Figure 55 Top View, Mach = 0.20, Angle of Attack = 0.0, Beta = 10.0

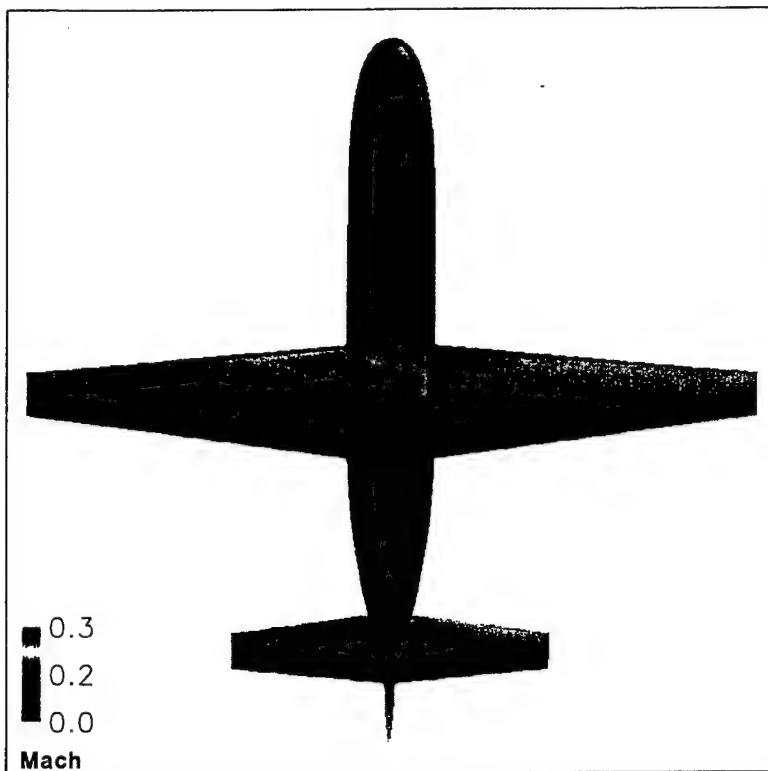


Figure 56 Bottom View, Mach = 0.20, Angle of Attack = 0.0, Beta = 10.0

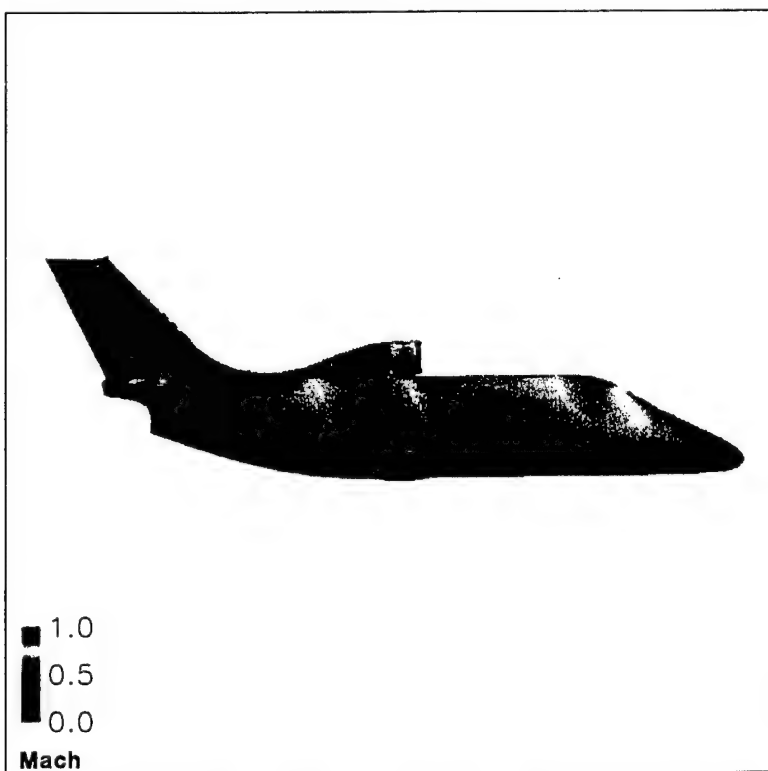


Figure 57 Windward Side, Mach = 0.70, Angle of Attack = 0.0, Beta = 5.0

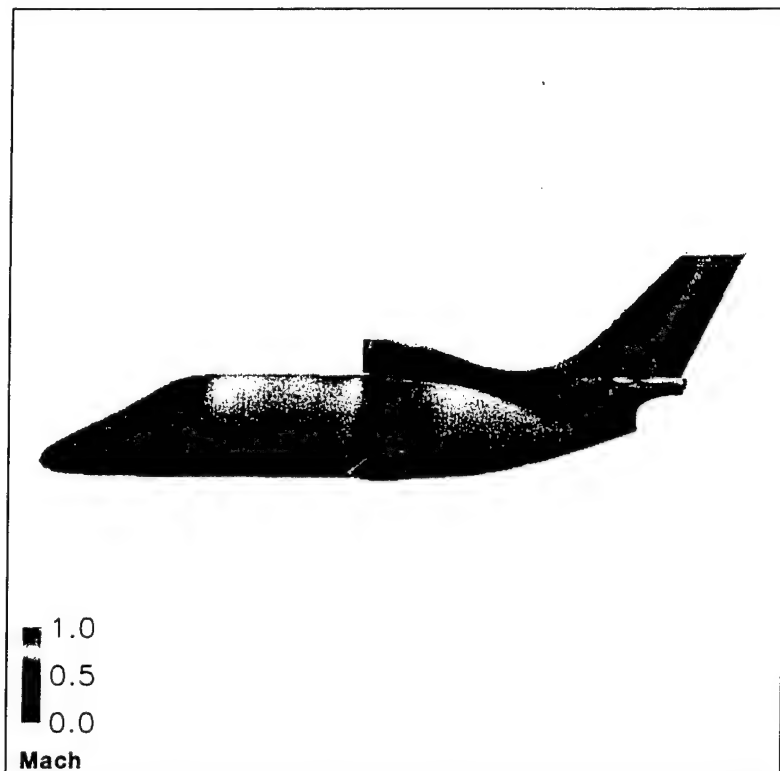


Figure 58 Leeward Side, Mach = 0.70, Angle of Attack = 0.0, Beta = 5.0

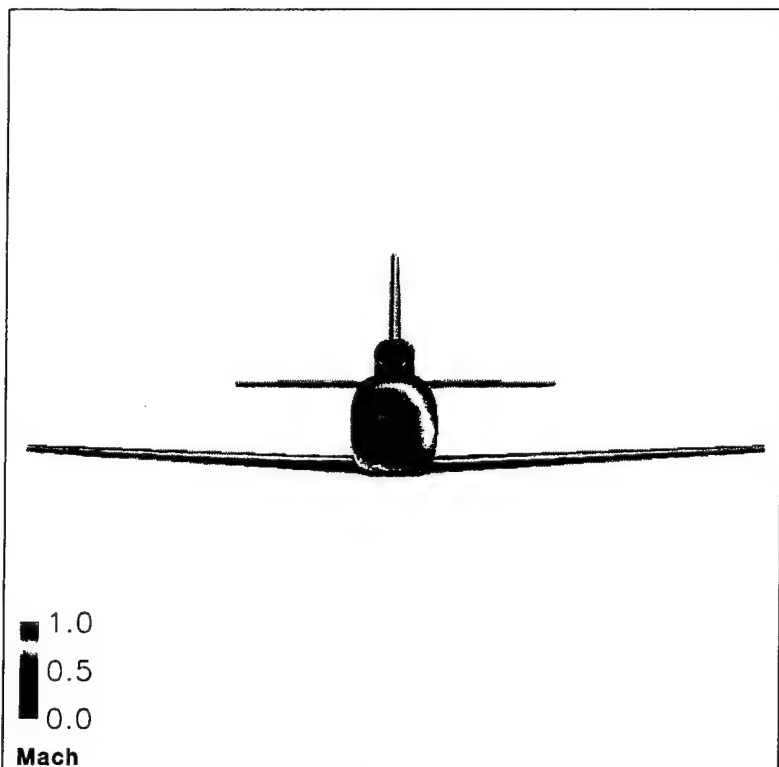


Figure 59 Front View, Mach = 0.70, Angle of Attack = 0.0, Beta = 5.0

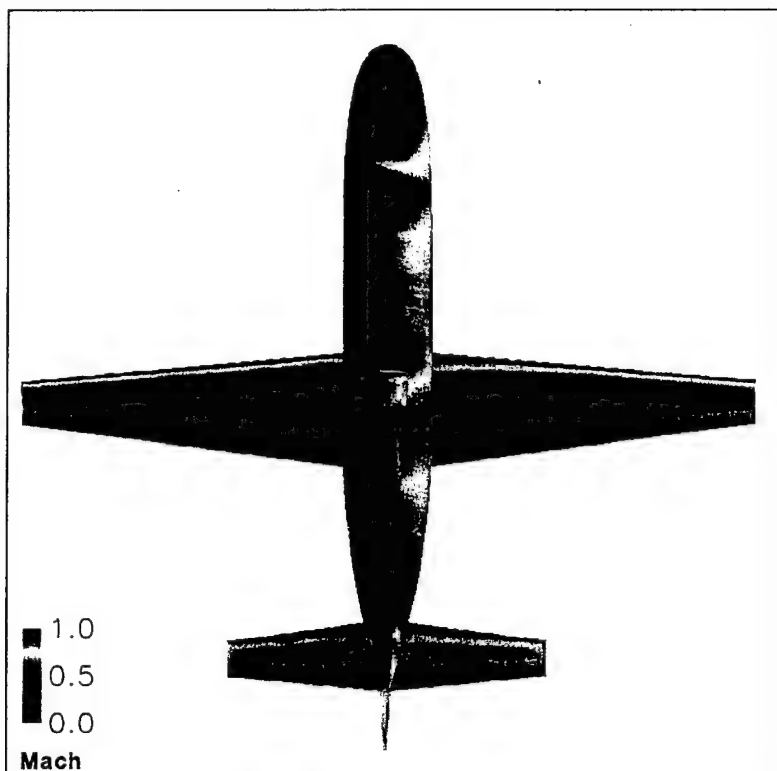


Figure 60 Top View, Mach = 0.70, Angle of Attack = 0.0, Beta = 5.0

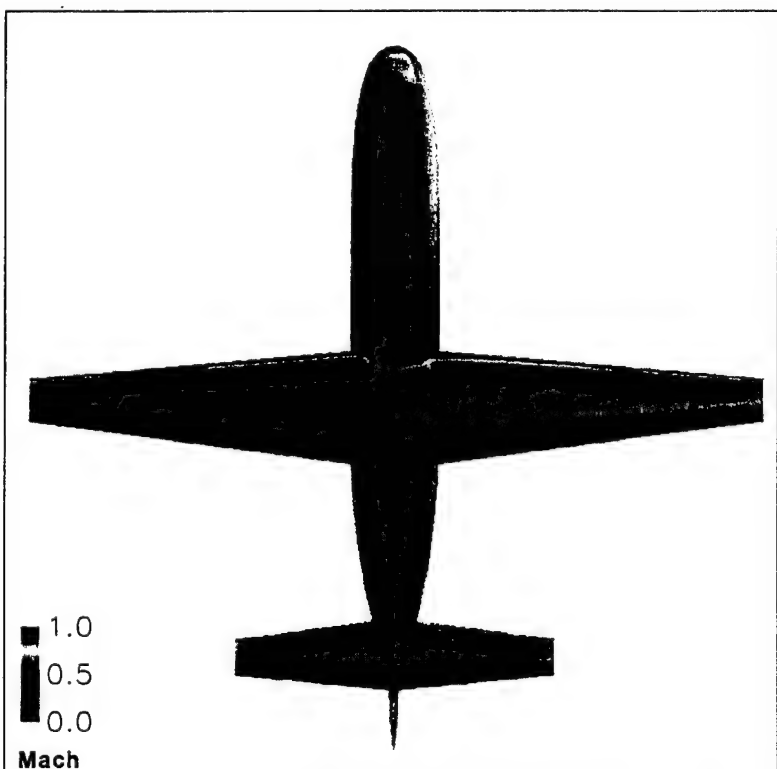


Figure 61 Bottom View, Mach = 0.70, Angle of Attack = 0.0, Beta = 5.0

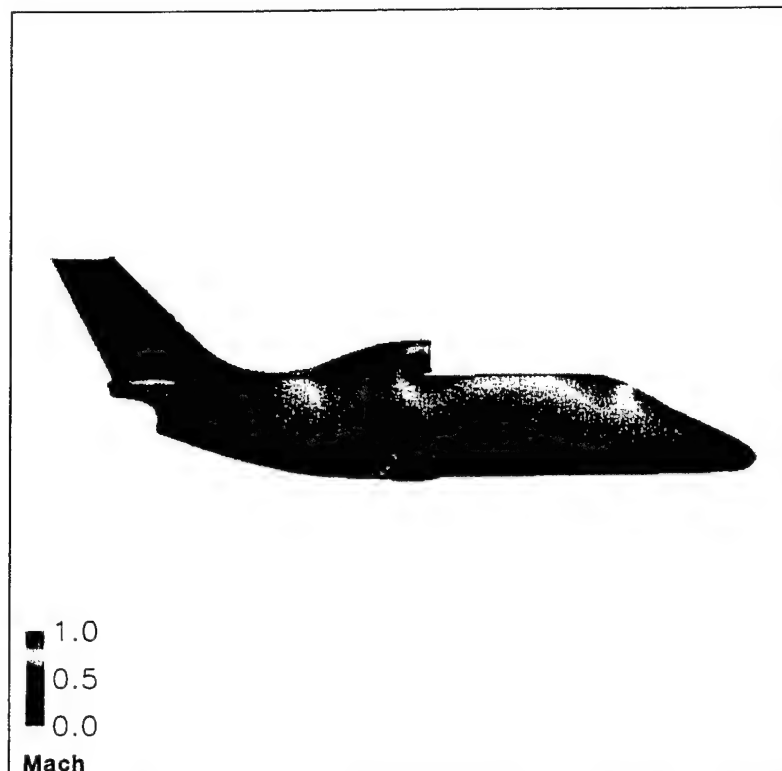


Figure 62 Windward Side, Mach = 0.70, Angle of Attack = 0.0, Beta = 10.0

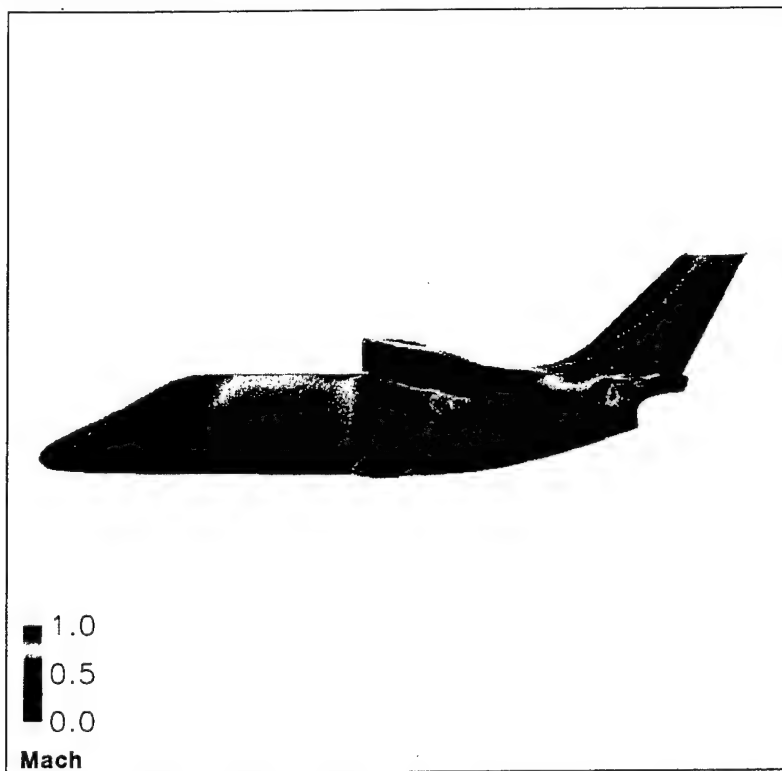


Figure 63 Leeward Side, Mach = 0.70, Angle of Attack = 0.0, Beta = 10.0

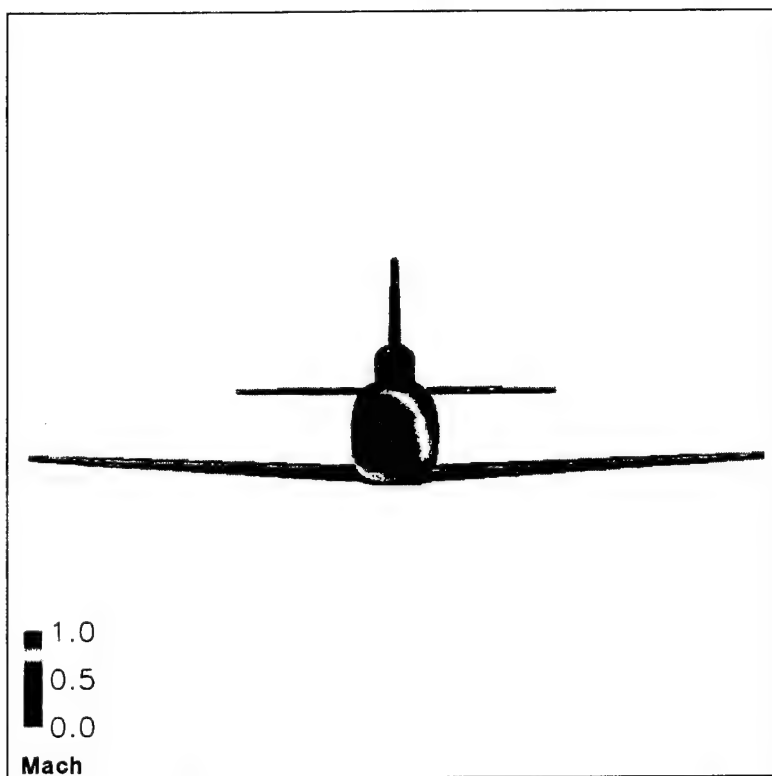


Figure 64 Front View, Mach = 0.70, Angle of Attack = 0.0, Beta = 10.0

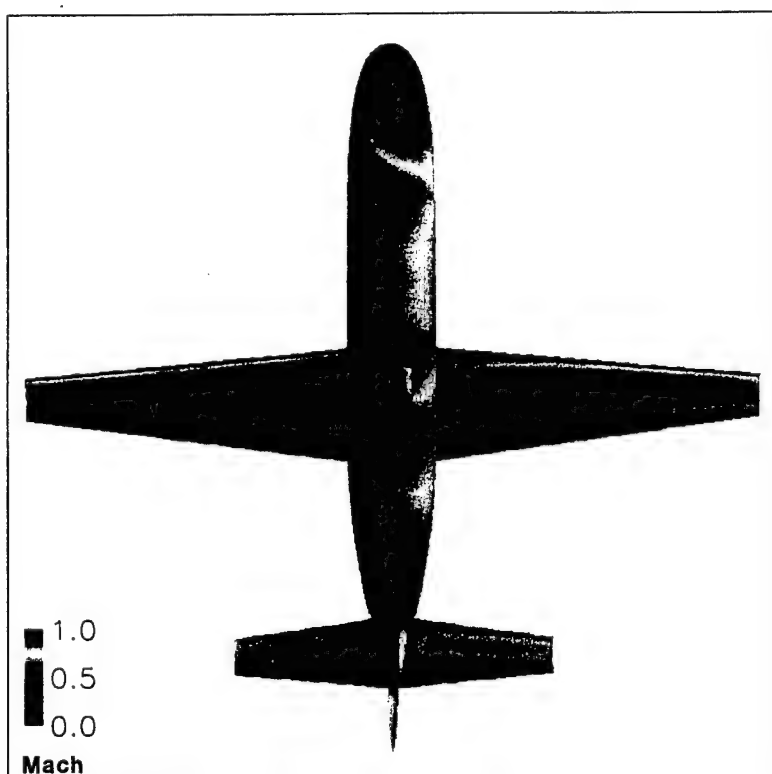


Figure 65 Top View, Mach = 0.70, Angle of Attack = 0.0, Beta = 10.0

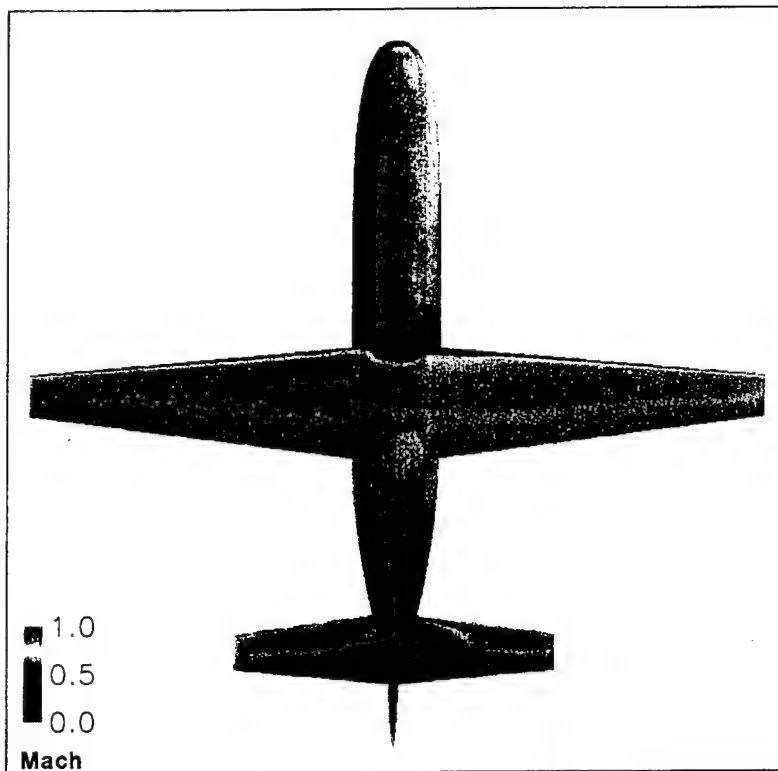


Figure 66 Bottom View, Mach = 0.70, Angle of Attack = 0.0, Beta = 10.0

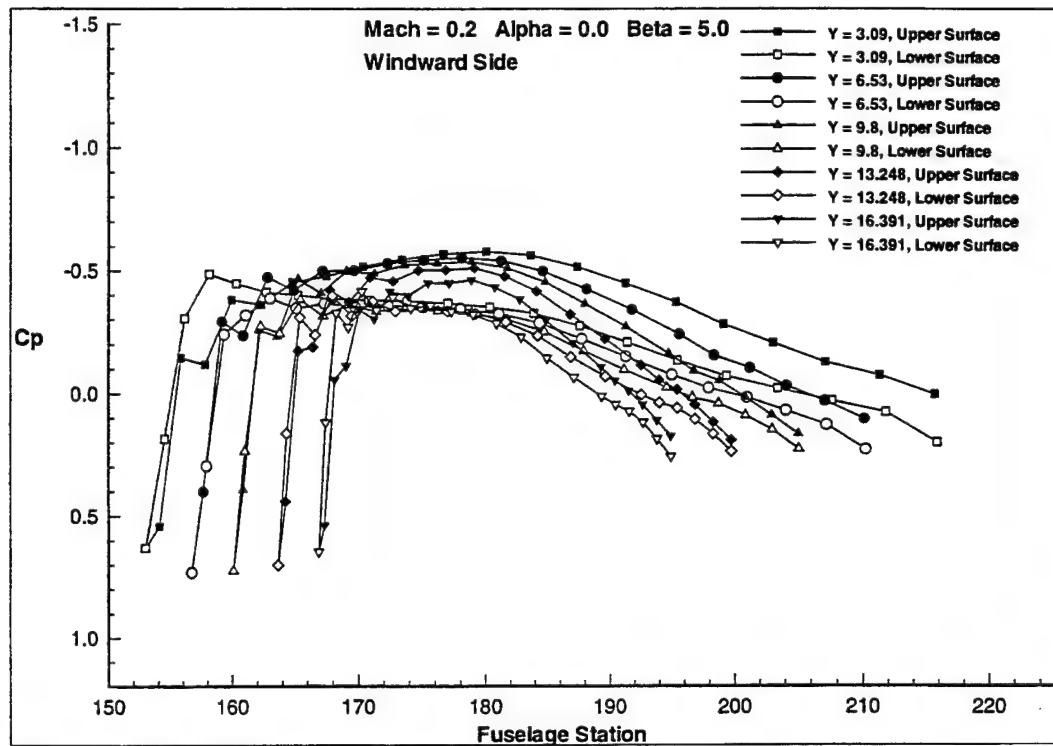


Figure 67 Windward Wing Cp. Mach = 0.20, Angle of Attack = 0.0, Beta = 5.0

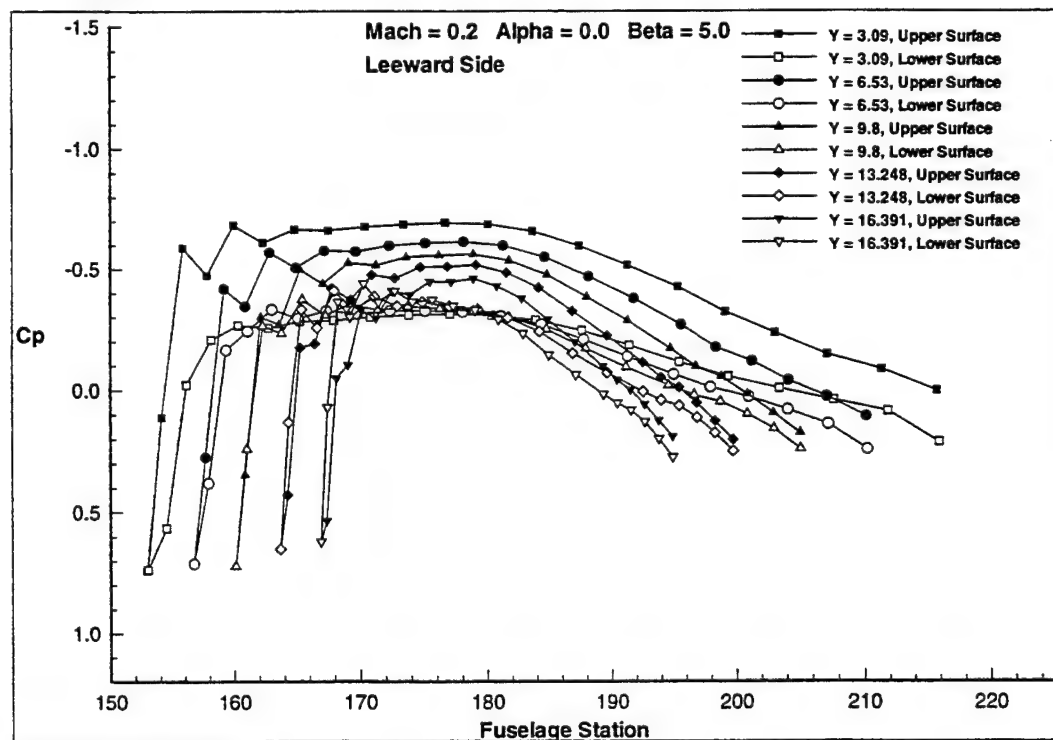


Figure 68 Leeward Wing Cp. Mach = 0.20, Angle of Attack = 0.0, Beta = 5.0

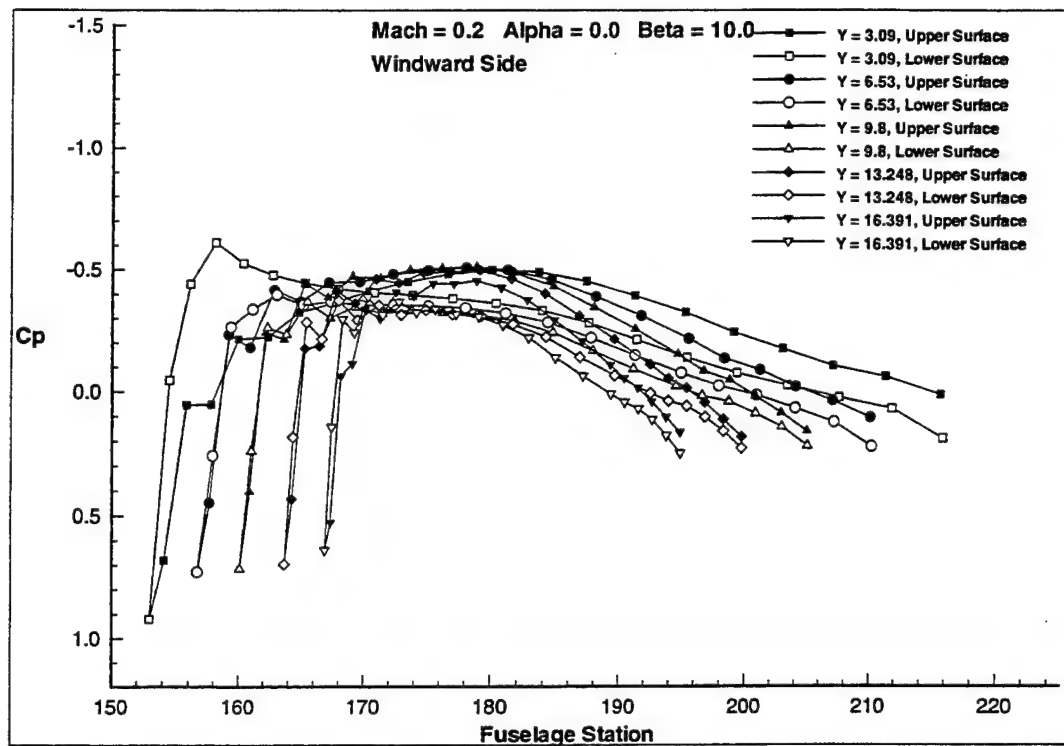


Figure 69 Windward Wing Cp. Mach = 0.20, Angle of Attack = 0.0,
Beta = 10.0

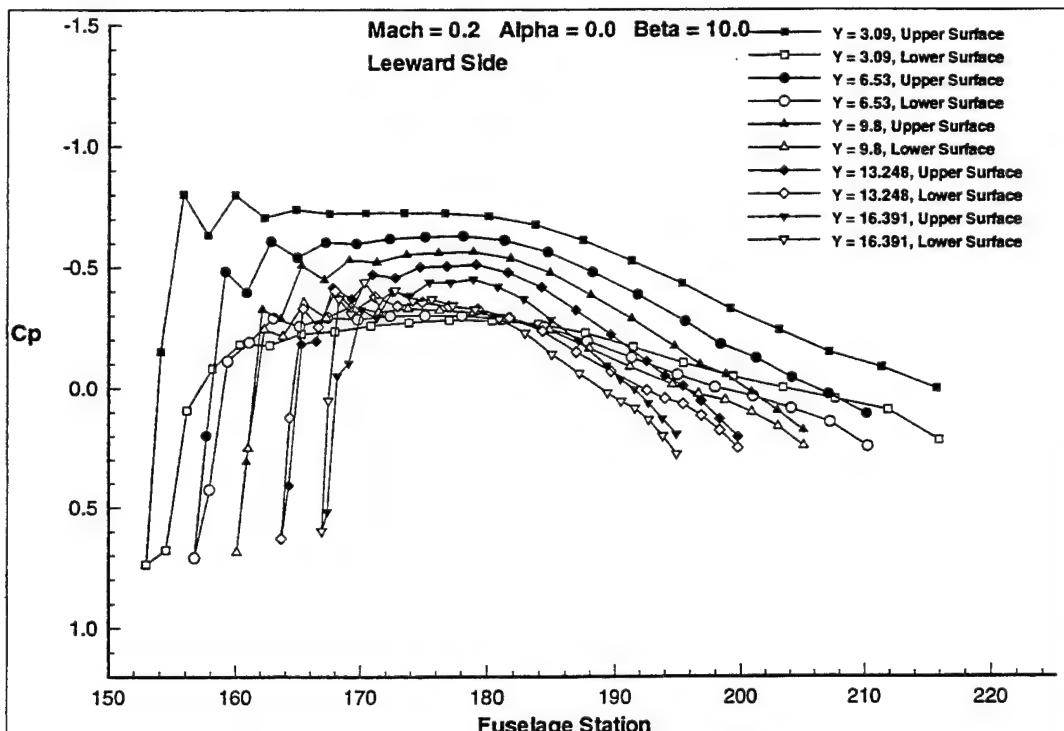


Figure 70 Leeward Wing Cp. Mach = 0.20, Angle of Attack = 0.0,
Beta = 10.0

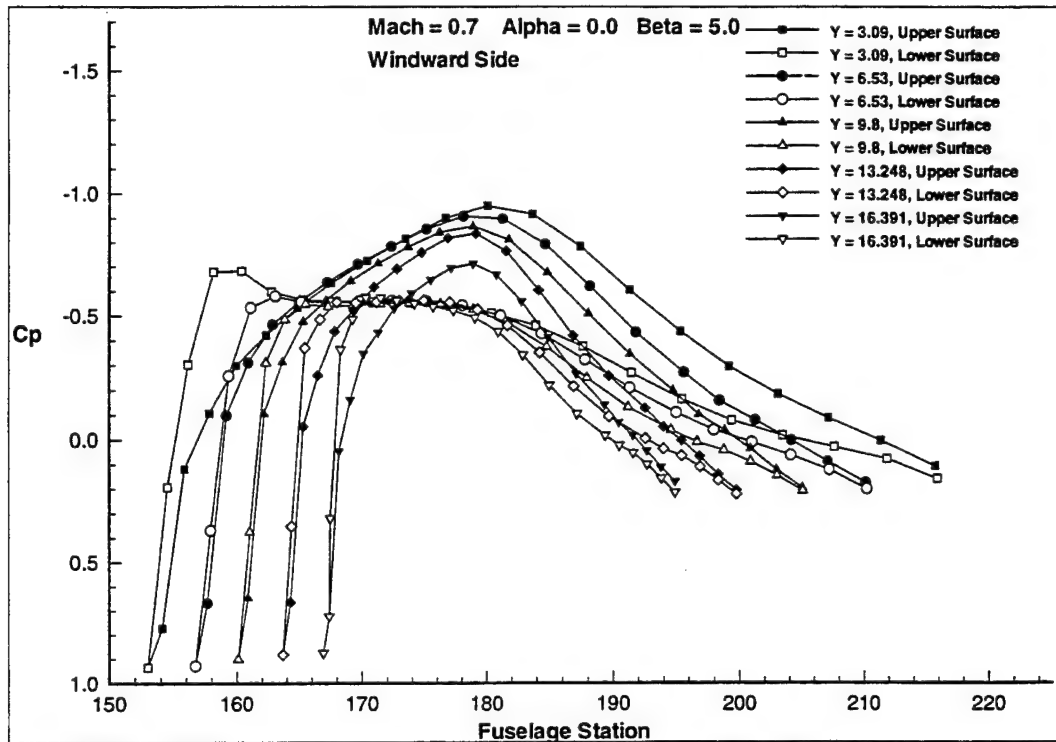


Figure 71 Windward Wing Cp. Mach = 0.70, Angle of Attack = 0.0, Beta = 5.0

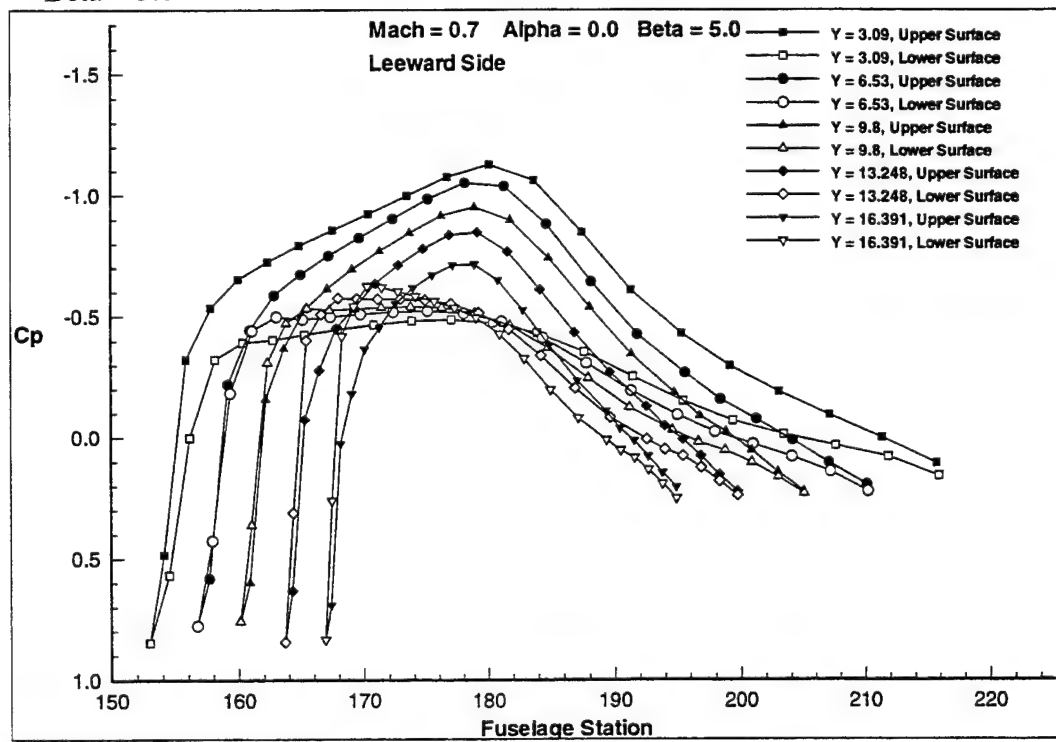


Figure 72 Leeward Wing Cp. Mach = 0.70, Angle of Attack = 0.0, Beta = 5.0

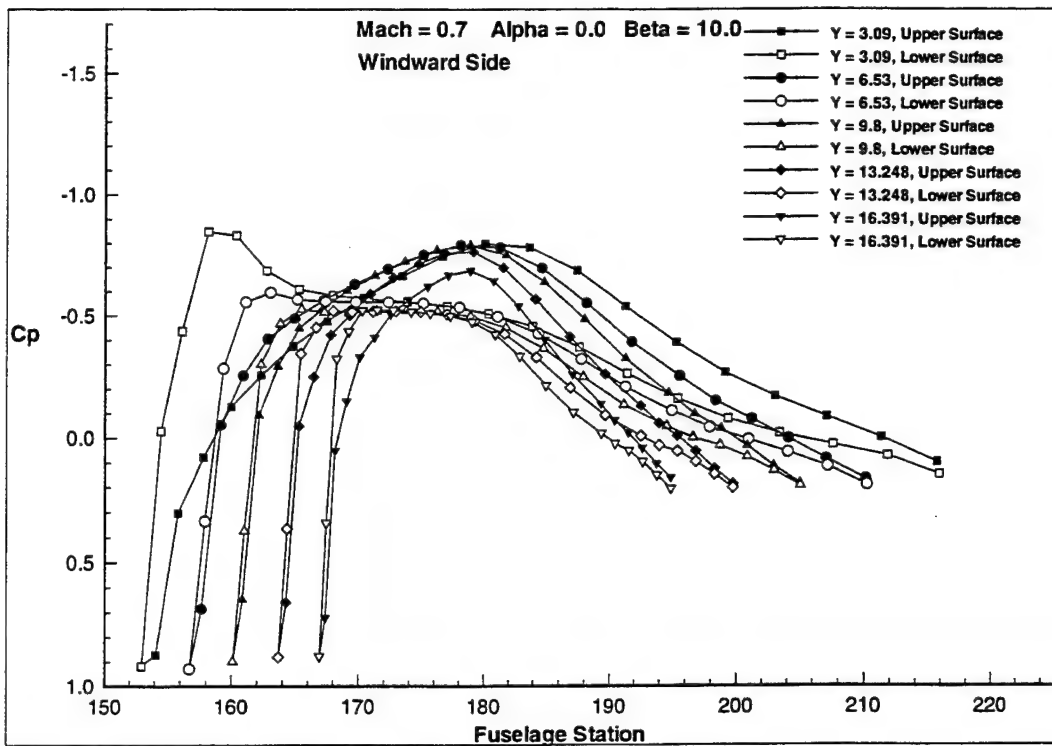


Figure 73 Windward Wing Cp. Mach = 0.70, Angle of Attack = 0.0,
Beta = 10.0

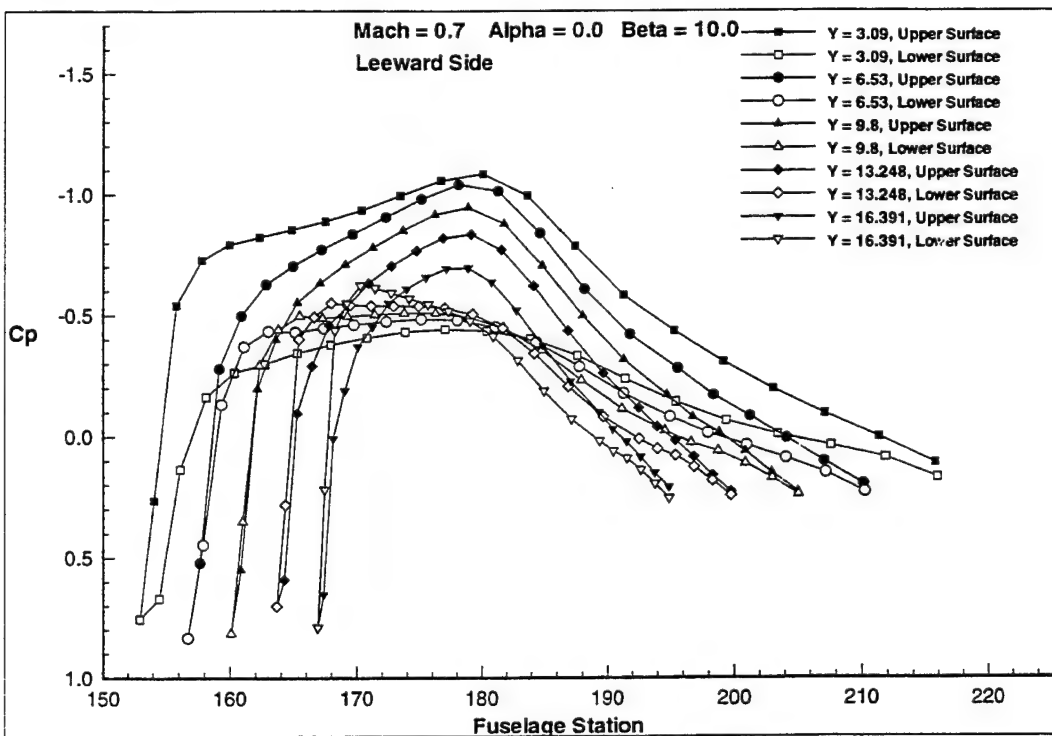


Figure 74 Leeward Wing Cp. Mach = 0.70, Angle of Attack = 0.0,
Beta = 10.0

3 Aileron Effectiveness

3.1 Computational Method - TEAM

To simulate the effect of aileron deflections on the flow field around the aircraft in general, and on the lift, drag, and moments coefficients in particular, serial and parallel versions of TEAM code with a transpiration boundary condition are used. The TEAM code, i.e., Three-dimensional Euler/Navier-Stokes Aerodynamic Method^{2,3}, was originally developed by Lockheed Martin under an Air Force contract. A parallel version of the code (PVMTEAM) was later developed at Georgia Tech Research Institute⁴ using Parallel Virtual Machine (PVM) message passing routines. The TEAM code integrates the three-dimensional Euler/Reynolds-averaged Navier-Stokes equations on boundary conforming grids with single- or multiple-zone grids. For spatial discretization, cell-centered finite-volume with adaptive numerical dissipation is used, while time marching is accomplished using an explicit multi-stage Runge-Kutta stepping scheme. Pseudo-time marching coupled with implicit residual smoothing can be used to accelerate convergence. Various boundary conditions such as, solid, far-field, inlet, exhaust, transpiration, etc., can be specified on the coordinate surfaces, or a section thereof, through an input data set. These boundary conditions facilitate analysis of arbitrarily complex problems. For this analysis the TEAM/PVMTEAM codes, using the 2nd order accurate in space Euler solver, with a five-stage Runge-Kutta stepping scheme, and transpiration boundary conditions are employed to simulate the aileron deflections.

3.2 Computational Grid

The computational grid consisted of 21 blocks and over 1.3 million grid points for half of the Century aircraft. It was developed for Euler analysis, i.e. the solver does not resolve boundary layers or shear layers. For a more complete description of the grid see Section 2.2.

3.3 Boundary Conditions

The far-field boundary condition, which is based on Riemann invariance, is imposed on outer coordinate surfaces of the grid located approximately seven fuselage lengths away from the aircraft, and the solid free-slip boundary condition is specified on all aircraft solid surfaces. The symmetry boundary condition is specified for the aircraft half-plane. Inlet boundary conditions with fixed pressures of $P_{\text{total}}/P_{\text{static}} = 1.0875$ and $P_{\text{total}}/P_{\text{static}} = 1.2745$ are specified for the engine- and scoop-inlet faces, respectively. For the engine-exhaust face, a supersonic exhaust boundary condition with $P_{\text{total}}/P_{\text{static}} = 2.3$, $T_{\text{total}}/T_{\text{static}} = 1.921$, and exit Mach number, $M=1.0$, is specified. It should be noted that although the exhaust is modeled in this computation, the entrainment due to the exhaust plume cannot be fully captured since a Euler analysis is being performed. Aileron deflections are simulated using transpiration boundary conditions wherein the computational grid remains unchanged while the face normals of the deflected surfaces are altered internally by TEAM/PVMTEAM. This causes the flow to see the affected surfaces as though they were deflected. This boundary condition can only be

specified for Euler calculations, and is only valid for small deflection angles where viscous effects can be neglected⁵.

3.4 Computational Approach

To obtain increments in lift, drag, and moment coefficients due to the aileron deflections of ± 5 deg, and ± 10 deg for flight Mach number of 0.7, a baseline converged solution with zero degrees aileron deflection at the above specified flight Mach number is first computed. The runs with deflected ailerons are then performed using TEAM/PVMTEAM's restart option with the baseline solution as the initial conditions. The effect of these deflections is determined by comparing the aerodynamic loads of the simulated deflected ailerons against the baseline values. A combination of serial and parallel runs were performed using TEAM and PVMTEAM, respectively. The serial runs were conducted on a Cray C-90 at the DoD High Performance Computing Center at the Army Corps of Engineers Waterways Experiment Station, and parallel runs were performed on an IBM SP2 at the Maui High Performance Computer Center and an IBM workstation dedicated cluster at the Flight Dynamics Directorate of Wright Laboratory.

3.5 Results and Discussion

We first examine the baseline three-dimensional flow field about the Century aircraft. This is a Euler solution obtained at $M = 0.7$, zero degrees angle of attack ($\alpha = 0$). The convergence of the solution is normally ascertained by monitoring the L2 norm of the density residual and the value of the lift and drag coefficients of the aircraft. However, since an unsteady separation bubble develops under the root of the horizontal tail for this flight condition (Figure 75), normal convergence is not obtained, and therefore, convergence is inferred when the *average* of the lift, drag and moment coefficients reaches a steady value. The surface Mach number contours for this run are shown in Figures 75 and 76. The separation bubble under the horizontal tail can be seen in Figure 75. The flow field over the rest of the aircraft, especially over the wing, appears steady and converged. The lift, drag, and moment coefficients due to the wing alone remained essentially unchanged during the last 4000 iterations, a further indication that the solution is indeed converged. The separation bubble observed in this computation is also noted when the above baseline case is run using the Mercury code (see Section 2), and was also present in the earlier low-Mach number ($M = 0.2$) wind-tunnel testing of a one-sixth scale model.

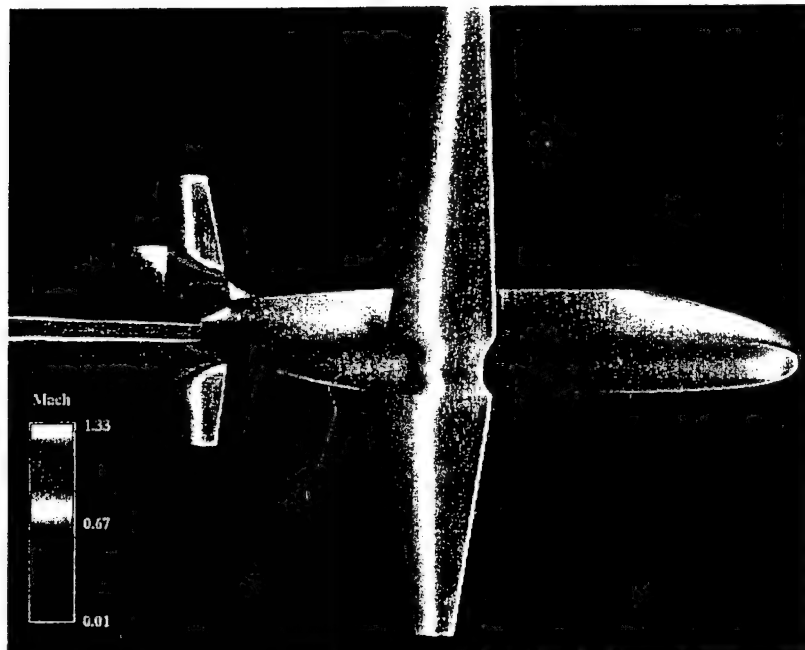
The lift, drag, and pitching moment coefficients are plotted against number of iterations for runs with zero, ± 5 deg., and ± 10 deg. aileron deflections in Figures 76 through 78. The increments in these coefficients attributable to the aileron deflections are illustrated using the solid lines that represent the averages of these coefficients. These averages were obtained by ignoring the first 1000 iterations of each run, during which time the solutions are in a transitory state, then by performing a simple average on the remaining data. These values were then checked against averages obtained on a smaller sample of the same data to assure that the computed averages were stationary. The coefficient increments obtained in this manner were plotted against the experimentally measured data obtained in a wind tunnel at

$M = 0.2$, for zero angle of attack ($\alpha = 0$)¹. Figure 79 presents this data and shows that, although trends for both numerical and experimental data are in agreement, the effects of aileron deflection at Mach 0.7 are more pronounced than the experimental data test condition, i.e., Mach 0.2. This difference may be attributed to compressibility effects, which are negligible at Mach 0.2, but can be significant at Mach 0.7. Some of the difference is almost certainly due to viscous effects. Experience indicates that the inviscid calculations are an "upper bound" and the actual aileron effectiveness will be somewhat less than that predicted by inviscid analysis.

The chordwise variation of the pressure coefficient (C_p) for five sections on the wing and three sections on the horizontal tail are provided for the zero, ± 5 deg, and ± 10 deg aileron deflection runs in Figures 80 through 82. The wing sections are located at approximately, 10 %, 30 %, 50 %, 70 %, and 90 % spans, while the tail sections are at 10 %, 50 %, and 90 % spans. The wing aileron covers the aft section of the wing from approximately 60 % to 100 % span, and therefore, its effect is predominately expected to influence the C_p data for the 70 %, and 90 % wing span locations. Figures 80 and 81 show C_p data at the five-wing sections for the above runs. Figure 80 compares the C_p 's of each section of the wing for the various runs separately, to show the effect of different angles of deflection on the flow. Very little effect is observed at the root of the wing, with increasing influence of the deployed aileron noted for the sections closer to the 60 % span location of the inboard start of the aileron. For the fourth and fifth wing-sections ($Y=13.25$ ft, and $Y=16.39$ ft) which cut across the aileron, large variations of the chordwise C_p data can be seen toward the aft of the wing ($X>15.5$ ft) where the ailerons are present. As would be expected the ± 10 deg deflection runs show more pronounced effects than the ± 5 deg deflection cases. The data of Figure 80 is re-arranged to show the chordwise C_p data of the five wing sections together for each run, and is presented in Figure 81. Again, the effect of aileron deflection on the C_p data can be clearly seen in these figures.

The C_p data for the three tail sections are shown in Figure 82. Figure 82 compares the C_p data of various runs for each tail section. As expected, the C_p data for the lower surface at the root of the tail, i.e., ($Y=1.42$ ft) show the unsteady nature of the separation bubble, while for the upper surface of the tail at this section no effect is observed. The C_p data for the mid section of the tail show some influence of the separation bubble for the ± 10 deg aileron deflection runs. For zero and ± 5 deg aileron deflection runs at the mid-section, and for all cases at the tip section of the tail, no unsteadiness is observed, and the flow is well converged and is almost unaffected by the wing's aileron deflections.

(a)



(b)

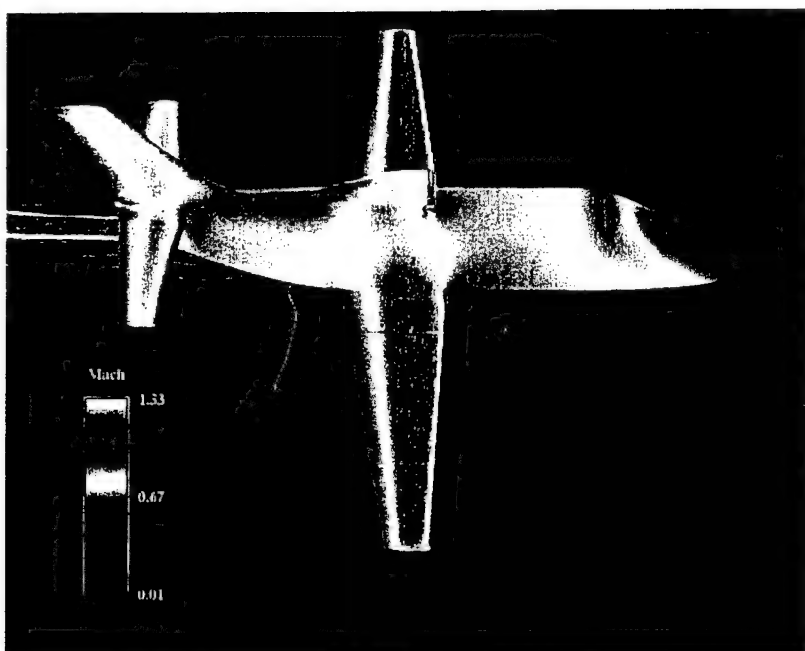


Figure 75 Surface Mach Number Contours, Mach = 0.70,
Angle of Attack = 0.0

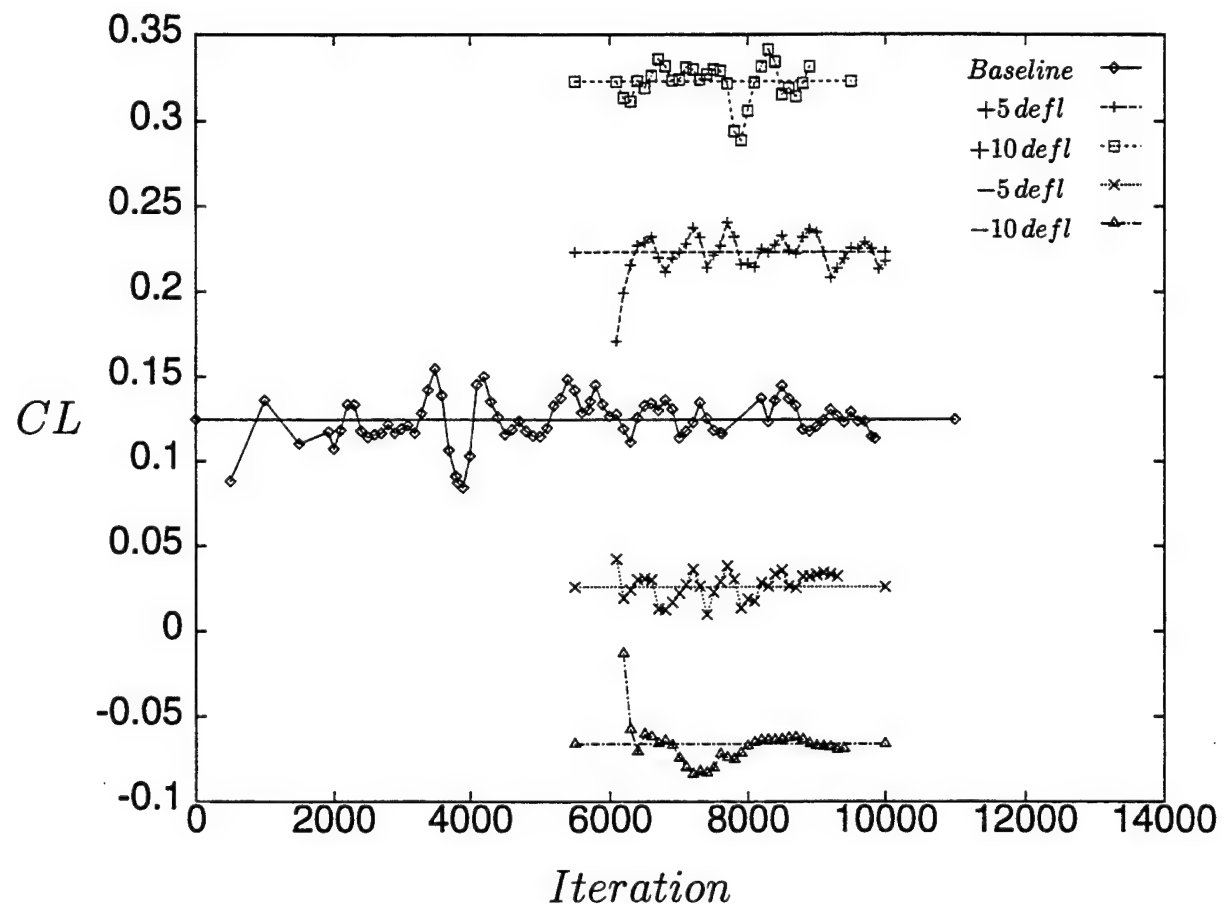


Figure 76 Lift Coefficient Variation with Aileron Deflections, Mach = 0.70,
Angle of Attack = 0.0

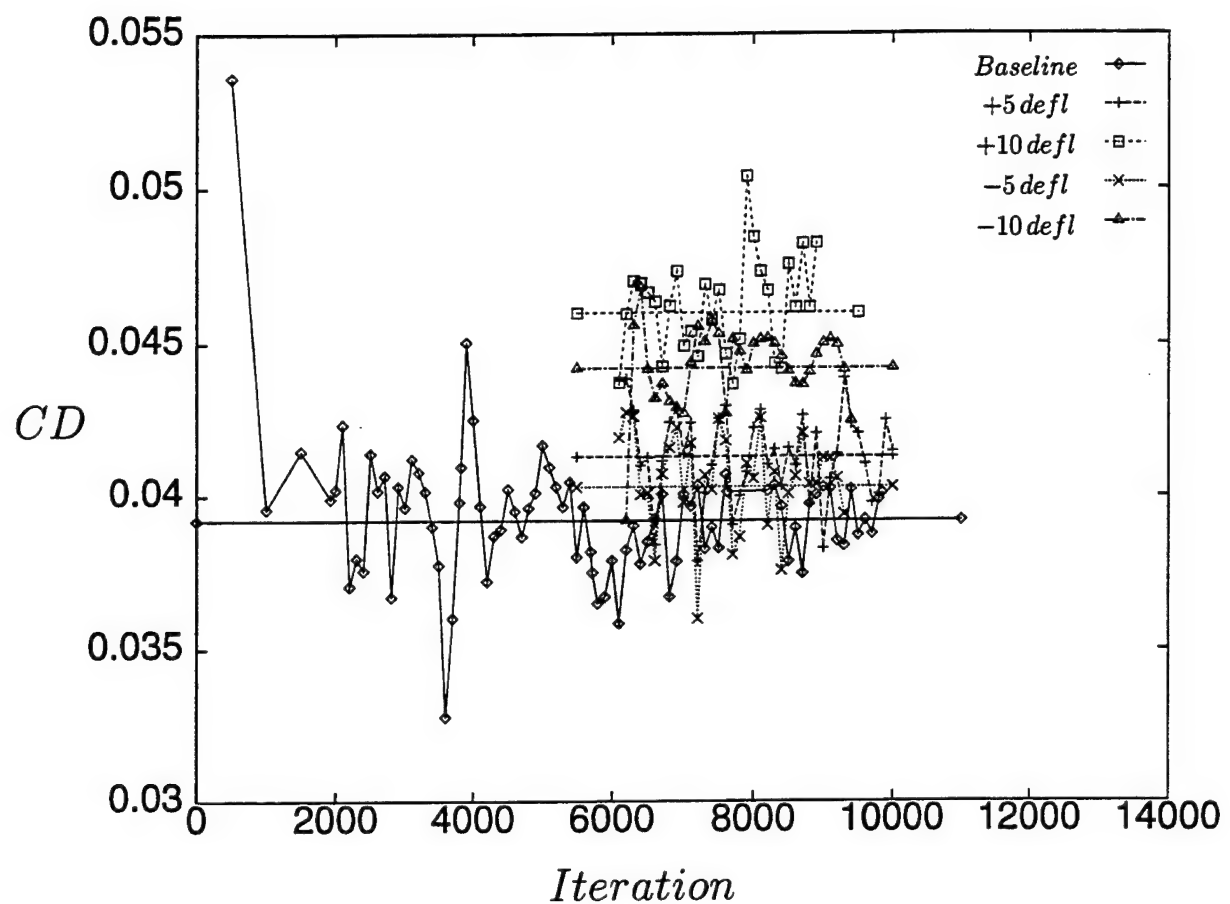


Figure 77 Drag Coefficient Variation with Aileron Deflections, Mach = 0.70,
Angle of Attack = 0.0

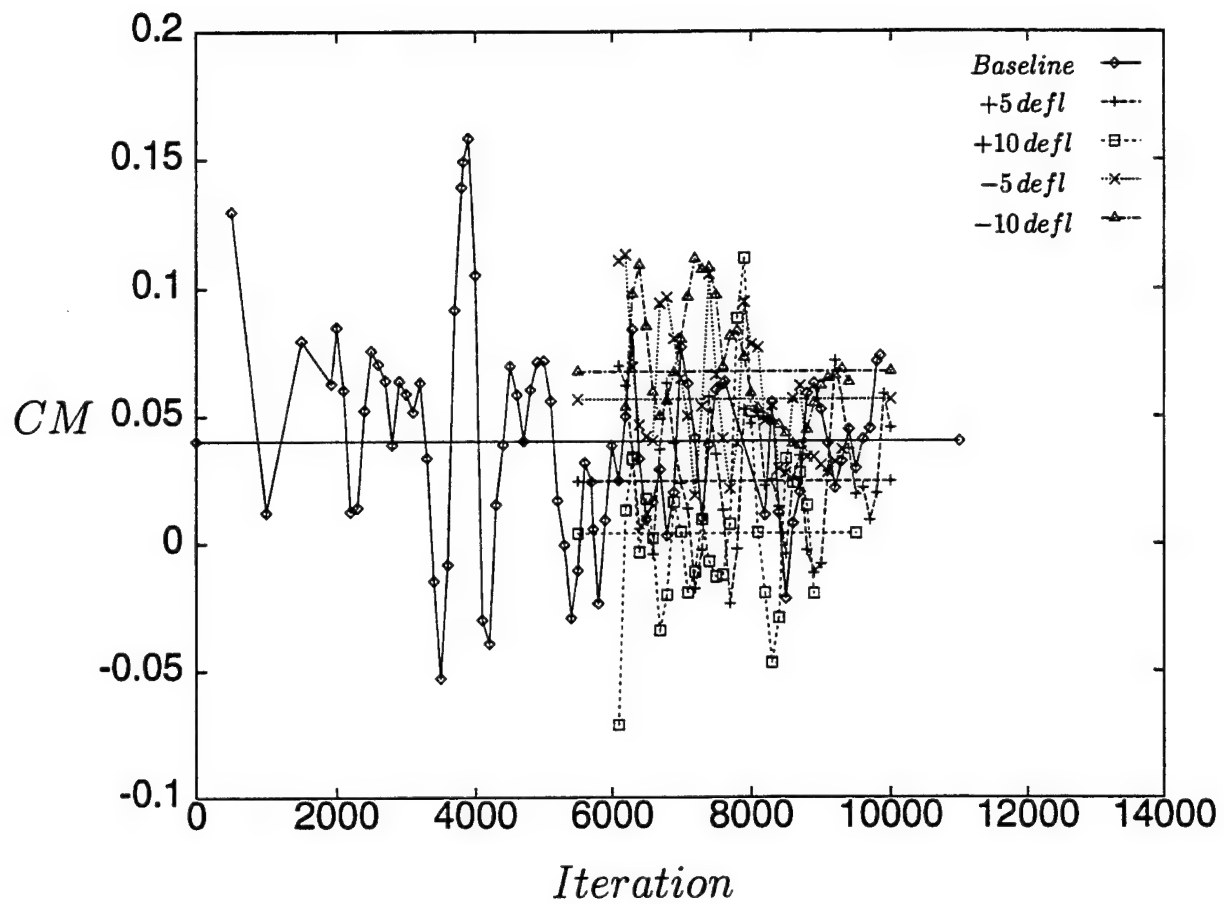


Figure 78 Pitching Moment Coefficient Variation with Aileron Deflections,
 Mach = 0.70, Angle of Attack = 0.0

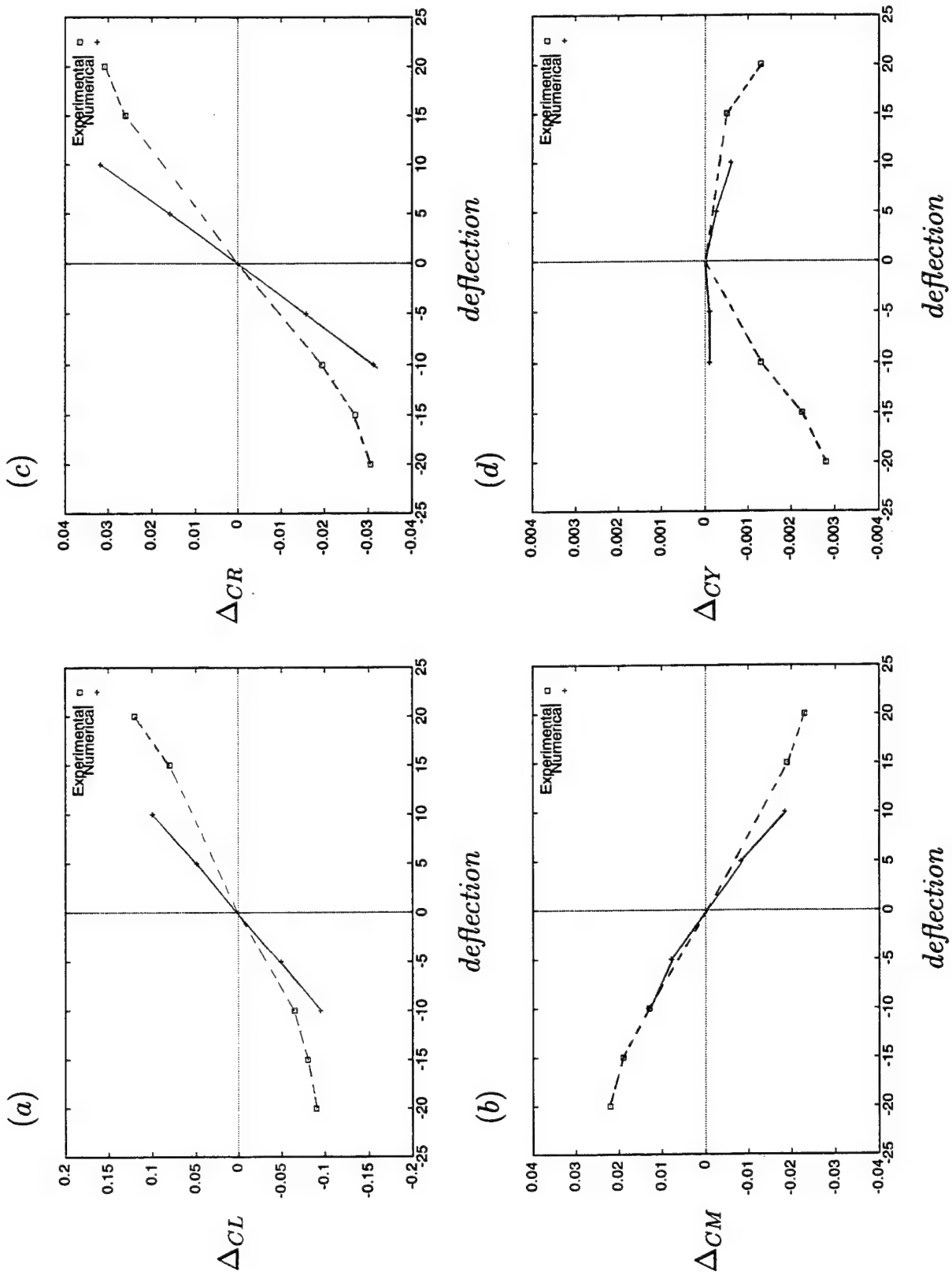


Figure 79 Change in Force Coefficients with Aileron Deflection,
Experimental Mach = 0.2, Numerical Mach = 0.70

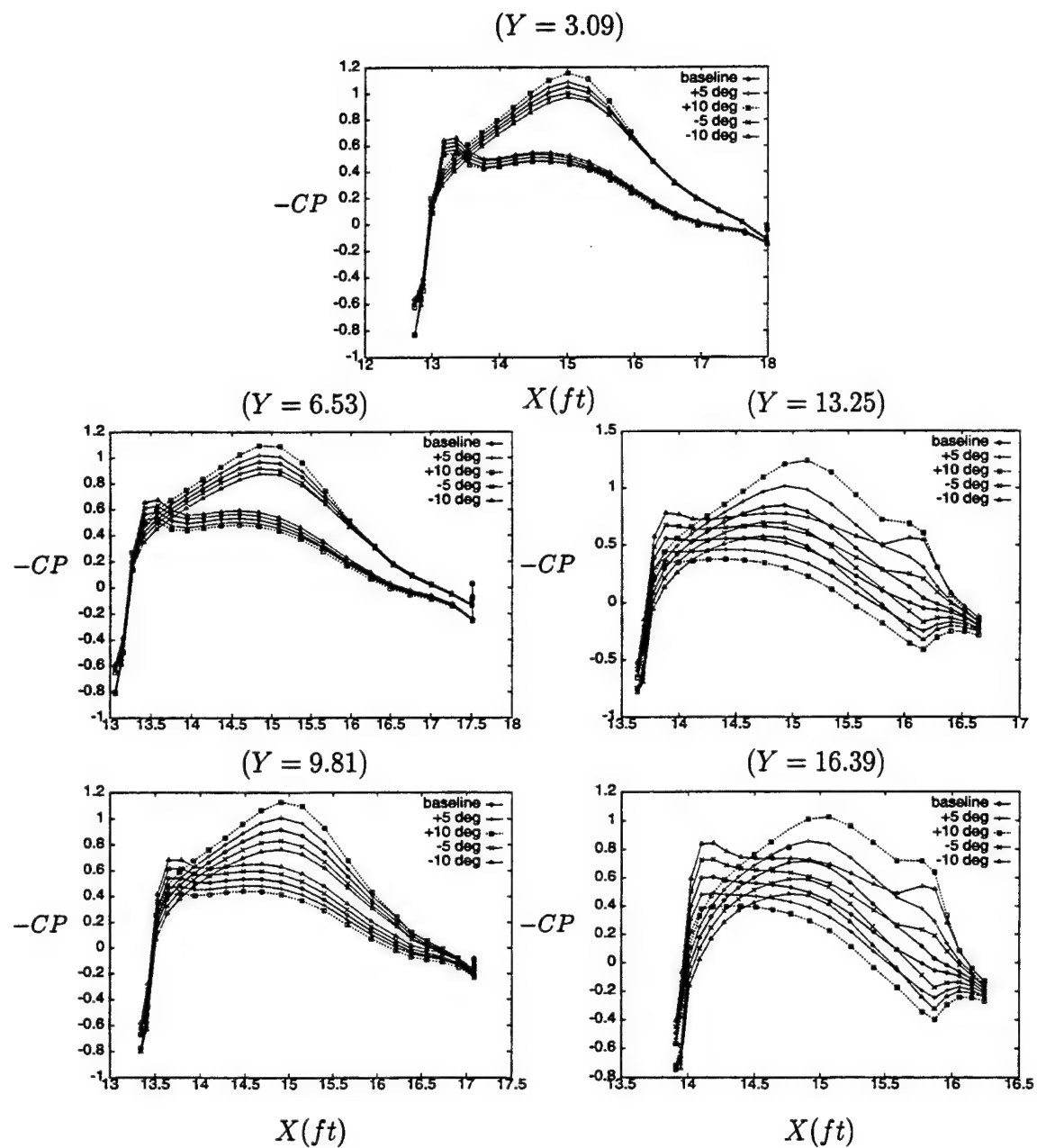


Figure 80 Pressure Coefficients with Aileron Deflections at Given Span Station, Mach = 0.70

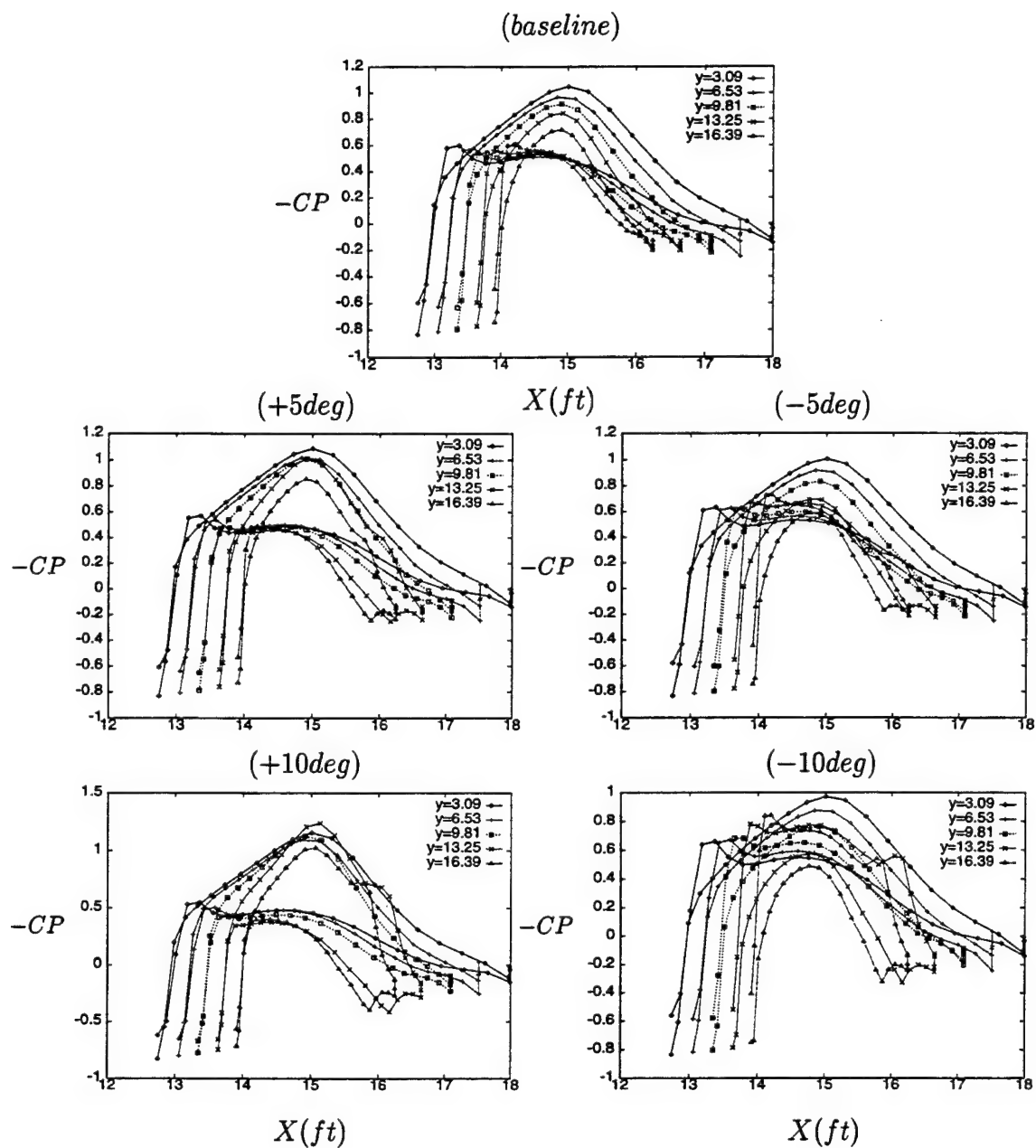


Figure 81 Pressure Coefficients at Different Span Stations for Given Aileron Deflections, $Mach = 0.70$

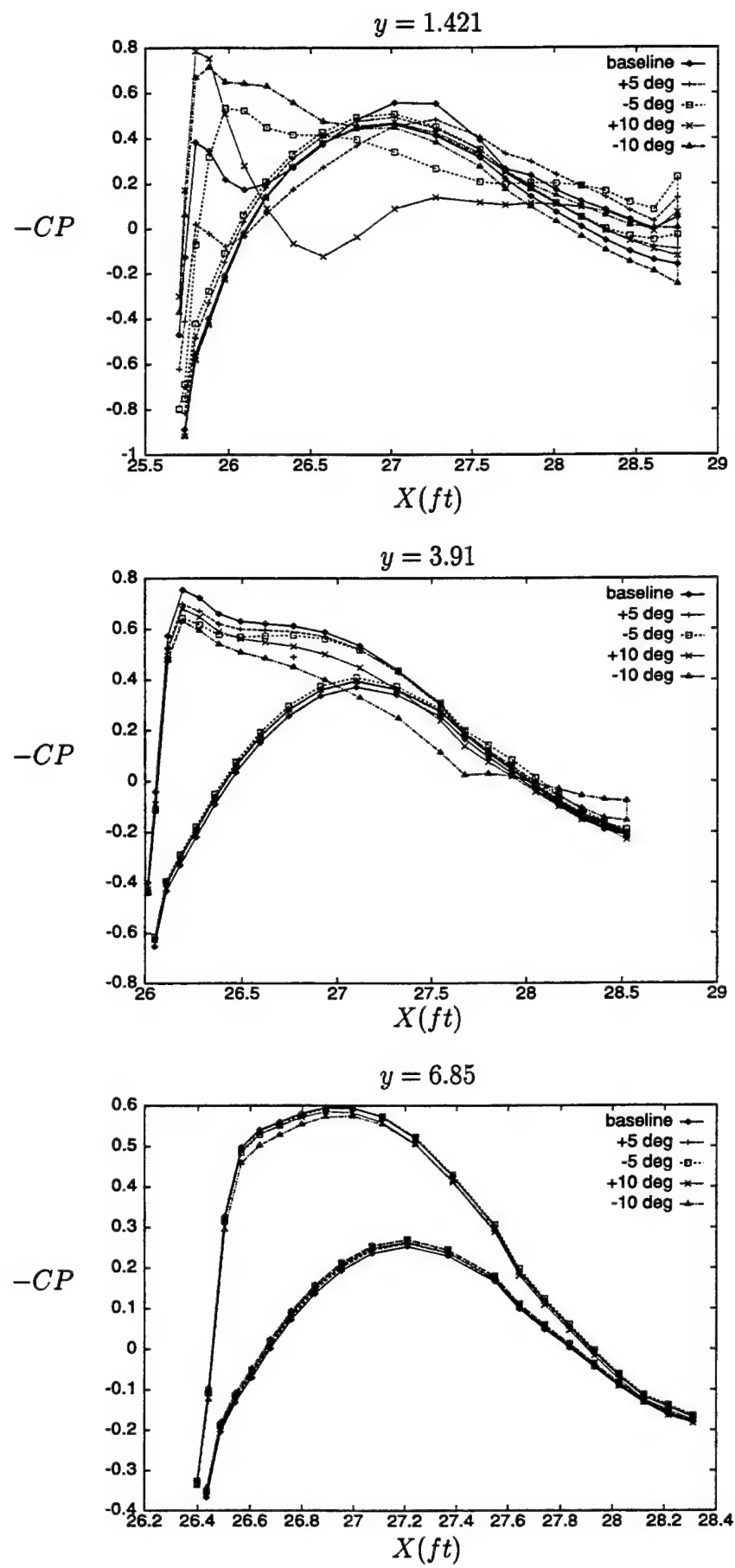


Figure 82 Pressure Coefficients on Tail due to Wing Aileron Deflections

4 Drag Divergence Analysis

Figure 83 compares wave drag estimates from the 3-D CFD analysis with a 2-D airfoil test in the OSU tunnel⁶. It appears that drag divergence occurs at a slightly lower Mach number on the 3-D Century Jet than the 2-D airfoil. There are several things that should be considered when trying to make this comparison such as viscous effects, wind tunnel wall effects and differences in airfoil sections. The 2-D airfoil was a "SZ(1)-0215" section, whereas the Century Jet wing has a "MS(1)-0313" airfoil. Plus, there is the added difference of 1 degree angle of attack. The CFD analyses were done at +1 degree angle of attack, whereas, the 2-D test was at 0 degree angle of attack. One must remember that the 3-D wing has a variable geometric incidence along the span as a result of the twist built into the wing.

The table below provides the actual values from the CFD analysis. The wave drag increments were determined by subtracting the drag value at Mach = 0.70 from the drag values at the other Mach numbers. There were several repeat runs at Mach = 0.70 in the 2-D test, therefore, an average drag for all the repeat runs was computed and subtracted from the 2-D test results to obtain the wave drag increments plotted in Figure 83. The CFD analysis of the Century Jet configuration indicated only about 20 counts (0.0020) of drag difference between Mach = 0.20 and Mach = 0.70, but 105 counts difference between Mach = 0.70 and Mach = 0.75. Thus drag divergence appears abruptly, with a relatively large increase in drag, at speeds above Mach = 0.70. This is not unreasonable or unexpected for a straight, relatively thick, high-aspect ratio wing.

Table 2

Century Jet Wave Drag Estimates	
AOA = 1.0 degree	
Mach No.	ΔCD
0.2	-0.0019
0.7	0
0.75	0.0105
0.8	0.0178

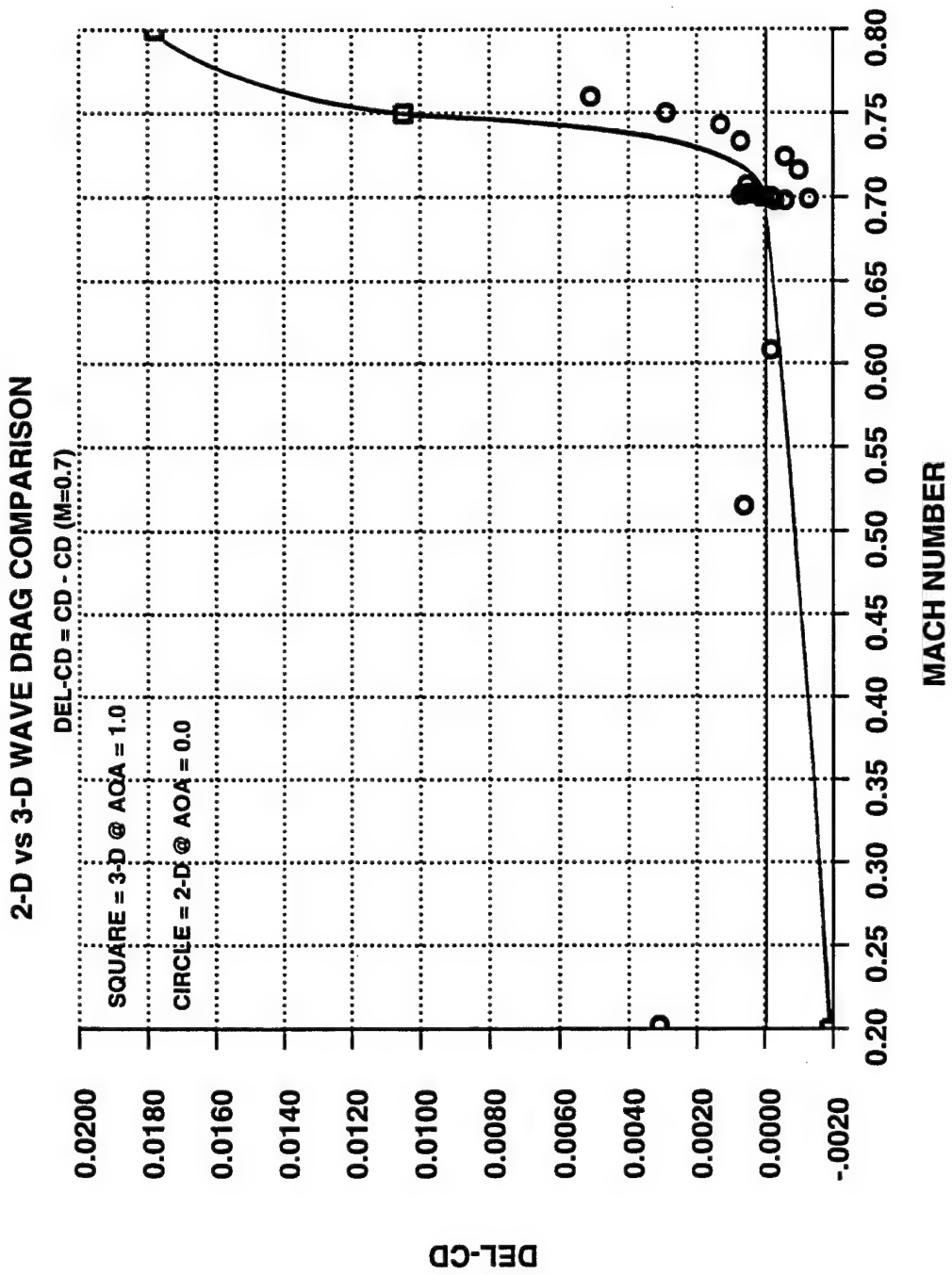


Figure 83 Drag Divergence

5 Elevator Effectiveness

Elevator effectiveness was simulated using the transpiration boundary condition procedure described in Reference 5. The calculations are for the $Mach = 0.7$, $AOA = 0.0$ flight condition. The +5 and -5 elevator deflection runs start with the converged clean aircraft configuration, and the +10 and -10 runs start with the +5 and -5 solutions respectively.

The separated region on the inboard lower surface of the tail produces significant "noise" in the solution that prevents the level of convergence preferred. Negative elevator settings appear to aggravate the unsteadiness while positive elevator settings seem to reduce the unsteadiness. However, it is obvious from the curves in Figures 87 and 89 that very definite increments in lift and pitching moment are realized with each elevator deflection. Drag increments (Figure 88) are less certain because the "noise" is equal to, or greater than, the increments due to elevator deflection.

The process used to arrive at the increments in the force coefficients was to compute a simple average of the values over several iterations. This should be analogous to what is done in a wind tunnel where several samples from the model balance are averaged to provide the final load values.

The following table provides the increments in total aircraft lift, drag and pitching moment coefficient due to elevator deflections. This same information is also plotted in Figures 84-86 where the increments from the OSU low speed wind tunnel test have been added for comparison. Since the CFD is an inviscid analysis and the deflections are simulated using transpiration boundary conditions, the CFD data represents a "best case" for tail effectiveness. The actual tail effectiveness will almost certainly be somewhat less than indicated by the CFD analysis. The larger the simulated deflection, the larger the potential error.

Table 3

Elevator Effectiveness			
Total Aircraft Increments			
Mach = 0.70, AOA = 0.0			
Elevator	ΔCL	ΔCD	ΔCM
0	0	0	0
5	0.0765	-0.0008	-0.2174
10	0.1673	0.0033	-0.4727
-5	-0.0658	0.0046	0.1881
-10	-0.1277	0.0109	0.3624

Chordwise pressure coefficients at three locations on the horizontal tail are provided in Figures 90-92. The more inboard location (butline = 1.6 ft.) shows the effects of the

separated flow on the lower surface. It also provides a clue as to why the flow may be prone to separate from the lower surface. The Euler analysis predicts a very sharp negative pressure coefficient spike on the lower surface near the leading edge. This would almost certainly promote boundary layer transition and could be severe enough to cause flow separation. A fairly large negative pressure spike still occurs near the lower surface leading edge at mid-span (butline = 4.1 ft.), but there is no indication of separation. The pressures are very well behaved at the most outboard location (butline = 6.9 ft.). At this location the pressures also provide some hope for laminar flow up to about 45% chord on the upper surface, and perhaps to 30% chord on the lower surface. Positive elevator deflections appear to promote more laminar flow, whereas negative elevator deflection appear to encourage earlier transition.

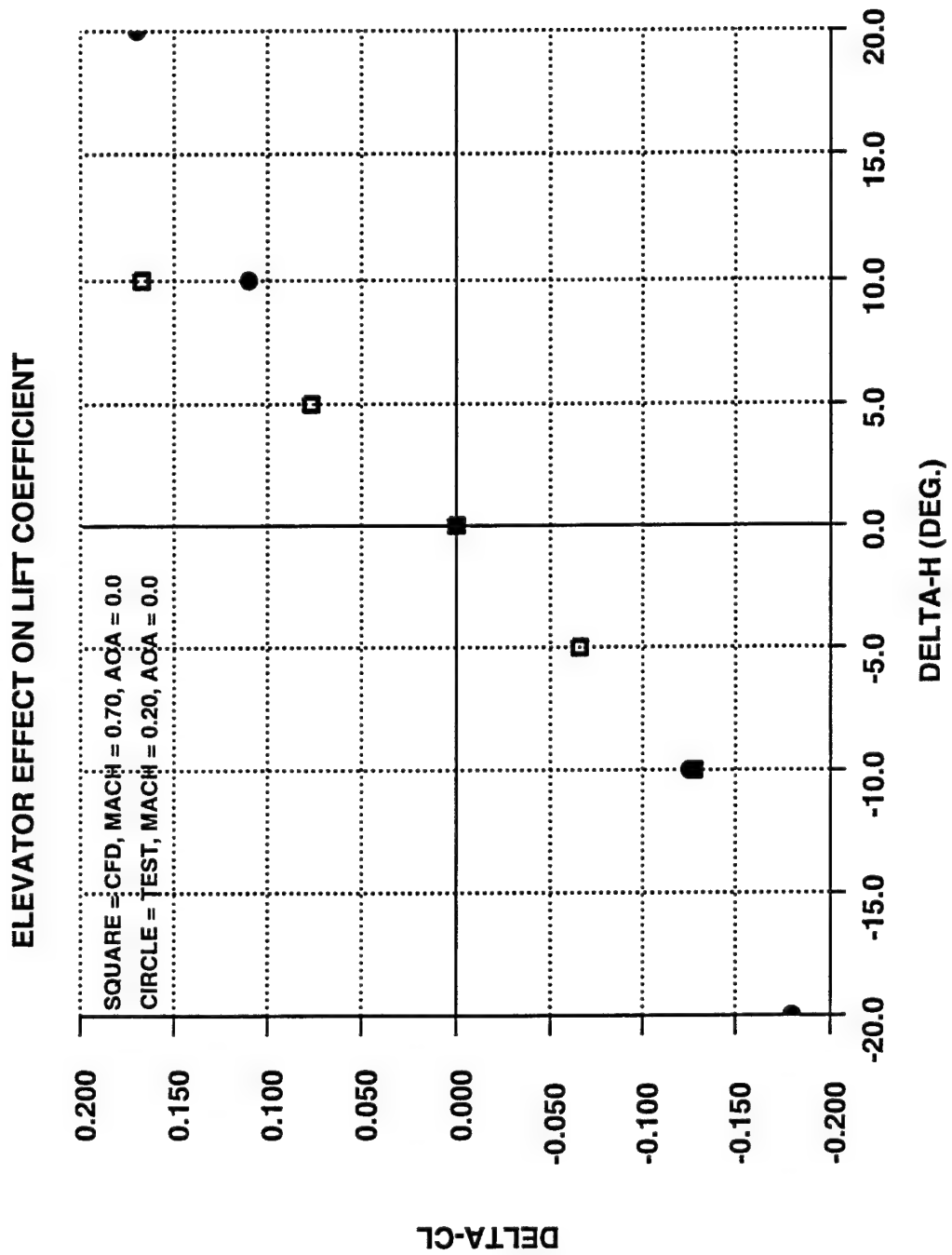


Figure 84 Effect of Elevator Deflection on Lift Coefficient

ELEVATOR EFFECT ON DRAG COEFFICIENT

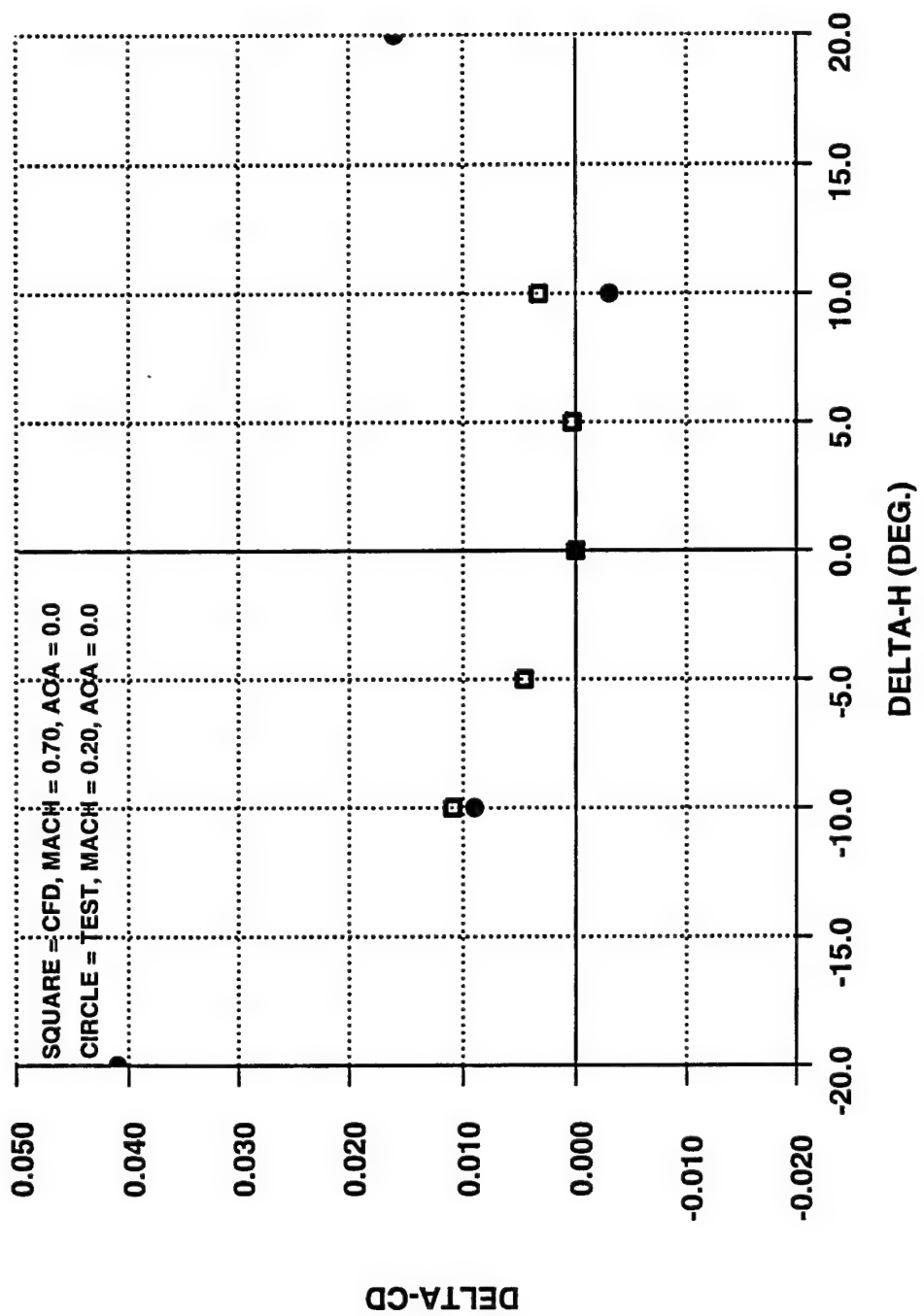


Figure 85 Effect of Elevator Deflection on Drag Coefficient

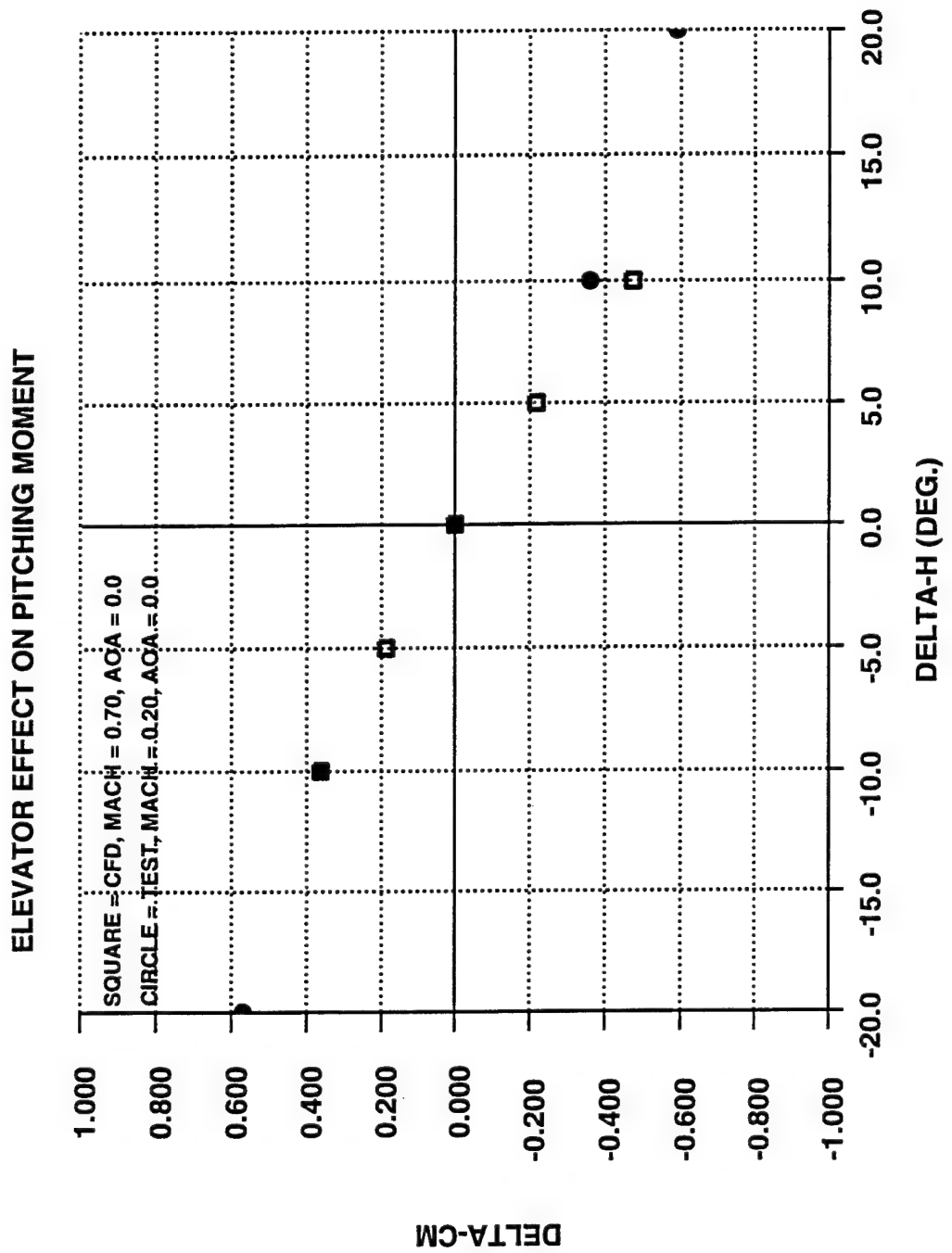


Figure 86 Effect of Elevator Deflection on Pitching Moment Coefficient

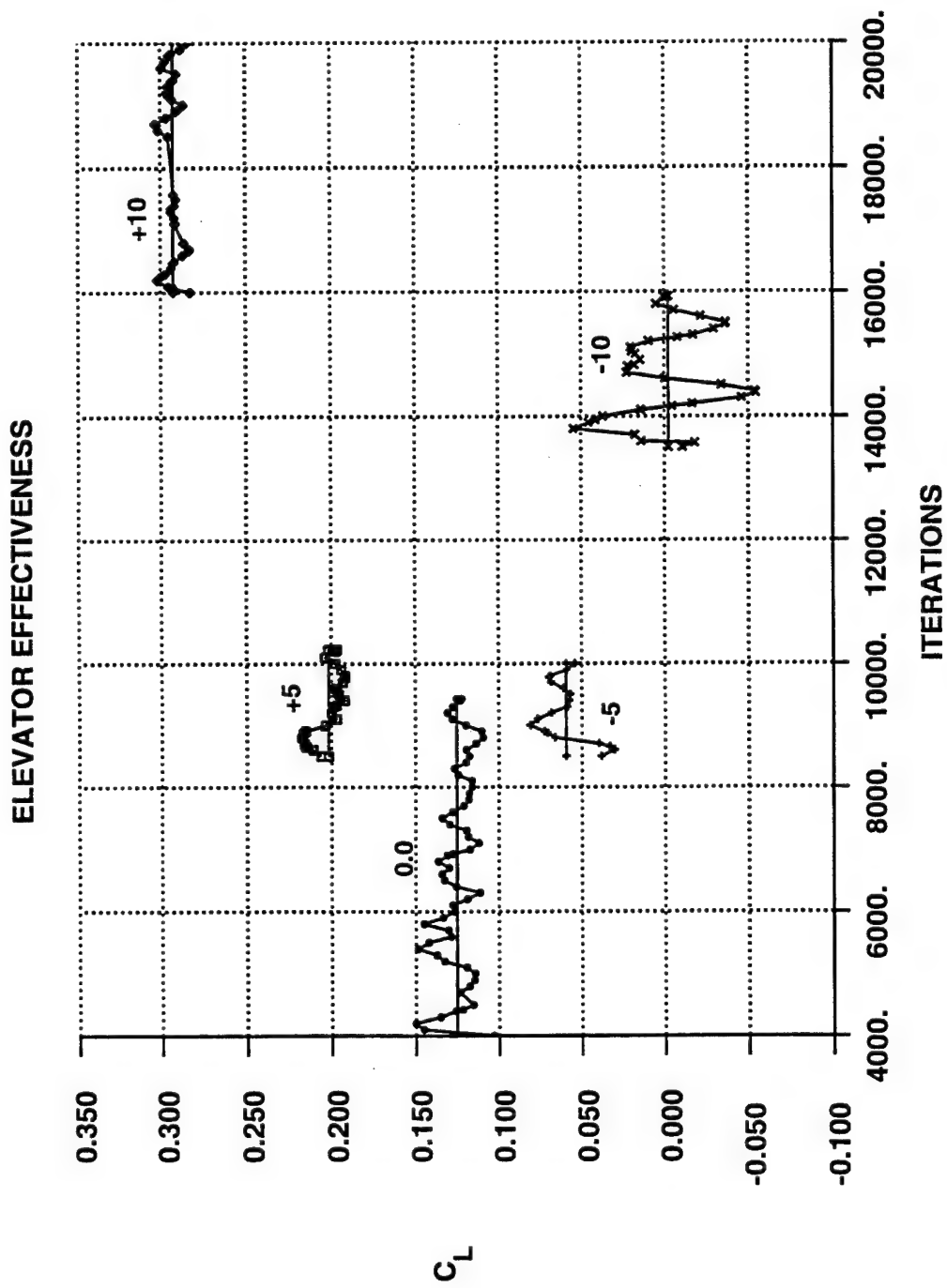


Figure 87 Variation of Lift Coefficient with Iterations

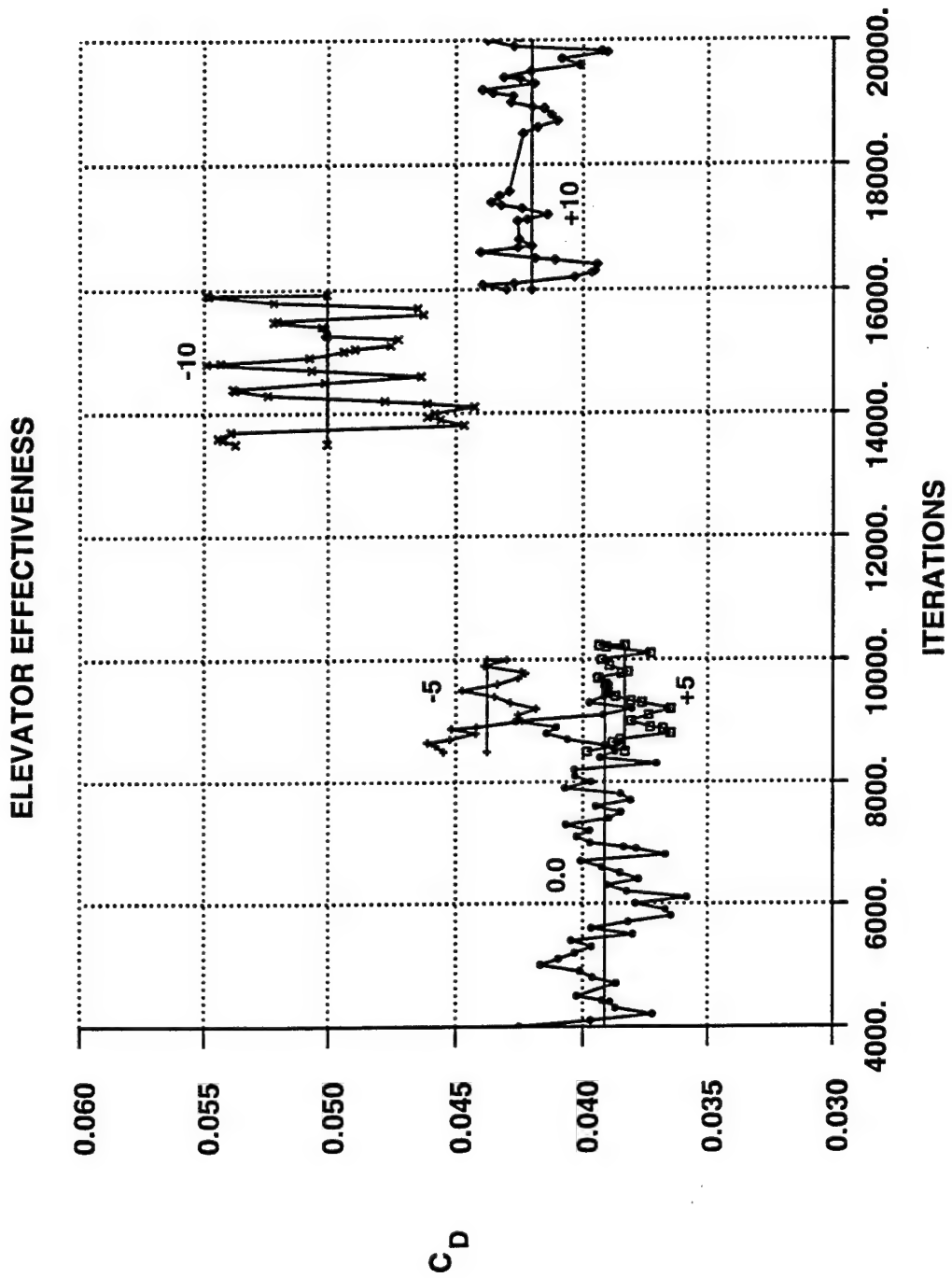


Figure 88 Variation of Drag Coefficient with Iterations

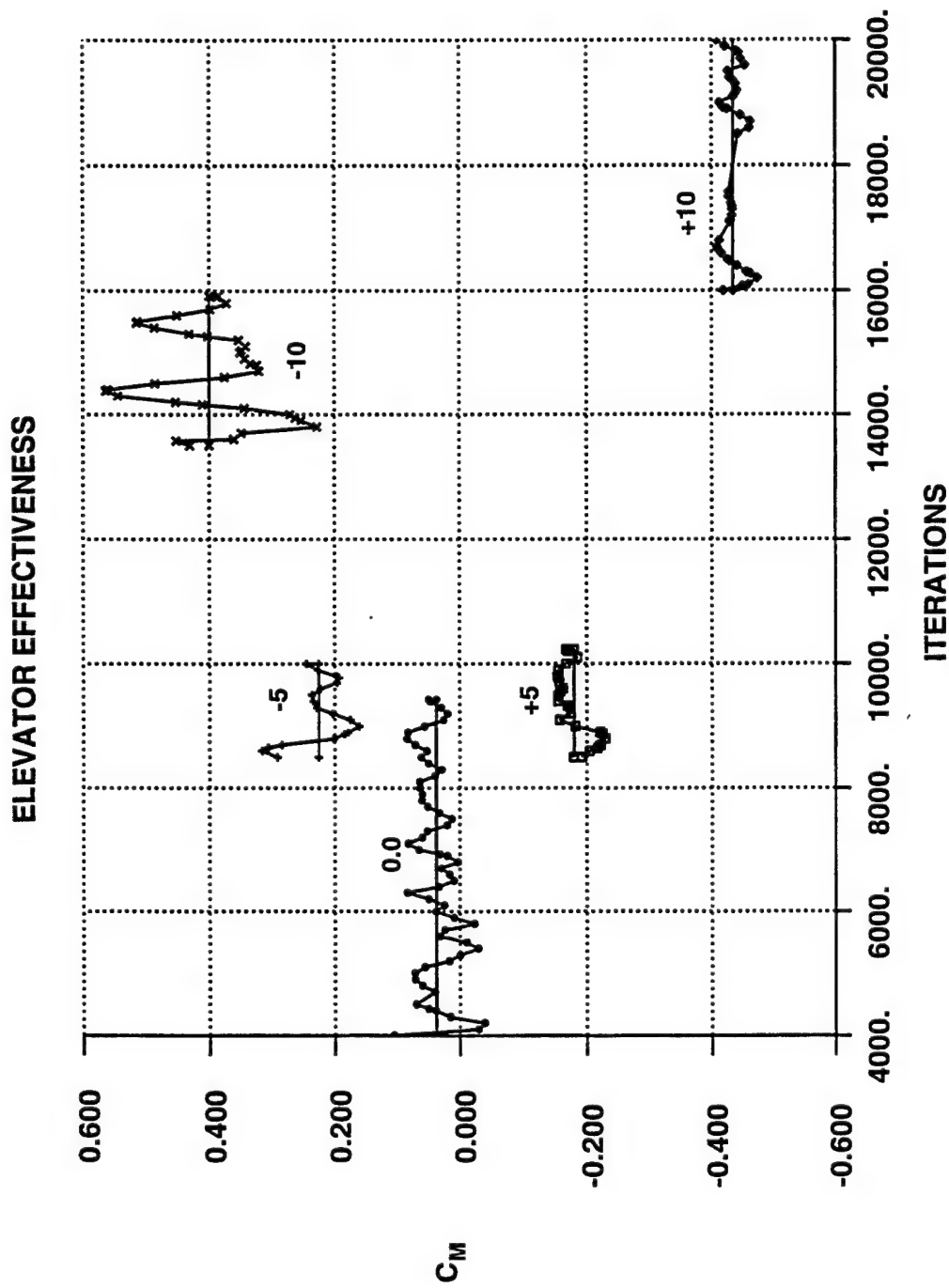


Figure 89 Variation of Pitching Moment Coefficient with Iterations

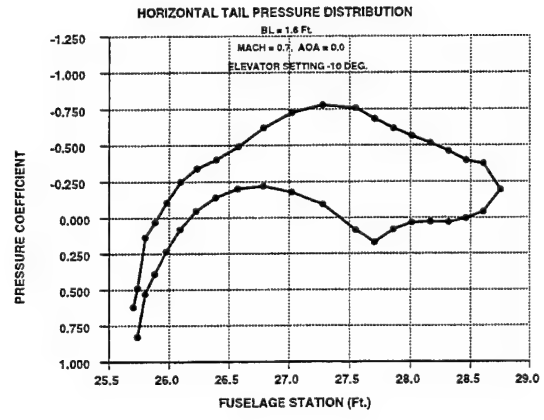
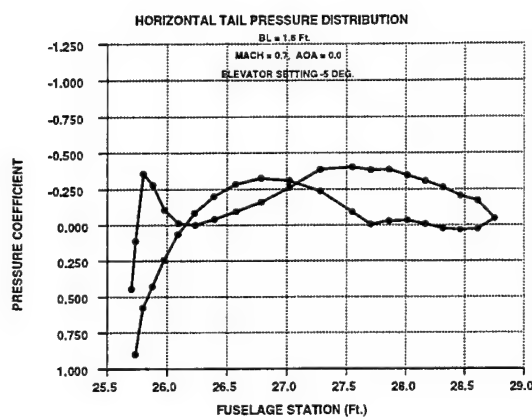
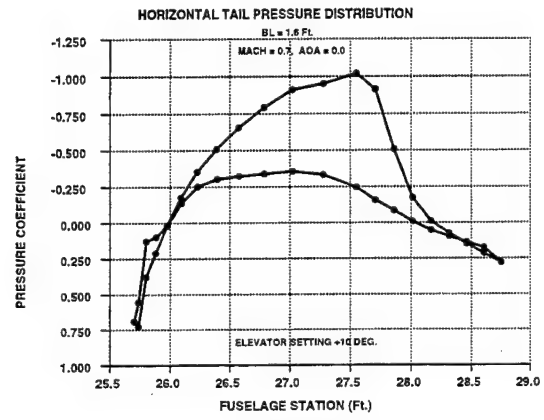
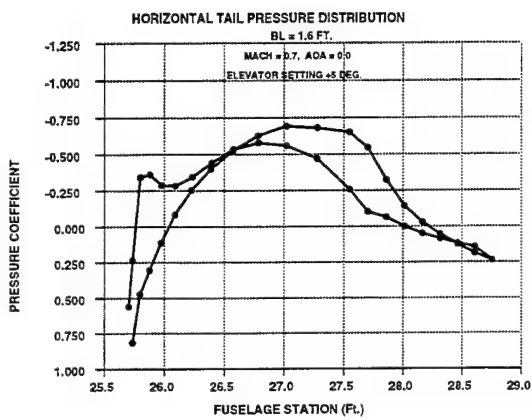
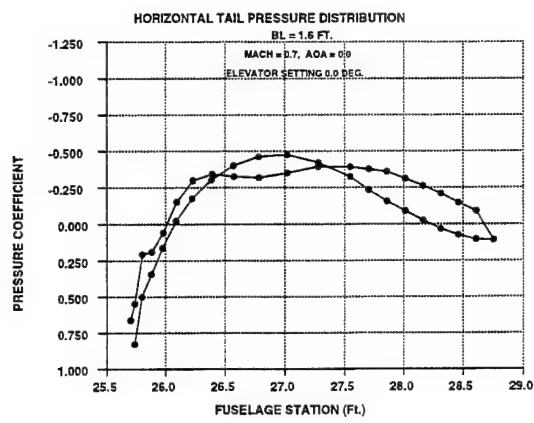


Figure 90 Tail Pressure Coefficients with Elevator Deflections - B.L. 1.6

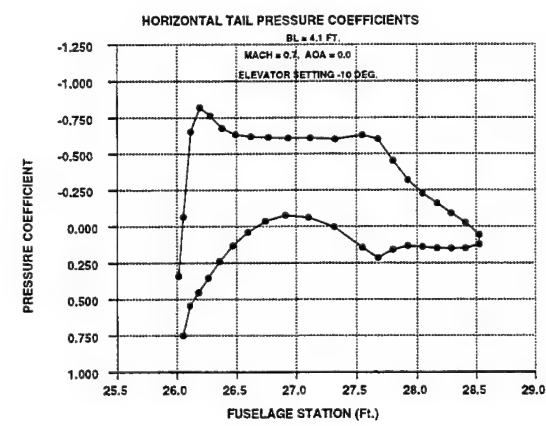
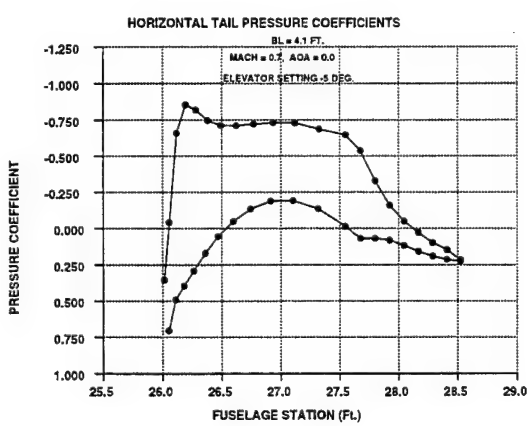
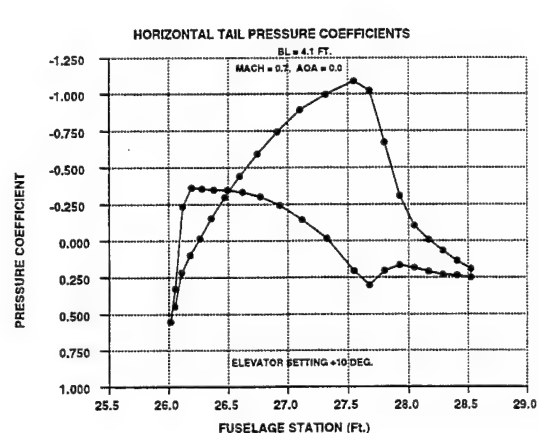
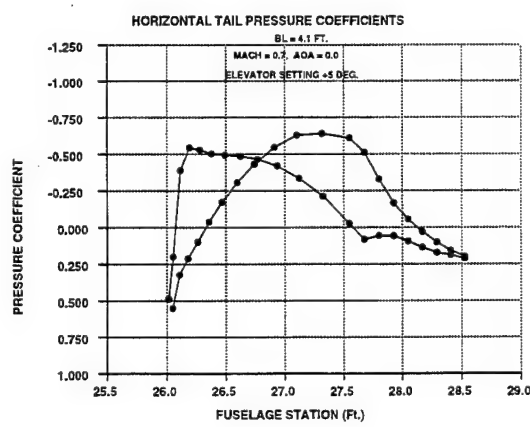
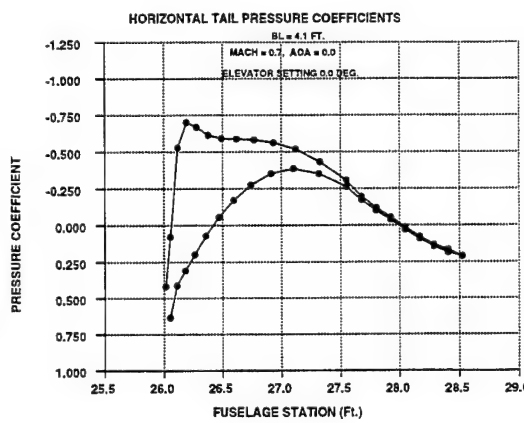


Figure 91 Tail Pressure Coefficients with Elevator Deflections - B.L. 4.1

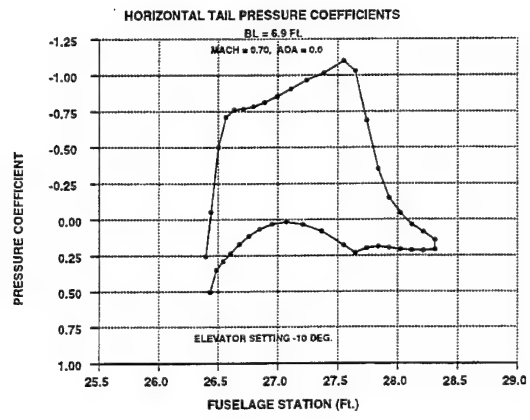
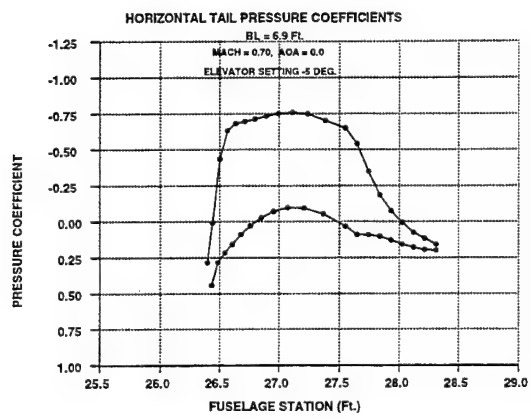
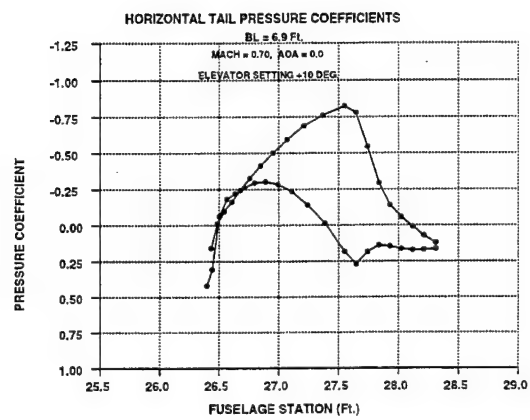
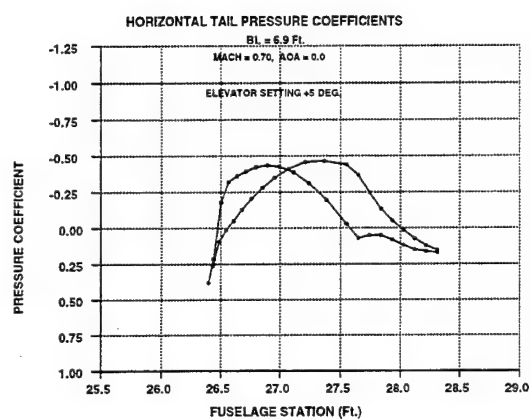
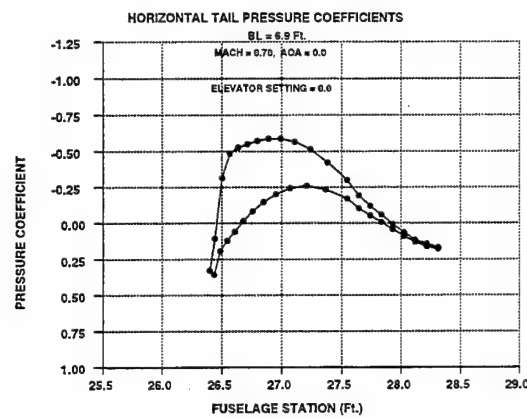


Figure 92 Tail Pressure Coefficients with Elevator Deflections - B.L. 6.9

6 Horizontal Tail Fairing

It was obvious during the early CFD solutions on the Century Jet aircraft that unsteady flow existed somewhere on the vehicle. The solutions were not converging as desired. Investigation of the flow solution revealed a relatively large region of separated flow on the inboard, lower surface of the horizontal tail. Engineers that ran the low speed test at OSU indicated that they had also detected evidence of separated flow in the tail-fuselage region.

Flow approaching the horizontal tail has a much more negative (downward) incidence along the fuselage than expected. It is not clear what causes the negative flow. Possible contributors include the engine inlet, the jet exhaust, and the fuselage, vertical and horizontal tail geometry/placement combination. Whatever the cause, the separation appears to exist at all speeds and angles of attack tested. Such separation is undesirable for a variety of reasons, such as noise, ride quality, aerodynamic drag, and structural fatigue.

The idea for the proposed tail fairing, which is referred to as the KEW fairing, came from a compromise of several requirements. Aerodynamically, the need was to provide a smooth transition of the negative incidence flow (near the fuselage) around the horizontal tail. For structural and ease-of-manufacturing considerations there was reluctance to change the current tail design. Therefore, the KEW fairing was intended to be an add-on, non-structural fairing that would fit over the existing tail geometry.

The shape of the KEW fairing was derived from an inverted forward section of a highly cambered NACA 4410 airfoil. The leading edge of the fairing extends forward of the tail approximately 7% chord (2.7 inches) at the tail-fuselage junction (spanstation = 10.48 inches) to zero at about 20 inches (spanstation = 30.4 inches) from the fuselage. The upper and lower surfaces were smoothly blended into the original tail geometry using an Intergraph CAD system. Figure 93 shows the fairing geometry at spanstation = 10.48. Figure 94 shows what a re-design of the airfoil section for the inboard part of the tail might look like, should it be desirable to maintain the original tail planform. This plot was created by normalizing both the original and modified airfoils to a unit chord.

Subsequent CFD analysis indicates that the KEW fairing was successful. The separated flow region on the tail has been completely eliminated, at least for the $Mach = 0.70$, $AOA = 2.0$ condition examined. Additional test runs at other Mach numbers, and with elevator settings, should be conducted before a final design is chosen for fabrication. Figures 95-99 compare pressure coefficients on the tail with and without the KEW fairing. The flow accelerates to supersonic speeds around the fairing lower surface. However, it does not appear to accelerate fast enough (rule of thumb, $Mach > 1.3$) to create a shock. A negative elevator deflection might induce enough additional circulation to create a shock, but significant negative elevator deflections are unlikely at $Mach = 0.70$ speeds. Incremental effects of the KEW fairing on lift, drag and pitching moment are provided in the table below. As expected, elimination of the separated flow region increased the down lift of the tail, reduced drag, and increased the aircraft pitching moment. Whether the increased pitching moment is enough to require a

change in tail incidence should be investigated. Figures 100-105 are color coded comparisons of the flow around the tail with and without the KEW fairing.

Table 4

Tail Fairing Effects			
Total Aircraft Increments			
Mach = 0.70, Elevator Angle = 0.0			
AOA	ΔCL	ΔCD	ΔCM
0	-0.0563	-0.0022	0.0802
2	-0.0602	-0.0019	0.0836

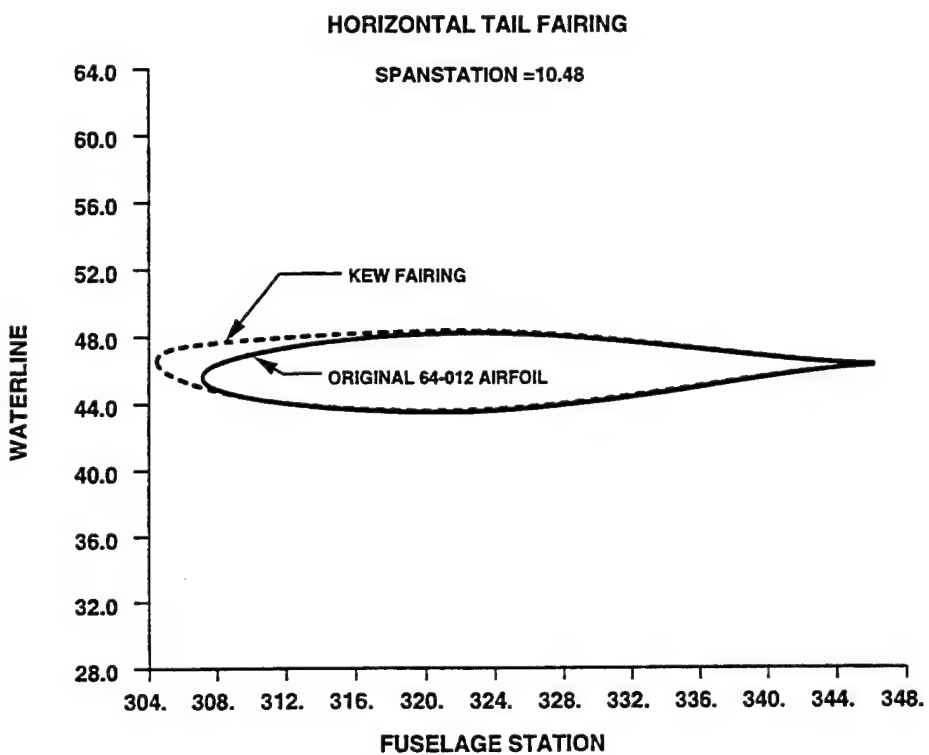


Figure 93 Horizontal Tail with KEW Fairing

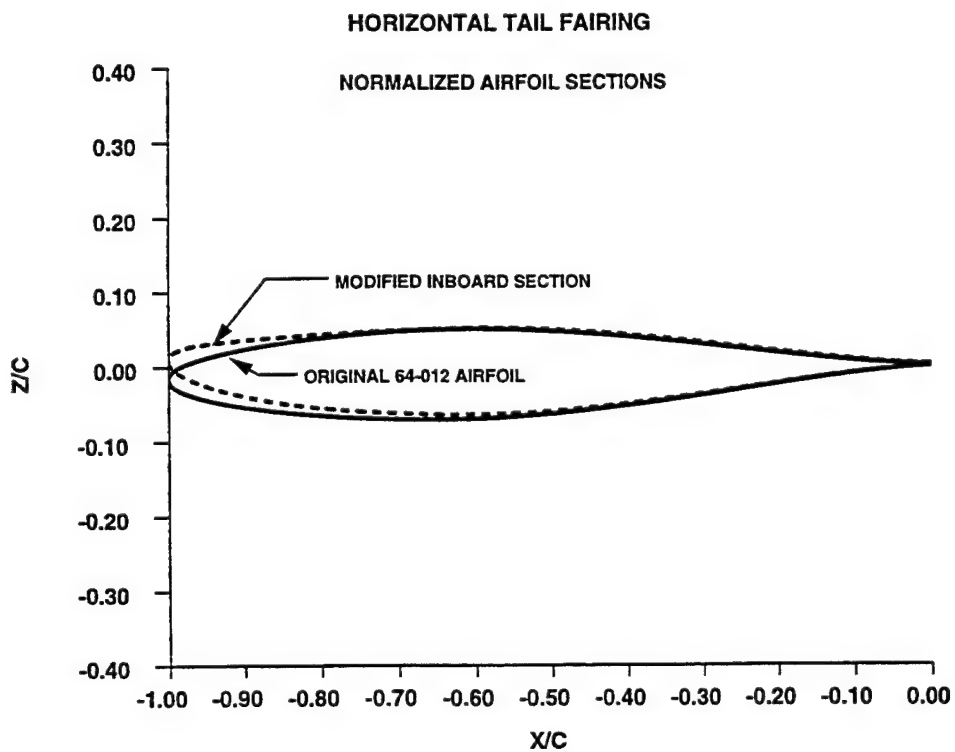


Figure 94 Horizontal Tail Geometry Normalized to Unit Length

Cp on Horizontal Tail

Mach = 0.7 Angle of Attack = 2

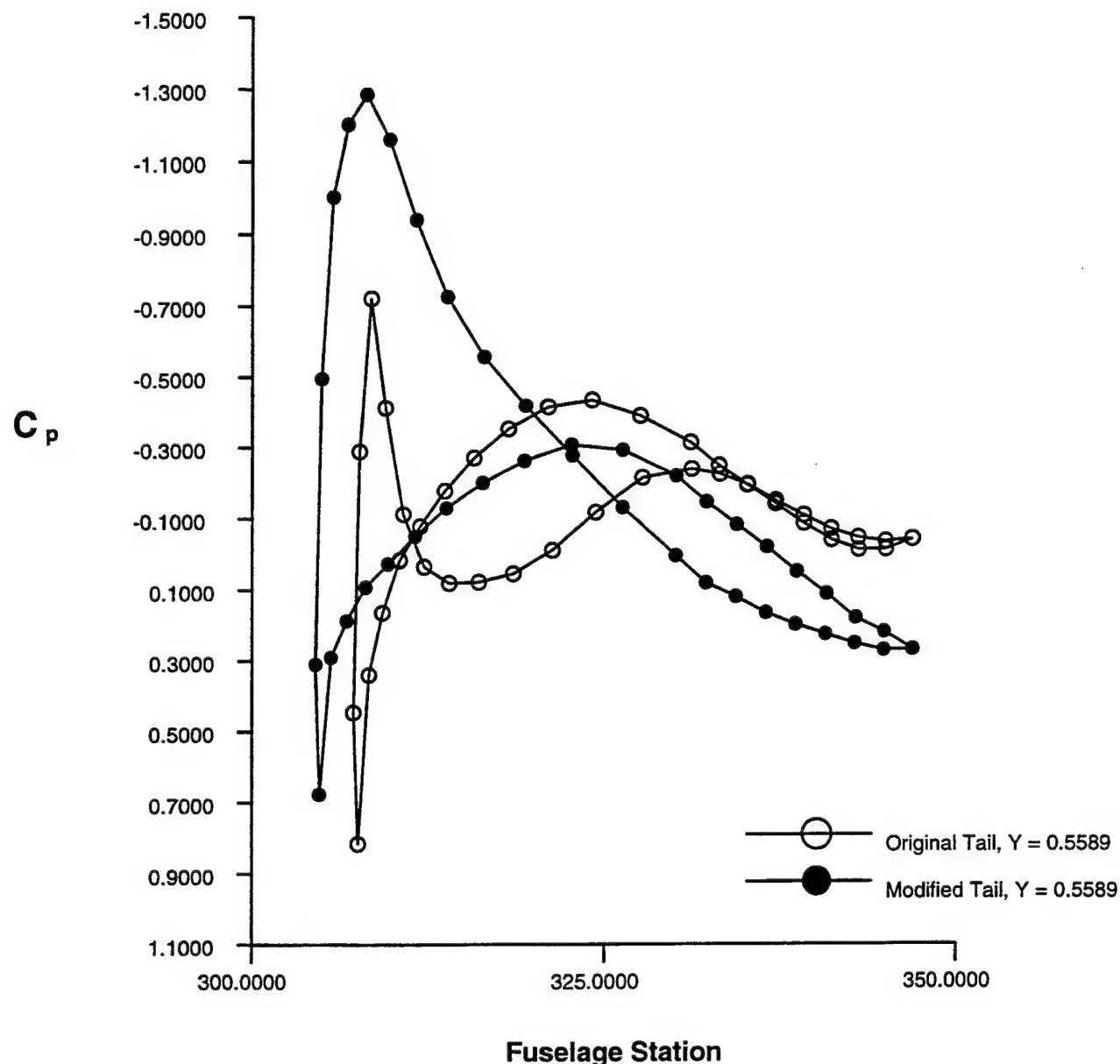


Figure 95 Pressure Coefficient on Tail with/without Tail Fairing - B.L. 0.56

Cp on Horizontal Tail

Mach = 0.7 Angle of Attack = 2

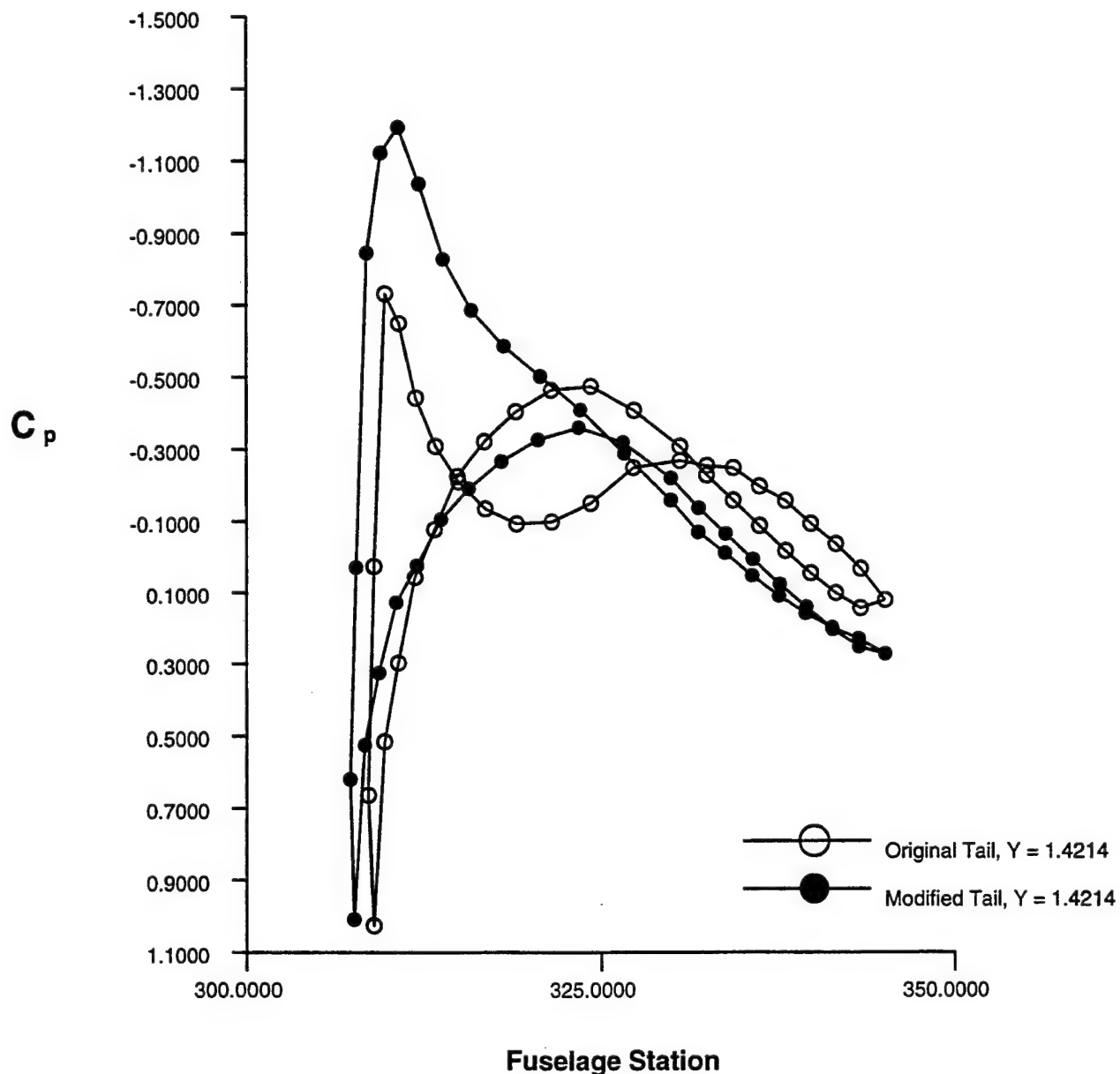


Figure 96 Pressure Coefficient on Tail with/without Tail Fairing - B.L. 1.42

C_p on Horizontal Tail

Mach = 0.7 Angle of Attack = 2

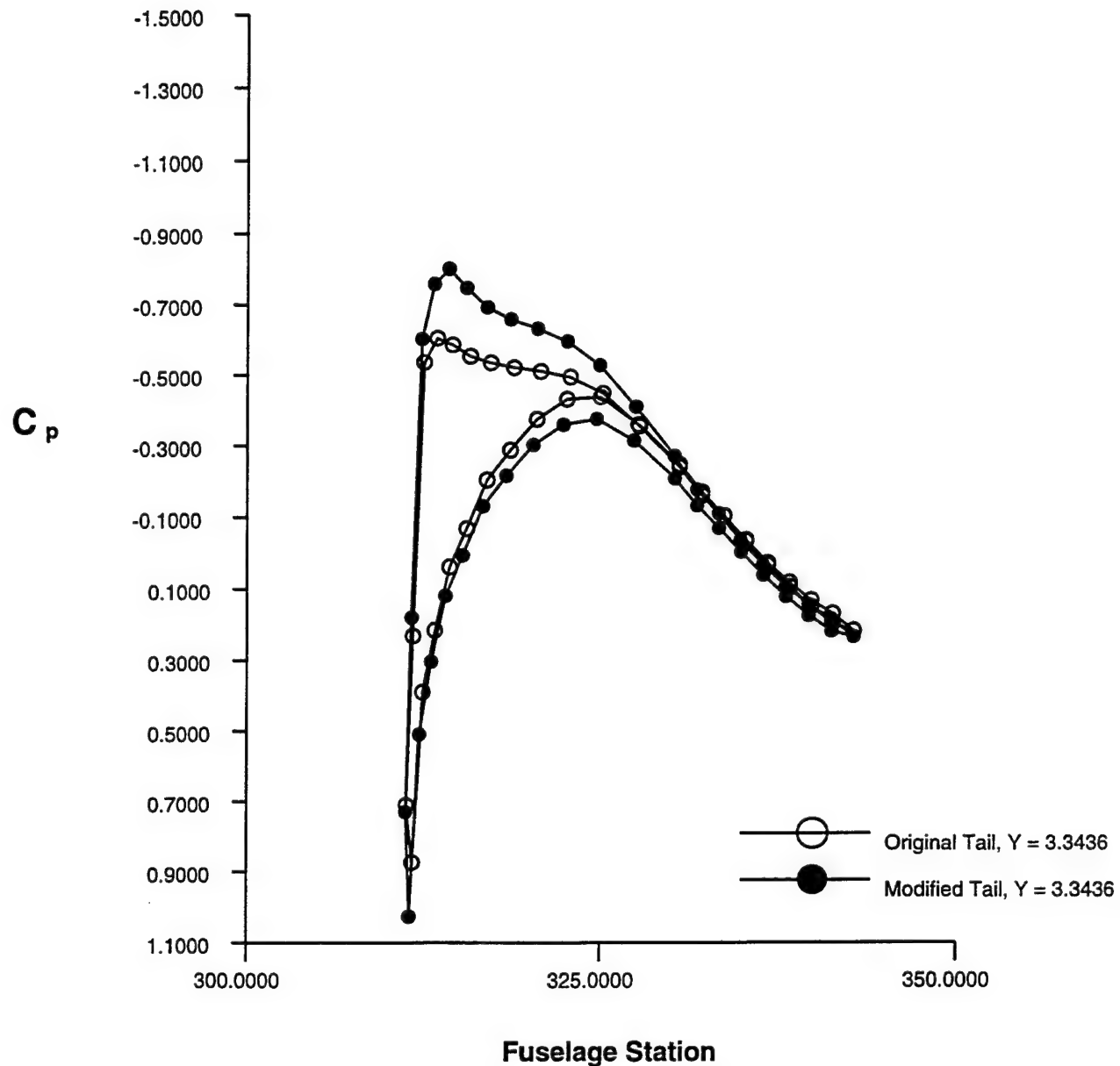


Figure 97 Pressure Coefficient on Tail with/without Tail Fairing - B.L. 3.34

C_p on Horizontal Tail

Mach = 0.7 Angle of Attack = 2

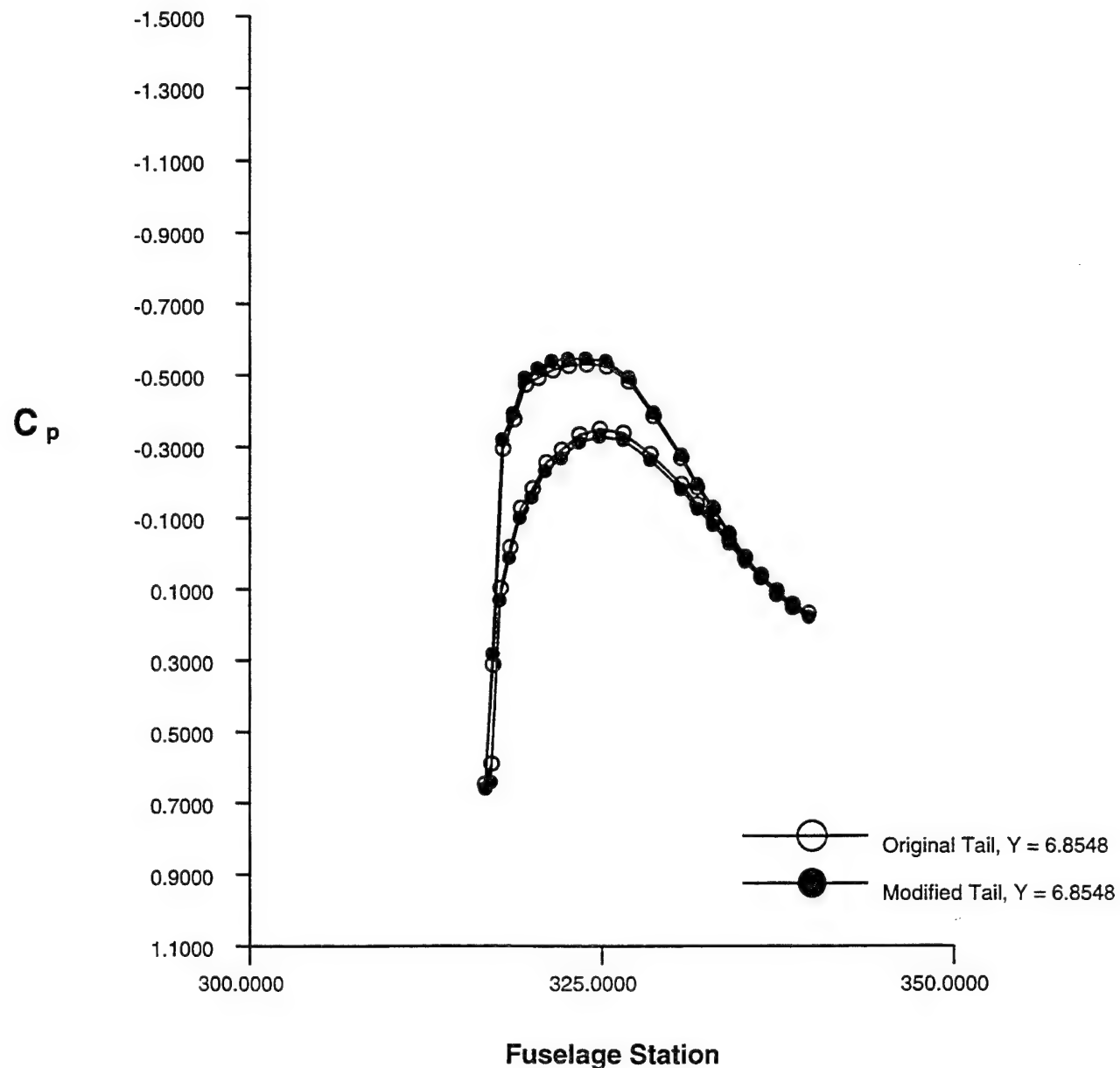


Figure 98 Pressure Coefficient on Tail with/without Tail Fairing - B.L. 6.85

C_p on Horizontal Tail

Mach = 0.7 Angle of Attack = 2

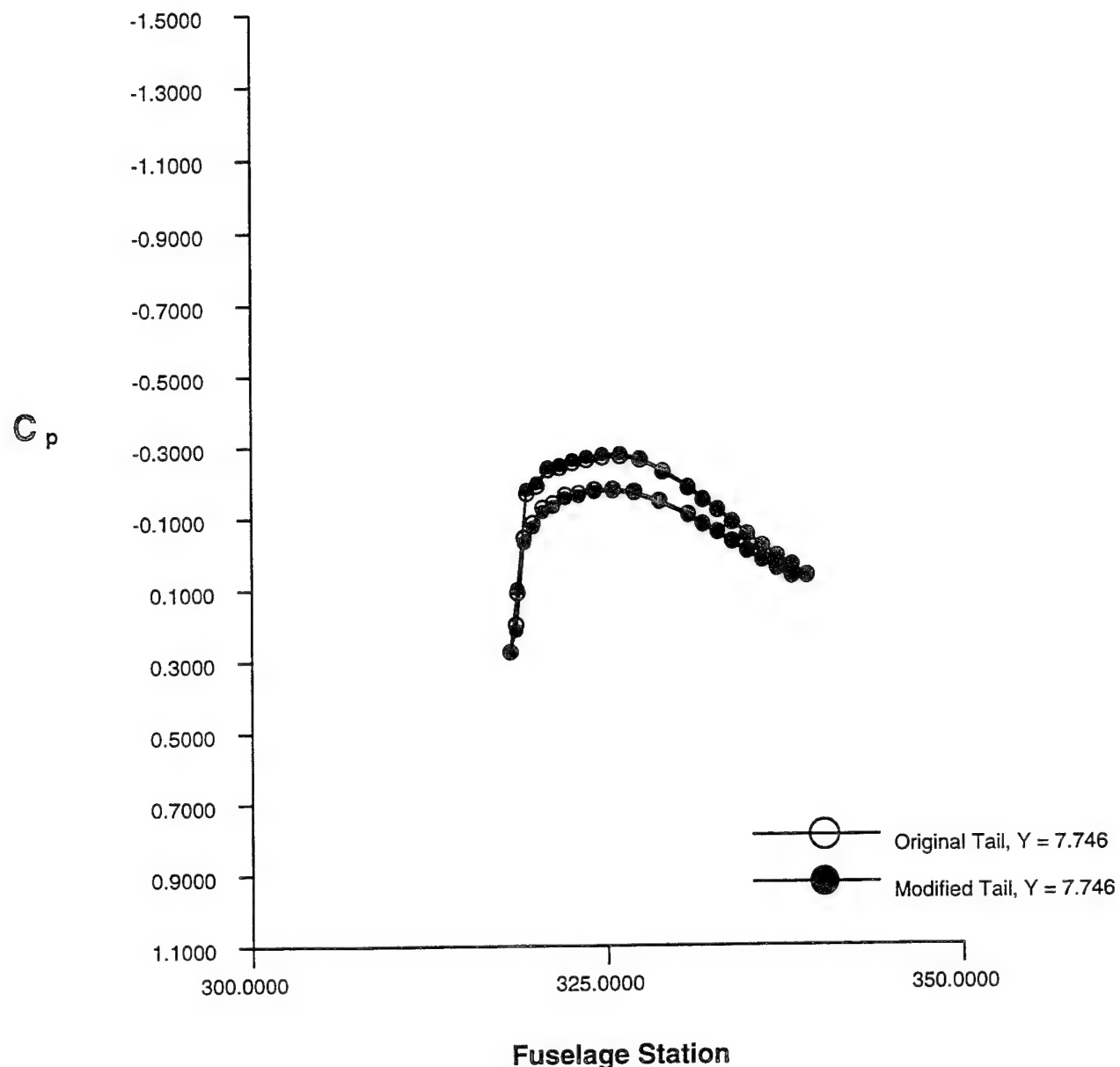


Figure 99 Pressure Coefficient on Tail with/without Tail Fairing - B.L. 7.75

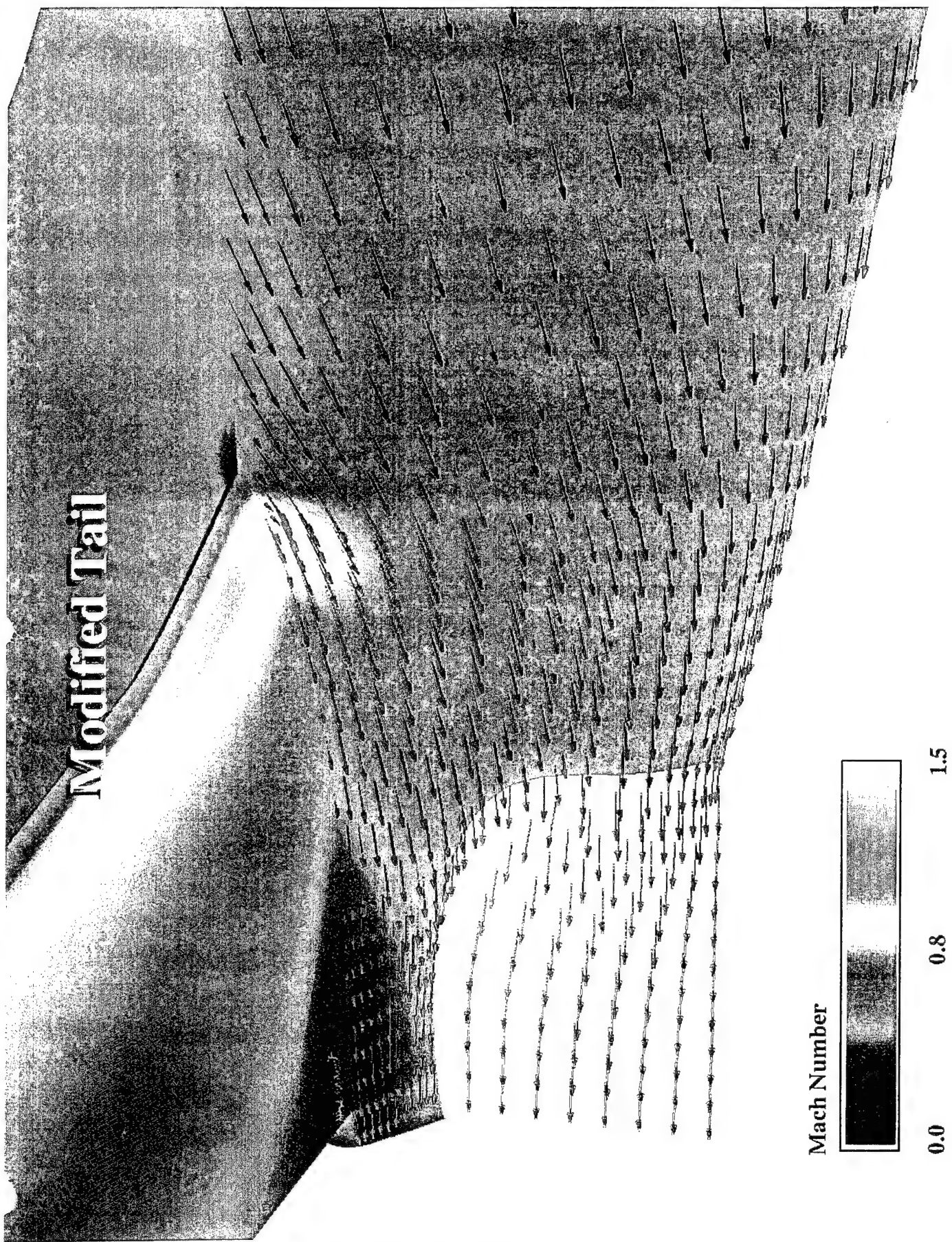


Figure 100 Velocity Vectors below Tail Fairing

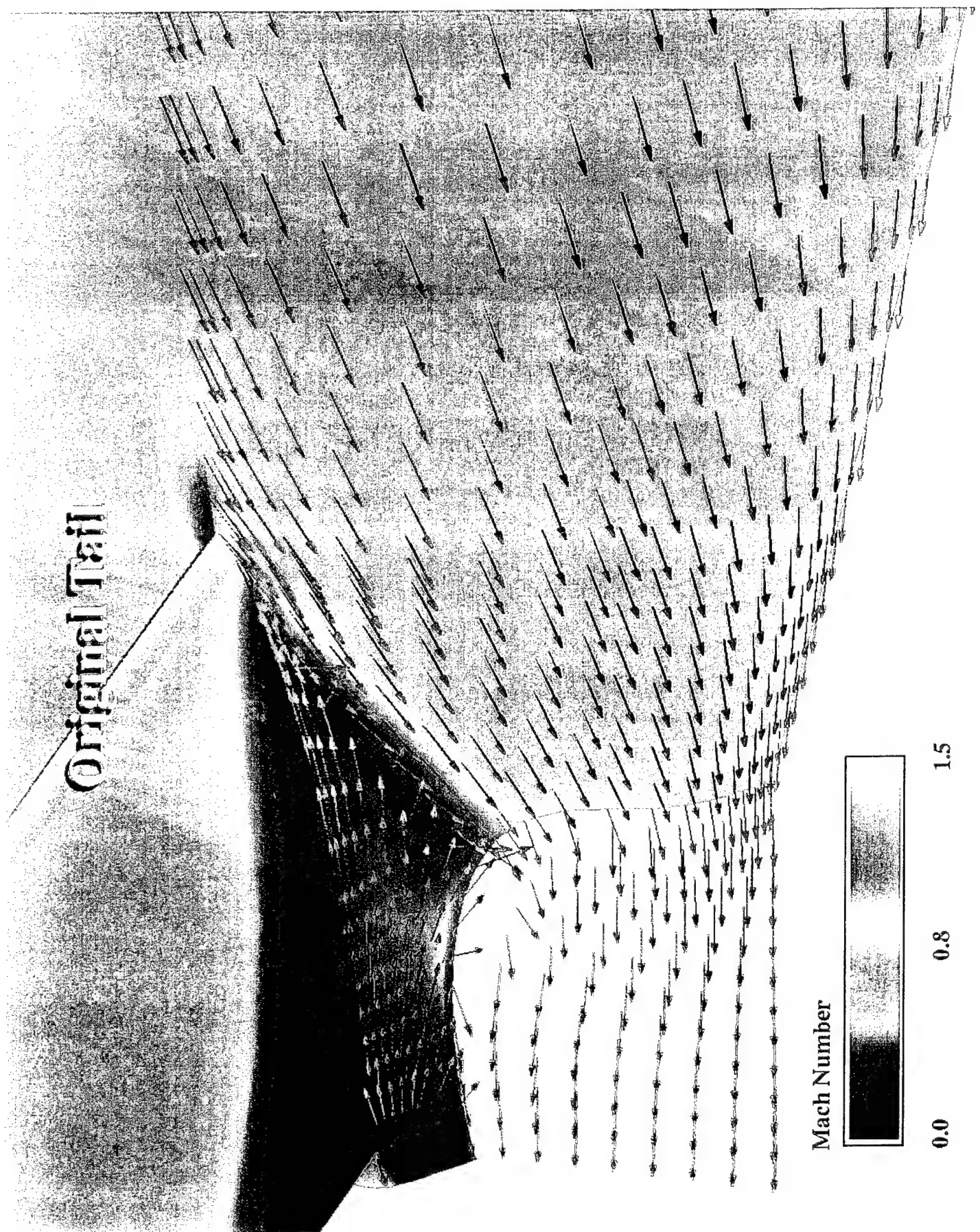


Figure 101 Velocity Vectors below Tail without Fairing

Modified Tail

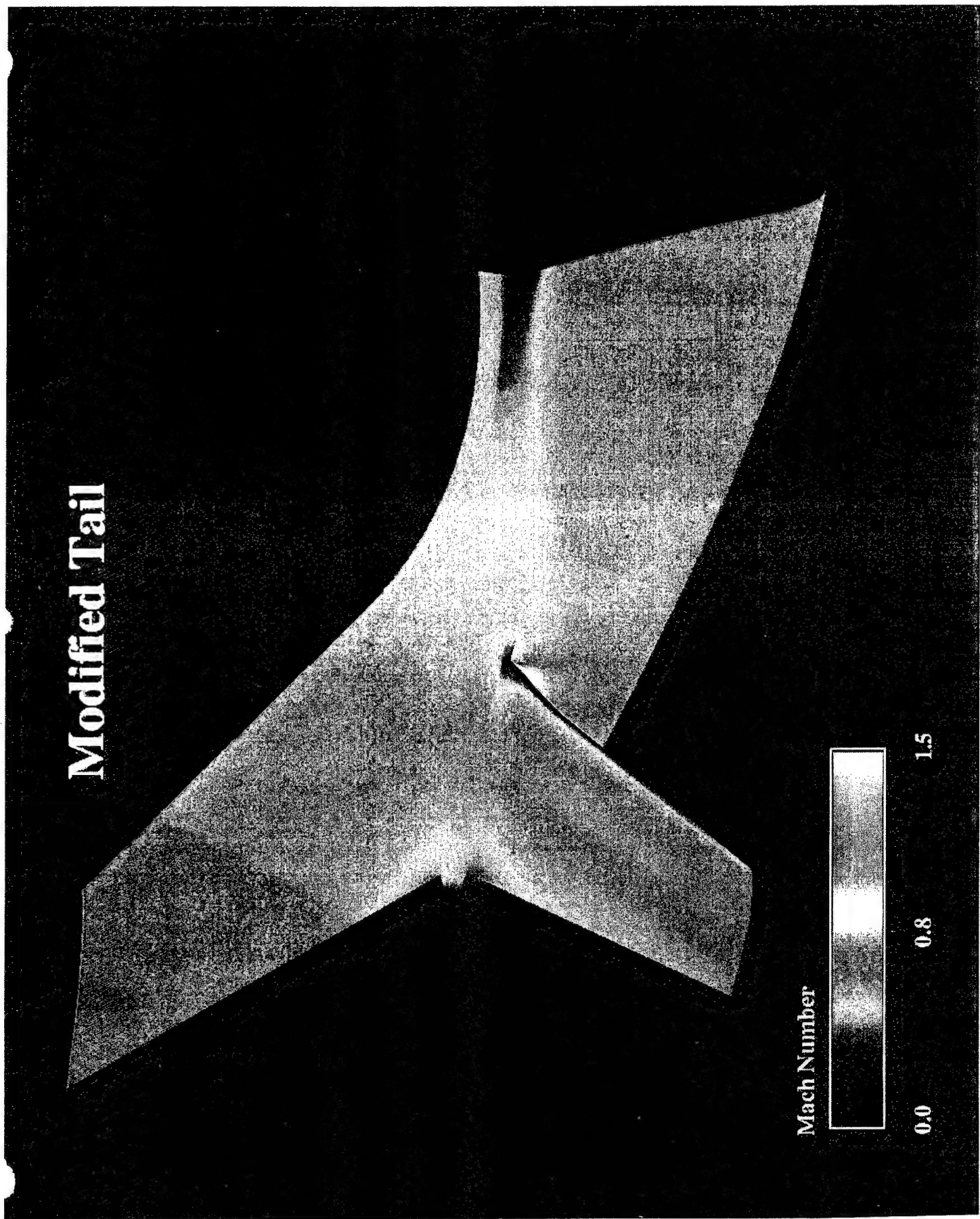


Figure 102 Mach Number Contours on Top of Tail with Fairing

Original Tail

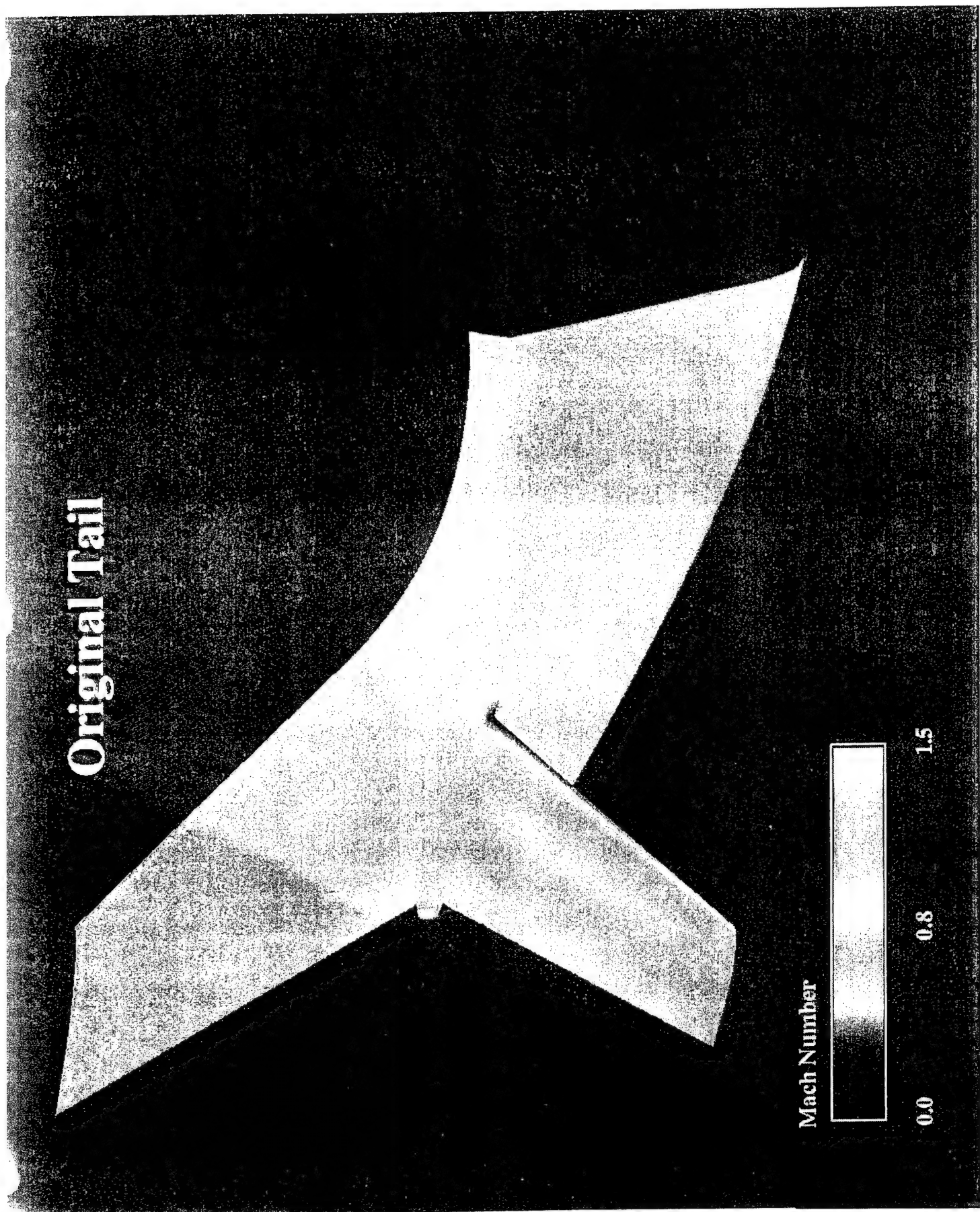


Figure 103 Mach Number Contours on Top of Tail without Fairing

Modified Tail

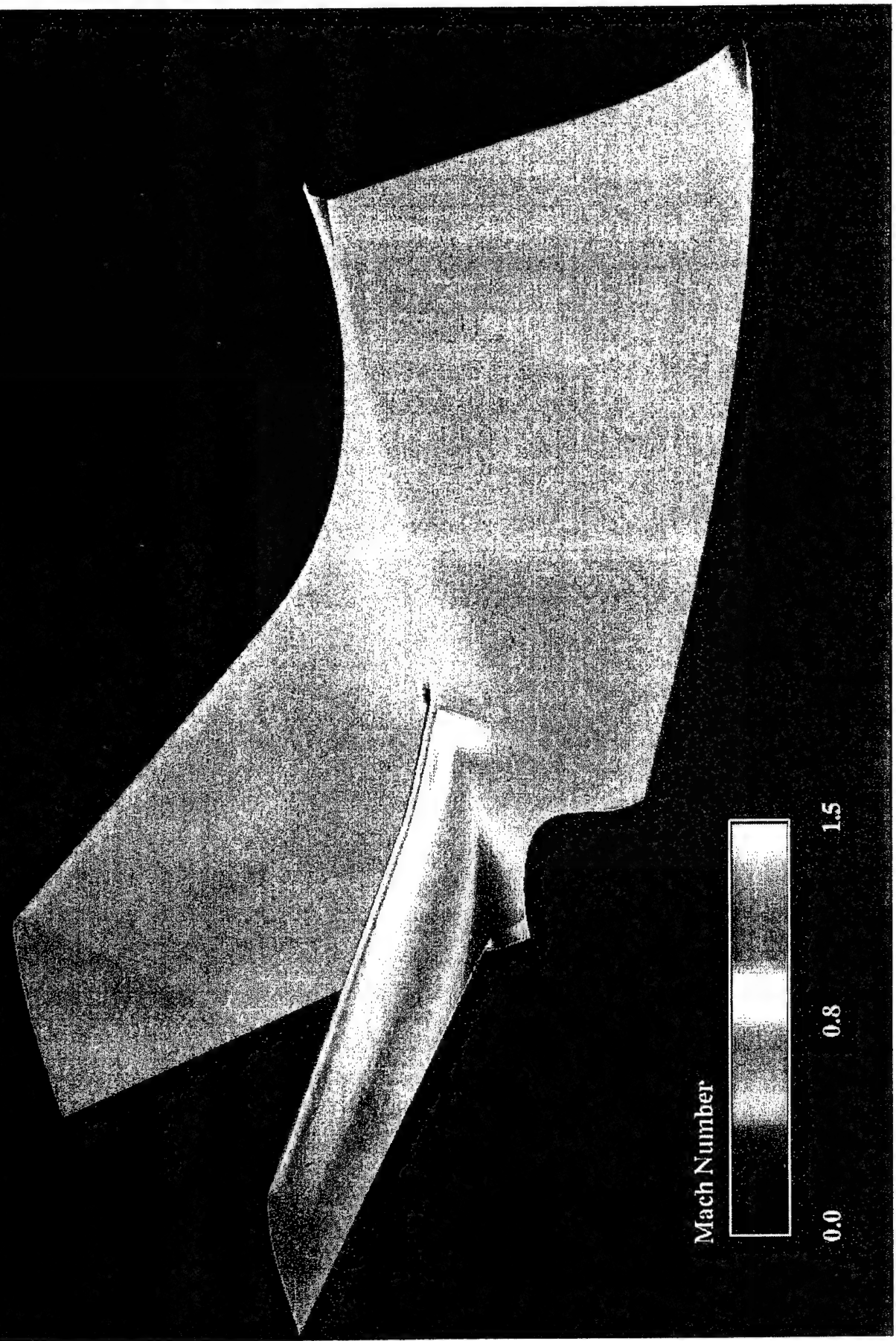


Figure 104 Mach Number Contours below Tail with Fairing

Original Tail

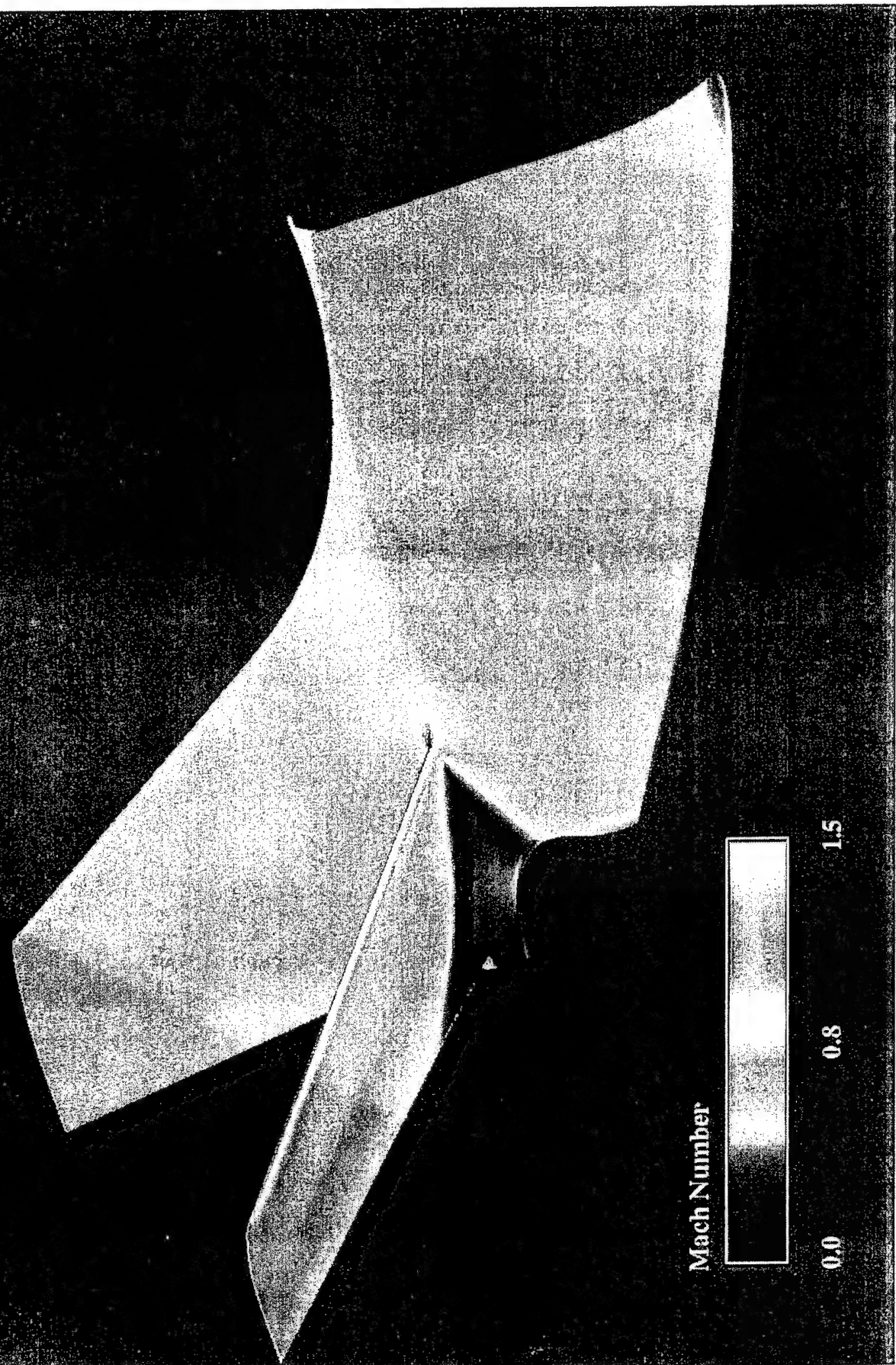
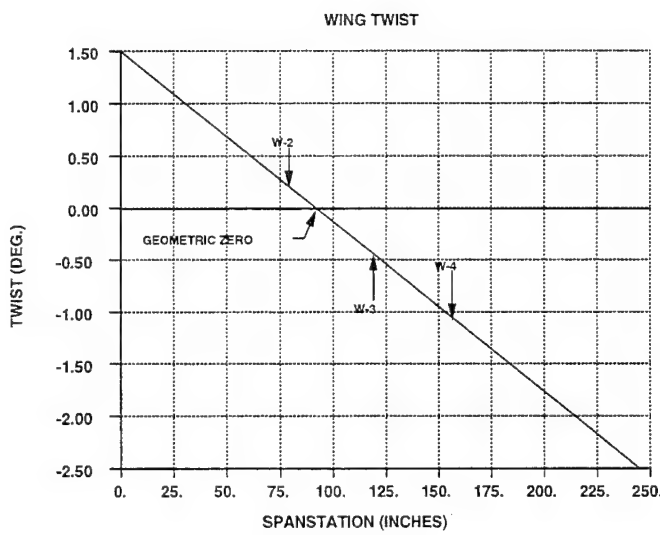


Figure 105 Mach Number Contours below Tail without Fairing

7 Comparison of CFD Data with 2-D Airfoil Data

Figure 106 compares the pressure coefficients for three span locations on the wing (Span Stations W-2 = 6.5, W-3 = 9.8, and W-4 = 13.2 ft.) with the 2-D data taken during an Ohio State University wind tunnel test⁶. The 2-D test conditions were Mach = 0.70, AOA = 0.0. As with the drag divergence comparison (Section IV), comparison of pressure coefficients between the 3-D Century aircraft and 2-D airfoil data is difficult. For example, what angle of attach does one use for the aircraft? The Century Jet wing is attached to the fuselage with 1.5 deg. incidence, however, there is significant twist built into the wing such that the tip is at -2.5 deg. incidence. Assuming linear twist, the geometric zero-angle-of-attack for the Century Jet wing would occur at about 38% semi-span (Span Station = 7.7 ft.), or at a point between W-2 and W-3. However, the CFD result on the Century Jet at the W-4 location appears to agree more closely with the 2-D test data. There are many other possible explanations for this result. Viscous effects, wind tunnel wall effects and differences in airfoil sections are a few possibilities. Indeed, the 2-D airfoil is a "SZ(1)-0215" section, whereas the Century Jet wing has a "MS(1)-0313" airfoil. Despite all these effects, the main difference between the 2-D and 3-D pressure data is near the leading edge, particularly on the lower surface. Considering the difference in airfoil sections, it is inappropriate to try to draw many conclusions from this comparison but it does increase the confidence in the value of the Euler results for design purposes.



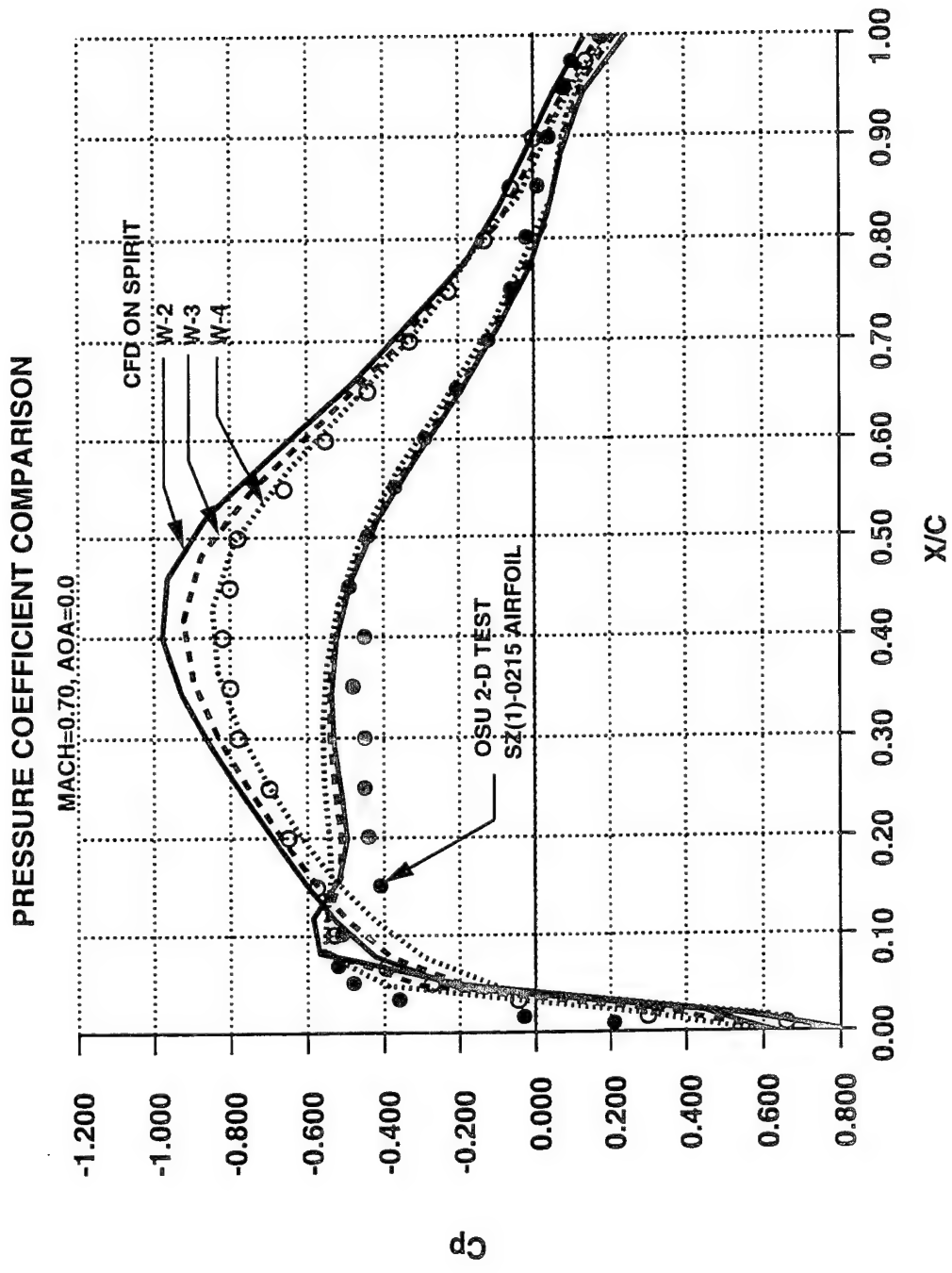


Figure 106 Pressure Coefficient Comparison of 2-D Airfoil with 3-D Wing

8 SUMMARY

This report documents the computational fluid dynamics (CFD) analysis of a small, single-engine business jet. The objective of the analysis is to predict the aerodynamic characteristics at transonic Mach numbers (up to the drag divergence Mach number) with various angles of attack and control surface deflections. A qualitative evaluation of the airflow conditions at the inlet face and the interaction of the inlet nacelle airflow on the vertical tail was performed. Wing chordwise pressures were compared to two-dimensional airfoil test data to provide a quantitative comparison.

The longitudinal aerodynamic characteristics, drag rise, and lateral directional stability analysis were accomplished using Mercury, an Euler code. The grid is a multi-block grid with point-to-point match-up at block interfaces with far-field boundaries 7 fuselage lengths away. A total of 1,348,777 points were used to build the computational domain around half of the aircraft. The main engine inlet had a specified mass flow rate and the auxiliary inlet was specified with a fixed pressure corresponding to the flight condition being modeled.

Longitudinal aerodynamic characteristics were determined by varying angle of attack at two Mach numbers, 0.2 and 0.7. The angles of attack investigated were 0, 2, 4 degrees for Mach = 0.2 and 0 and 4 degrees for Mach = 0.7. A Mach = 0.75 case with angles of attack of 1 and 2 is also included to determine drag rise. The resultant plots of lift coefficient versus angle of attack revealed positive, linear slopes which is expected since the wing on the aircraft is straight and no vortex lift is expected. The pitching moment is non-linear with angle of attack. The aircraft responds with less positive nose-up force in all of the cases and obtains a negative pitching moment for the Mach = 0.7 case at angle of attack equal to 4.0. The Mach = 0.75 curve almost lies directly on the Mach = 0.7 curve.

The lateral stability characteristics of the aircraft were obtained by running a high and low speed case at two beta angles, 5 and 10 degrees, angle of attack of 0.0. The complete aircraft configuration was run due to the asymmetry of the flow. At beta = 5.0, the lift coefficient decreases slightly but returns to the C_L $_{\beta=0}$ value at beta = 10.0 for both Mach cases. The pitch coefficient behaves in a reverse manner. It increases at beta = 5.0 and then decreases at beta = 10.0. The high speed case exhibits a very small negative rolling moment (right wing down). The low speed case responds linearly with a much greater negative rolling moment (right wing down). Finally, the yawing coefficient in both cases responds linearly with a negative yawing moment (nose right).

The TEAM code, a Euler code with transpiration boundary condition options, was used to simulate the effect of the aileron deflection on the lift, drag, and moment coefficients. Aileron deflections of ± 5 deg, and ± 10 deg for flight Mach number of 0.7 were computed. The effect of these deflections is determined by comparing the aerodynamic loads of the simulated deflected ailerons against baseline (no aileron deflection) values. The lift, drag, and pitching moment coefficients show that the effects of aileron deflection at Mach 0.7 are more pronounced than the low speed (Mach 0.2) experimental data. The chordwise variation

of the pressure coefficient (C_p) for five sections on the wing and three sections on the horizontal tail are provided. Very little effect is observed at the root of the wing, with increasing influence of the deployed aileron noted for the sections closer to the 60% span location of the inboard start of the aileron.

Elevator effectiveness was simulated using the transpiration boundary condition to model elevator deflections. Calculations for the $Mach = 0.7$, $AOA = 0.0$ flight condition with ± 5 and ± 10 degrees elevator deflection were completed. Increments in total aircraft lift, drag and pitching moment coefficient due to elevator deflections were tabulated and compared with increments from a low speed wind tunnel test. Wave drag increments were determined by subtracting the drag value at $Mach = 0.70$ from the drag values at the other Mach numbers. The CFD analysis of the aircraft indicated only about 20 counts (0.0020) of drag difference between $Mach = 0.20$ and $Mach = 0.70$, but 105 counts difference between $Mach = 0.70$ and $Mach = 0.75$. Thus drag divergence appears abruptly, with a relatively large increase in drag, at speeds above $Mach = 0.70$.

It was obvious during the CFD solutions on the aircraft that unsteady flow existed in the vicinity of the vehicle. Engineers that ran the low speed test indicated that they had also detected evidence of separated flow in the tail-fuselage region. Flow approaching the horizontal tail has a very negative (downward) incidence along the fuselage and the result is a separated flow region on the inboard lower surface of the tail. The separation appears to exist at all speeds and angles of attack tested. A tail fairing was proposed to provide a smooth transition of the negative incidence flow (near the fuselage) around the horizontal tail. Subsequent CFD analysis indicates that the fairing was successful in completely eliminating the separation. As expected, elimination of the separated flow region increased the down lift of the tail, reduced drag, and increased the aircraft pitching moment.

Finally, a comparison of pressure coefficients at three span locations on the aircraft wing with the 2-D data taken during a wind tunnel test is provided. Although comparison of pressure coefficients between the 3-D aircraft and 2-D airfoil data is difficult, the W-4 location agrees closely with the 2-D test data, the main difference being near the leading edge on the lower surface.

This CFD (Euler) analysis of the single engine business jet configuration provides critical transonic aerodynamic information for the designers. This information, combined with lower-order numerical results and low speed 3-D and transonic 2-D wind tunnel test, provides a clear picture of the aircraft's aerodynamic performance.

IX References

1. Avery, M., Hoffmann, M.J., "Scale Model Test Final Report for the Paragon Spirit Aircraft in the OSU/AARL 7"x10' Low Speed Wind Tunnel," OSURF Project No. 73073, April 1996.
2. Raj, P., et al., "Three-dimensional Euler/Navier-Stokes Aerodynamic Method (TEAM), Volume 1: Computational Method and Verification," *AFWAL-TR-87-3074 (Revised)*, June 1989.
3. Goble, B. D., Raj, P., and Kinard, T. A., "Three-dimensional Euler/Navier-Stokes Aerodynamic Method (TEAM) upgrade," *WL-TR-93-3115*, February 1994.
4. Weed, R. A., and Sankar, L. N., "Computational Strategies for three-dimensional flow simulations on distributed computer systems," *25th AIAA Fluid Dynamics Conference*, Paper 94-2261, 1994.
5. Raj, P., and Harris, B., "Using Surface Transpiration with an Euler Method for Cost-Effective Aerodynamic Analysis," *AIAA Applied Aerodynamics Conference*, Paper 93-3506, 1993.
6. Gregorek, G.M., Hoffmann, M.J., and Berchak, M.J., "Aerodynamic Characteristics of the OSU SZ(1)-0215 Airfoil as Determined by Tests in the OSU/AARL 6"x22" Transonic Blowdown Wind Tunnel," OSURF Project No. 73073, March 1996.

List of Symbols

AOA	angle of attack (°)
M	Mach number
T	temperature (°R)
P	pressure (psia)
x-dir	axis along fuselage length (inches)
y-dir	axis along wing span (inches)
z-dir	axis normal to fuselage and wing (inches)
C_L	lift coefficient
C_D	drag coefficient
C_m	pitch coefficient
C_n	yaw coefficient
C_l	roll coefficient
C_p	pressure coefficient
Butt Line (B.L. or BL)	wing or tail span location (y-dir)